Theoretical modeling of the dynamics of photo-excited states in light-driven molecular rotary motors

Kazaryan, Andranik Koryunovich

Theoretical modeling of the dynamics of photo-excited states in light-driven molecular rotary motors

Andranik Kazaryan

University of Groningen
Zernike Institute
for Advanced Materials

Zernike Institue PhD thesis series 2011-02
ISSN 1570-1530
ISBN: 978-90-367-4722-6

The research presented in this thesis was performed in the Theoretical Chemistry Group (part of the Zernike Institute for Advanced Materials) of the University of Groningen, The Netherlands.

Andranik Kazaryan,

Theoretical modeling of dynamics of photo-excited states in light-driven molecular rotary motors,

Proefschrift Rijksuniversiteit Groningen.

RIJKSUNIVERSITEIT GRONINGEN

Theoretical modeling of the dynamics of photo-excited states in light-driven molecular rotary motors

Proefschrift

ter verkrijging van het doctoraat in de
Wiskunde en Natuurwetenschappen
aan de Rijksuniversiteit Groningen
op gezag van de
Rector Magnificus, dr. F. Zwarts,
in het openbaar te verdedigen op
maandag 10 januari 2011
om 16.15 uur

door

Andranik Koryunovich Kazaryan
geboren op 15 december 1979
te Erevan, Armenië

Promotor:	Prof. dr. M. Filatov
Beoordelingscommissie:	Prof. dr. M. Olivucci
	Prof. dr. W. Thiel
	Prof. dr. E. J. Baerends

ISBN: 978-90-367-4722-6

маме, папе, брату

и жене

Contents

Chapter 1

General Introduction

1.1 Preface

The immense progress in science and technology nowadays calls for new doorways to developing memory storage devices, [1] processing units and, importantly, entirely new means of turning light energy into useful work. The heritage of nature offers us an abundance of smart solutions realized at molecular level: biologically active molecules are driven by heat, electron and proton transfer, cis-trans isomerizations. The reactions involved are generally very fast and efficient, proceeding often on picosecond and subpicosecond timescales. It becomes clear that a further advance in technology should inevitably adopt the mechanisms involved in the molecules and macromolecules in living bodies and plants.

The development of the existing and invent of new experimental techniques renders it possible to literally inspect the molecular compounds and even atoms at the scale of a fraction of Angstroms. With the advent of electron microscopes researchers have discovered the elementary machines that are responsible for transformation of chemical energy into mechanical motion, [2] such as intra- and inter- cellular transport and even exerting body locomotion via muscle contraction.

Presently the mechanisms behind the chemically powered macromolecules are well understood. There exist different types of the so-called molecular motors that bring about and steer mechanical motion in biological systems. Two main subgroups are distinguished by type of motion: linear motors, such as kinesin, myosin or RNA, and rotary motors such as bacterial flagella or F_1-ATPase motor. [2, 3] In plants the biological energy for motors is supplied from the sun. Photons are harvested by photosynthesis in chloroplasts and transformed into chemical energy that is subsequently passed to the molecular motor. [4]

Another type of bioactive molecules are photoreceptors, [4] that respond to light with a conformational change, such as cis-trans and trans-cis isomerization about a carbon-carbon double bond. Since the invention of ultrafast spectroscopy extensive theoretical study has been carried out in the area of photobiology. One of the earliest investigation was focused on the study of photoisomerization of the retinal

chromophore in the primary vision process, [5] revealing that the first photoproduct is formed within 6 ps after light absorption.

The design of molecular machines, such as rotary molecular motors and photoswitches, represent a real challenge in the context of future technology. Early ideas of the molecular design were given by Richard Feynman in his classic talk. [6] Presently there have been created numerous devices that convert light into mechanical motion. [7] The systems range from single-molecule switches/motors such as the synthetic light-driven molecular motors, [8, 9] which will be discussed in more details in further sections, to state-of-the-art devices such as, e.g. the photomobile by Yamada and coworkers [10] that is based on disarmingly simple idea of utilizing the push-pull properties of azobenzene chromophore to stir a plastic belt that is wrapped around two pulleys. The azobenzene molecules that are embedded into a liquid-crystalline elastomer (LCE) matrix are aligned along the belt due to the anisotropic order of mesogens of LCE that also leads to anisotropic contraction of the chromophores. When incorporated into liquid crystals, azobenzene molecules can isomerize in both directions depending on the wavelength of radiation, so UV light causes trans-cis isomerization, whereas exposed to a visible light the phase transition in the liquid crystals will lead to a reversed cis-trans isomerization of azobenzene. Upon continuous irradiation of the laminated plastic belt by two light sources at two positions it was shown that a contraction of the belt on one side and stretching on the other side leads to a rotation of pulleys. In this stunning example the light-initiated molecular deformations are directly coupled to the macroscopic motion which is a clear demonstration of future prospects in techniques for efficient conversion of light into motion.

One of the first endeavors to create a single molecule motor was made by Kelly and coauthors [11–13] who synthesized a version of Feynman's ratchet and pawl (Fig. 1.1).

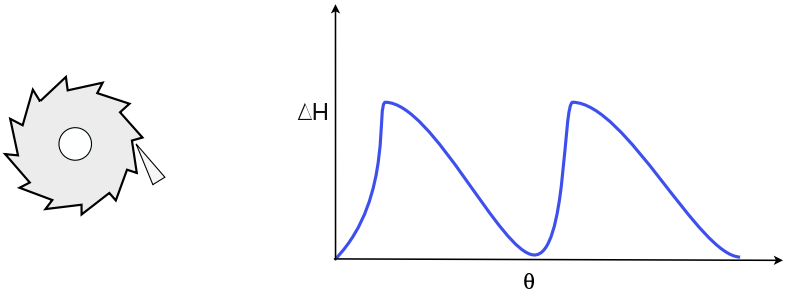

Figure 1.1: *Ratchet and pawl and the corresponding schematic potential energy curves.*

The main goal in designing the molecule was to achieve an asymmetric torsional potential and the molecule was expected to perform a directional motion due to the different speed with which the resistance builds up in clockwise and counterclockwise directions. However, it was shown that when the molecule is immersed in a solution it performs rather a Brownian motion as can be expected from the Second Law of Thermodynamics. [14] To satisfy the second law of thermodynamics, an energy supply is needed. After c-storeoupling the ratchet to energy coming from a chemical reaction Kelly achieved rotation through 120° in one direction. [8, 11–13]

In 1997, the Feringa group synthesized a chiral helical alkene that later in 1999 was shown to be capable of performing a 360° continuous rotation around the central double bond [15, 16] as depicted in Fig. 1.2 The rotation was initiated by consecutive irradiation and heating of the molecule in four strokes. The main distinction from the Kelly's ratchet is the type of energy supply that triggers the motion.

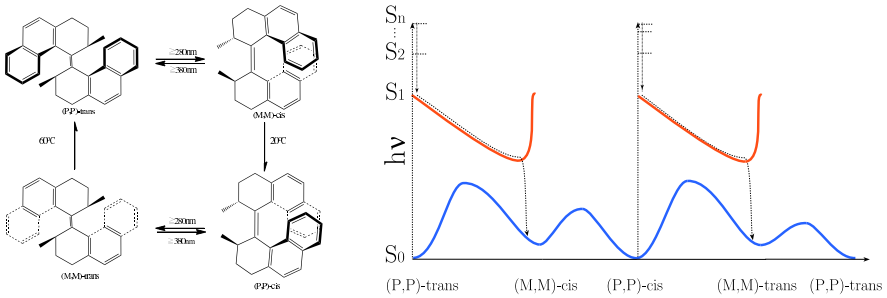

Figure 1.2: *The first generation light-driven molecular motors [16] and the schematic potential energy curves of the ground and lowest excited singet states in a light-driven system.*

The potential energy curves shown in Fig. 1.2 illustrate that in order to achieve a continuous motion, in case of photo-induced reactions, in addition to an asymmetric ground state barrier one should anticipate a well in the excited state with its minimum shifted towards the product. The picture represents, however, a simplified model and misses some dynamic aspects that will be clarified in further sections.

1.2 Photoisomerization

The concept of photoisomerization is rooted in the alternations of electronic structures of molecules. Excitation of an electron from a bonding to an antibonding orbital leads to changes of the equilibrium geometry of a molecule. As a result of steric interactions the dihedral angles differ appreciably in the different electronic states of the

molecule. Experimentally it is easier to observe the spectra of molecules that absorb in the UV/VIS region. Usually the electronic transitions in this region are due to $\pi \rightarrow \pi^*$ or $n \rightarrow \pi^*$ excitations. Unsaturated organic compounds, i.e. compounds with multiple (π) bonds represent therefore the most important class of compounds from both experimental and theoretical points of view. Of particular interest are systems that upon excitation and subsequent decay to the ground state end up in a new conformation, i.e. the ones that are capable of undergoing a chemical conversion initiated by absorption of a photon. The most common type of molecules that possess such properties are biradicals that are characterized by a pair of nearly degenerate nonbonding orbitals occupied by two electrons in a molecular orbital (MO) model. The examples of perfect biradicals are, e.g. a dissociated H_2 molecule and 90° twisted ethylene. It has been established that biradicaloids (near biradicals) undergo ultrafast radiationless transitions from the excited state to the ground state. Because of lack of a ground state minimum (or presence of a shallow one) biradicaloids convert to a non-biradicaloid species after relaxation in the electronic ground state.

Conjugated π systems such as polyenes and aromatic conjugated compounds belong to the most prevalent type of organic systems where biradicaloid behavior can be observed. The light-induced C=C double bond isomerization that proceeds via the dissociation of the π bonds is referred to as photoisomerization and represents the most efficient way to convert light into a mechanical motion. The photoisomerization in retinal chromophore governs the first step in the mechanism of vision in vertebrates.

A broad outline of a typical photochemical reaction in an unsaturated organic molecule can be cast into four steps:

1. through absorption of a photon the molecule undergoes a $\pi \rightarrow \pi^*$ transition
2. the C=C double bond breaks and isomerizes
3. at a certain point the system decays to the ground state
4. the molecule equilibrates on the ground state potential energy surface, possibly in a new conformation.

Experimentally it is very difficult to observe biradicaloids especially in the singlet excited state due to their fast decay to the ground state. With modern spectroscopic methods it became possible to trace the excited state reaction paths while the information about excited state stationary structures is still beyond reach of experimental techniques. A careful description of the mechanisms that underly light-induced conversion of photosensitive systems requires not only information about excited state

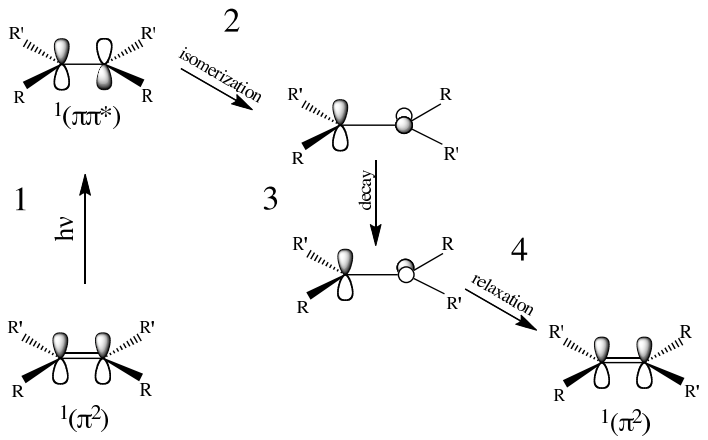

Figure 1.3: *Chart of alkene photoisomerization*

reaction paths and ground state product yields (that can be retrieved by usual chemical methods) but also a simultaneous detailed knowledge about the ground and excited state properties, such as relative energies, geometries etc.

Theoretical investigations on the other hand not only endeavor to elucidate the subtleties of the mechanism but also offer ideas to design new compounds which possess the desired properties.

1.3 Methods of description

The photo-induced reactions are inherently non-classical, therefore from the very first step, in the chart of isomerization mentioned above, quantum mechanical treatment is necessary. The full quantum mechanical description is limited, however, to H_2^+ molecule in approximation of clamped nuclei (the so-called Born-Oppenheimer approximation). Therefore a number of approximations are accepted to make solving the problem feasible.

The approximations to a quantum mechanical description of molecules are called quantum chemical (QC) methods. Certain QC methods use approximations that allow for a systematic extension of precision and do not contain (or contain a very few) empirical parameters. These approaches are called *ab initio* methods. Others that are based on the knowledge of a particular set of molecules or phenomena and

incorporate a large number of empirical parameters are called semiempirical methods. The quantum chemical methods are briefly sketched in the next section and widely used methods will be explained in more detail in the Chapters 2, 3.

The widely accepted first approximation to the description of quantum systems is the concept of potential energy surfaces (PES) of the ground and excited states. The PESs are calculated using a quantum chemical method by optimizing the geometry of molecule with only a limited number of internal coordinates kept fixed to certain values along a possible reaction path. The most obvious, and until quite recently, treated as the main coordinate of isomerization in alkenes, is the torsional angle of C=C bond that undergoes isomerization. The PESs of ground S_0 and excited S_1 singlet states along the torsional angle are depicted in Fig. 1.2. This is intrinsically a simplified model because i) the motion along a given coordinate with all others optimized is clearly an ideal case where the system has sufficient time to relax at each given point, i.e. essentially an adiabatic motion (in fact the process is dynamic and should be described by solving equations of motion, quantum, or in certain cases classical), ii) the one-dimensional model in many cases leads to a biased description excluding deformations that might bring the system to points of true degeneracy of PESs - the so-called conical intersections which are believed to be the most efficient channels for relaxation to ground state, [17] iii) PES itself is a notion emerging from the Born-Oppenheimer approximation implying an adiabatic process in the sense that electron clouds instantly follow the motion of the nuclei, which, however, may fail, e.g., in the region of decay. This implies that the nuclei must be treated on equal footing with electrons in the region of possible decay, such as conical intersections and avoided crossings with sufficiently small energy gaps.

1.4 Review of studies of photoisomerization in alkenes.

One of the pioneers in studying the process of photoisomerization in retinal, Warshel performed in 1976 a semi-classical dynamics simulation with nonadiabatic state transitions. He inferred a peculiar "bicycle pedal" motion of the molecule to explain the fast photoisomerization observed experimentally of $\lesssim$ 6ps [5] (limiting resolution in those days). Apart from the suggested mechanism of isomerization Warshel found that the isomerization proceeds at ca. 200 fs which agrees with the modern experimental data.

Early discussions of photoisomerization were based on chemists empirical knowledge using correlation diagrams. An exhaustive study of photochemical reactions in alkenes, and specifically biradicaloid species was carried out by Salem in early 70's.

[18] On the basis of correlation diagrams and using the Unrestricted Hartree-Fock (UHF) method he calculated potential energy curves for the isomerization in small alkenes. He pointed out the basic scenarios of photoisomerization in model systems such as ethylene, butadiene and hexatriene paying special attention to the mechanism of radiationless decay through crossing of the ground and excited state curves. While the possibility of surface crossing in molecules apart from symmetry reasons [19] has first been illustrated by Herzberg and Longuett-Higgins, [20] Salem focused on the reasons behind such crossings based on molecular orbitals (MO) model. [18]

In the study of protonated Schiff Base (PSB) photoisomerization Salem [21] attributed the experimentally observed [5] fast photoisomerization to the "sudden polarization" that favors a crossing between the ground and excited states surfaces. Although graphic and intuitive, the qualitative description by Salem lacked strong quantitative grounds that were not within reach of quantum chemical methods at that time. The phenomenon of "sudden polarization" was studied then using UHF method followed by a diagonalization of 3X3 configuration interaction (CI) matrix. [22] The relatively simple approaches such as Restricted Hartree-Fock (RHF) or UHF do not account for dynamic and static electron correlation both of which are crucial for the description of the photoisomerization in alkenes. Rather small basis sets used at that time that lacked polarization functions were quite inaccurate in treating the excitation energies. The formally exact is the Full CI (FCI) method that takes all dynamic and static electron correlation into account. Unfortunately FCI is only applicable to atoms or molecules with few electrons. Truncated versions of FCI that include only single, double .. excitations, CIS, CISD, etc are less demanding, however the applications to middle-sized molecules, are restricted to the CIS method which was extensively used for characterization of excited state reactions. However, CIS may only be used to describe states dominated by singly excited configurations from a closed shell ground state, which is rarely the case in the photoisomerization of alkenes as was noted in the discussion of biradicaloids in the previous section. Besides, truncated CI methods lack size consistency which may lead to artefacts in the description of photodissociation processes. Another common method for description of excited states, TDDFT in its standard implementation [23] has the similar deficiency as the CIS method and can not therefore describe all aspects of photoisomerization. [24]

The development of Complete Active Space SCF (CASCF) and corrected to the second order of perturbation theory (CASPT2) methods made it for the first time possible to accurately treat the electronic excited states in a variety of molecular systems. [24] The study of paradigmatic systems such as ethylene, butadiene and hexatriene carried out at the CASSCF/PT2 level has characterized the accurate excitation energies and the ordering of the lowest excited states. [25] It has been demonstrated that the correct ordering of excited states is very sensitive to the dy-

namic electron correlation. Specifically, the importance of dynamic correlation for description of states dominated by ionic valence structures was emphasized. Since the lowest singlet excited state in alkenes has the ionic character, it is clear, that an adequate treatment of photoisomerization in such a case can only be achieved with the use of highly correlated methods.

Despite the success of applying CASPT2 to many important situations from a quantum chemical point of view, the method has several limitations. First, it shouldn't be taken for granted that CASPT2 is always the best method of choice (although quite often CASPT2 can be in an excellent agreement with experimental and higher level methods) because the dynamic correlation is accounted for to the second order of perturbation theory and subtle effects can be overlooked in difficult situations. [24] Secondly, it is only applicable to small systems because of computational constraints. And finally the molecular structure optimization can be quite tedious because of the need to track the active space at different geometries.

The CASSCF method, on the other hand, although less demanding than CASPT2 should be used with precaution. It is already well established that in, e.g. longer polyenes such as for instance PSB, the bond length alternation (BLA) pattern obtained by CASSCF geometry optimization is at a variance with that obtained by CASPT2. [26–28] Methods that incorporate only static and lack dynamic correlation (e.g. CASSCF) tend to overestimate the dominant resonance in the valence bond structure which results in the overestimated charge localization and BLA. In contrast, density functional theory (DFT) with LDA/GGA exchange-correlation functionals tends to delocalize uncompensated charge in longer conjugated systems and underestimates BLA. [29, 30]

To take into account dynamic correlation in CASSCF, Boggio-Pasqua and coworkers proposed [31] using the Restricted Active Space SCF (RASSCF) [32] method with a specific recipe for extension of the active space and introducing special basis functions. The vertical excitation energies obtained after the suggested modifications were in a good agreement with highly correlated methods such as CASPT2, Multireference CI (MRCI) and Multireference Moller-Plesset (MRMP). The shortcomings of the proposed method are first, the specific nature of the choice of active space, and an unstable convergence.

Another widely used alternative approach to incorporate dynamic correlation in CASSCF calculations is to perform geometry optimizations at CASSCF (or state-average CASSCF: SA-CASSCF) followed by single point energy evaluation with such methods as TDDFT or CASPT2. [33–38] This strategy allows one to study moderate-sized systems such as, e.g. PSB or stilbene.

Polarized molecules such as, e.g. PSB are very susceptible to the environment. The effects of an environment on the mechanism of photoisomerization can be as-

sessed by, e.g. considering charged sites of the encompassing cavity (for instance chloride counterion in case of rhodopsin [39]) and studying the changes in the landscapes of photoisomerization pathways. From the relative disposition of the Franck-Condon (FC) point, conical intersections and possible barriers in between, certain conclusions may be drawn about the efficiency and character of photoisomerization. Cembran and co-authors [39] illustrated the effect of a particular localization of positive excess charge in PSB (which depends on the character of electronic state) on the stabilization or destabilization of an S_1 state depending on the certain placement of the counterion. As a consequence of the (de)stabilization of the S_1 state, the conical intersection point between S_0 and S_1 is displaced and new intersections between S_1 and S_2 occur. Such rearrangements were shown to lead to a much slower reaction in agreement with experimentally observed slow deactivation of retinal in a polar solvent.

Since the unbalanced description of static and dynamic correlation will be more pronounced in case of the degeneracy of leading electronic configurations, the strategy of CASSCF geometry optimization and subsequent calculation of energy profiles by highly correlated methods should be used with care, as the technique applies to systems that follow excited reaction paths lying entirely in regions where the molecule exhibits a closed-shell ground state as is the case in PSB photoisomerization (see Ref [38] and references therein). This is especially important when for the correlated method one employs TDDFT.

To summarize, the mechanistic picture of photoisomerization can be assessed with the aid of a PES and minimum energy paths (MEP) in the ground and excited states. These are calculated with the help of either pure quantum chemical approaches or using hybrid schemes

1) geometries are optimized by a relatively inexpensive *ab initio* method followed by evaluation of S_0 and S_1 states PESs by a higher level *ab initio* method. [40–42]

2) quantum chemical energies are obtained at geometries optimized using a classical force field. [43–46]

3) ground and excited PESs are evaluated quantum chemically at geometries taken from "snapshots" from a preceding MD simulation. [26, 47, 48]

Photoisomerization is, however, characterized by many factors, among which are the vertical excitation energy, time delay of deactivation, quantum yield (QY) of a product and photostationary state (PSS) (i.e. an equilibrium mixture of, e.g. cis/trans conformers under specific radiation). Whereas the vertical excitation energy can be directly calculated with the help of quantum chemical methods, and quantum yield can be qualitatively estimated by investigation of PES landscapes and positions/topology of conical intersections, [49] the quantitative characterization of QY and PSS can only be achieved by performing molecular dynamics (MD)

simulations.

The incorporation of non-classical effects and the calculation of excited states in a dynamics simulation can be performed by a variety of techniques which can be roughly divided into the three categories

1) QM/FF/MD schemes employing ground and excited states force fields parameterized to the corresponding *ab initio* PESs, which are subsequently used in classical MD simulations; [50]

2) methods that use classical trajectories, such as, e.g. the Surface Hopping Molecular Dynamics (SHMD) method by Fabiano, Keal, and Thiel, [51] or the Direct Trajectory with Surface Hopping (DTSH) approach by Granucci, Persico and Toniolo, [52] in which the PESs are calculated using a semiempirical Hamiltonian;

3) schemes with simultaneous quantum mechanical treatment of electrons and nuclei such as the Ab Initio Multiple Spawning (AIMS) method by Ben-Nun and Martinez, where the nuclear wave functions are expanded in a fixed basis of frozen gaussians. [53–55]

The first method is conceptually simple and can be treated as a plausible first approximation to the realistic dynamics in which quantum effects are introduced via a specific parameterization of the force fields. The nonadiabatic effects near a conical intersection can be taken into account by i) referring to the nonadiabatic coupling matrix elements in the regions with a narrow energy gap ii) taking as a measure of transition probability the energy gap itself or iii) estimating the proximity to the conical intersection geometries obtained beforehand. By a certain choice of criteria in particular cases plausible results can be obtained which makes the technique a quite specific, albeit a simple method.

In the second method the nonadiabatic effects are evaluated "on the fly". The method is nowadays the most prevalent due to its favorable cost/accuracy balance.

The third scheme appears to be the most realistic one as it explicitly incorporates nuclear degrees of freedom by solving the full time-dependent Schrödinger equation.

1.5 Objectives and outline of this thesis

The objective of this thesis is a theoretical study of the mechanisms and dynamics of synthetic light-driven rotary molecular motors.

Light-driven molecular rotary motors derived from chiral overcrowded alkenes [56–68] are a key class of compounds that utilize sequential photochemical and thermal rearrangements in their operation. The mode of action of these molecular motors is based on the periodic repetition of photo-isomerization and thermal relaxation steps (see 1.1b) that lead to unidirectional rotation of one part of the molecule (rotor) with respect to another (stator). [56–59] To date empirical studies and judicious synthetic

modifications have allowed for a very high degree of control over the thermal step limited rotation speed (*ca.* 10^8 times) through the lowering of the activation energy of the thermal helix inversion. [60–62] The photo-isomerization step however still remains poorly understood and less amenable to prediction with regard to the effect of synthetic modifications. The effect of various factors, such as substituents and hetero-atoms introduced in the rotor and the stator parts, [63] the effect of environment, [69] on the dynamics of photorearrangement and on the geometric transformations that the motor undergoes need to be considered to be able to improve the design of molecular motors.

The light-driven rotary molecular motors have not so far been extensively studied theoretically. To the best of our knowledge, apart from model systems, there is a handful of works in this area.

The effect of substituents are very important in molecular motors. It is appealing to address the question of the relation between preferred direction of rotation and the chemical factors responsible for that. Sampedro and co-workers studied a locked polyenal Schiff base and its chiral derivative using the CASSCF/CASPT2 strategy discussed above. It was found that the reaction paths of both species proceed via conical intersections located at ca. $\pm 90^\circ$ C=C torsion, however the FC point in the chiral derivative is shifted toward one of two CIs thereby making one of the directions of rotation during decay more preferable.

A QM/MM study of first-generation molecular rotor **1** was carried out by Gerrit Groenhof with the help of the ONIOM method by the use of CASSCF/AM1/MM hybrid scheme. [70] The QM/MD simulations demonstrated a unidirectional photoisomerization proceeding during ca. 1.5 ps. In the ONIOM scheme the total system is divided into parts which can be treated at different levels of theory. Although, ONIOM represents a computationally efficient scheme, the application of the method is only justified when every part is adequately described by the corresponding method, which however is not obvious in, e.g. applying semiempirical methods such as AM1 to the description of double bond breaking process.

Grimm and co-workers employed the Spin-Restricted Open-Shell Kohn Sham (ROKS) method for the study of the potential energy curves of the first generation light-driven molecular motor in the S_0 and S_1 states [71] and carried out Car Parinello Molecular Dynamics (CPMD) simulations of the photoisomerization cycle [72] where it was shown that the photoisomerization proceeds preferably in one direction and the delay time of deactivation was estimated to be less than 1 ps. The ROKS scheme used in their work is, however, not suited for the description of bond breaking processes and avoided crossing regions.

To summarize, we list the main prerequisites for the proper study of photoisomerization in alkene-based light-driven molecular rotors: i) The double-bond breaking

and regions of conical intersection must be treated adequately. Therefore, methods that are capable of describing static electron correlation must be used. ii) Ionic character of the lowest excited singlet state lies predominantly in the regions where the ground state has a biradicaloid character. Therefore, to obtain proper geometries and PESs it is necessary to employ methods with a balanced description of static and dynamic correlation. iii) The size of the molecular rotors is prohibitive for highly correlated methods such as, e.g. CASPT2, therefore alternative approaches must be used. iv) The photoisomerization dynamic aspects must be studied to explain the experimentally observed quantum yield of a given rotamer and photostationary state (PSS).

As opposed to the highly correlated wave function based methods, DFT methods scale favorably with the system size, which makes them applicable to large compounds. However the standard implementations of DFT and TDDFT do not meet the requirements i) and ii). Therefore one calls for alternative DFT-based approaches. In Chapter 3 we discuss variants of DFT and in Chapter 4 we propose the State-Averaged Ensemble-Referenced Kohn-Sham (SA-REKS) method that is capable of proper description of the S_0 and S_1 states PESs in the avoided crossings regions and near conical intersections. The SA-REKS method is applied to the calculation of S_0 and S_1 PESs of model systems in Chapter 4 and the first generation light-driven molecular motor in Chapter.5

The incorporation of quantum effects into the description of photoisomerization dynamics is computationally expensive. Consequently, we resort to a SA-REKS/FF/MD strategy described in Chapter.6 To assess the quantum yield and PSS, MD simulations are carried out based on the PESs of the ground and excited states. Surface hoppings are controlled by the proximity of the MD structures to the CI structures.

In Chapter 8 we carry out the semiempirical configuration-interaction MNDO/MRCI [73] study of the PESs in the S_0 and S_1 states and perform optimization of conical intersection (CI) structures and CI seams. The so obtained PESs and CI structures are used for subsequent MD simulations in the similar vein as the ones with the SA-REKS method.

To further validate the application of SA-REKS method to the description of photoisomerization processes we calculate the non-adiabatic coupling (NAC) matrix elements and perform optimization of conical intersection structures (Chapter 7).

Chapter 2

Wave function methods

2.1 Schrödinger equation

A non-relativistic quantum system is described by the Schrödinger equation (SE)

$$i\frac{\partial \Psi}{\partial t} = \hat{H}\Psi \tag{2.1}$$

where the Hamiltonian $\hat{H}$ is a sum of the kinetic $\hat{T}$ and potential $\hat{V}$ energy operators of the system, and Ψ is the wavefunction of the system. The energy of the system is given as the expectation value of the Hamiltonian

$$E = \langle \Psi | \hat{H} | \Psi \rangle \tag{2.2}$$

As long as the potential energy $\hat{V}$ is time-independent, the total wavefunction of the system can be represented by a product of a time-independent wavefunction and an exponential phase factor. From the expression (2.2) it follows that the energy is independent of the phase factor. Therefore the system with stationary potential $\hat{V}$ can be described by the time-independent SE:

$$\hat{H}\Psi = E\Psi \tag{2.3}$$

This is the case when, e.g. one considers electronic system without external fields or with constant/slow varying ones.

2.2 Born-Oppenheimer approximation

Consider a system with the Hamiltonian

$$\begin{aligned} \hat{H} &= -\sum_k \frac{\nabla_k^2}{2M_k} - \sum_i \frac{\nabla_i^2}{2} + \sum_{k<l} \frac{Z_k Z_l}{\mathbf{R_{kl}}} + \sum_{i<j} \frac{1}{\mathbf{r_{ij}}} - \sum_{i,k} \frac{Z_k}{\mathbf{r_{ik}}}, \\ &= \hat{T}_{nuc} + \hat{T}_{el} + \hat{V}_{nuc}(\mathbf{R}) + \hat{V}_{el}(\mathbf{r}) + \hat{V}(\mathbf{r}, \mathbf{R}) \end{aligned} \tag{2.4}$$

here k, l are nuclear indices, $i, j-$ the electronic indices, Z_k is the atomic number of the k-th atom, $\mathbf{r_{ij}}$ are the electronic separations, and $\mathbf{R_{kl}}$ the internuclear separations.

The exact solution of the SE is only possible for a two-body system. Consequently, a quantum treatment of many-electronic and many-atomic systems requires certain approximations to be made. The differential equation (2.3) with the Hamiltonian (2.4) can be simplified by separating the variables. The separation of nuclear and electronic motions is performed using the Born-Oppenheimer approximation which consists of partitioning the total wavefunction into a product of nuclear and electronic wavefunctions

$$\Psi(\mathbf{R}, \mathbf{r}) = \chi(\mathbf{R})\Phi(\mathbf{r}; \mathbf{R}) \tag{2.5}$$

where the semicolon symbolizes a parametric dependence on $\mathbf{R}$. This partitioning is valid in many situations because nuclei are heavier than electrons by a factor of $10^3 \div 10^5$. With the wavefunction (2.5) the SE (2.3) can be split into the electronic and nuclear components:

$$[\hat{T}_{el} + \hat{V}_{el}(\mathbf{r}) + \hat{V}(\mathbf{r}, \mathbf{R})]\Phi(\mathbf{r}; \mathbf{R}) = E_{el}(\mathbf{R})\Phi(\mathbf{r}; \mathbf{R}), \tag{2.6}$$

$$\left[\hat{T}_{nuc}(\mathbf{R}) + E_{el}(\mathbf{R}) + \hat{V}_{nuc}(\mathbf{R})\right]\chi(\mathbf{R}) = E\chi(\mathbf{R}) \tag{2.7}$$

Solution of the electronic SE yields the electronic wavefunction $\Phi(\mathbf{r}; \mathbf{R})$ and the energy E_{el} which depends on the relative positions of the nuclei, therefore the nuclei can be considered as moving in an effective electronic field. The function $E_{el}(\mathbf{R}) + \hat{V}_{nuc}(\mathbf{R})$ in eqution (2.7) is called the potential energy surface (PES). From now on we will mainly be focused on the electronic part of the problem, assuming the BO approximation to be valid everywhere except special situations discussed in Chapters 6, 7, 8.

2.3 Many-electron wavefunction

The electronic wavefunction of a many-electron system depends on the coordinates of all electrons. To solve the electronic SE (2.6) one needs to further partition the many-electron wavefunction into a product of one-electron wavefunctions. However, such a product does not carry an information about the type of particle statistics. The correct wavefunction of N electrons must be antisymmetric to interchange of two electrons and depend on both the spatial and spin coordinates. The simplest antisymmetric wavefunction describing the ground state of an N-electron system is a

single Slater determinant (SD)

$$\Phi_0(\mathbf{x_1}, \mathbf{x_2}, ..., \mathbf{x_N}) = \frac{1}{\sqrt{N!}} \begin{vmatrix} \psi_1(\mathbf{x_1}) & \psi_2(\mathbf{x_1}) & \dots & \psi_N(\mathbf{x_1}) \\ \psi_1(\mathbf{x_2}) & \psi_2(\mathbf{x_2}) & \dots & \psi_N(\mathbf{x_2}) \\ \vdots & \vdots & \ddots & \vdots \\ \psi_1(\mathbf{x_N}) & \psi_2(\mathbf{x_N}) & \dots & \psi_N(\mathbf{x_N}) \end{vmatrix} = |\psi_1 \psi_2 \dots \psi_N\rangle, \tag{2.8}$$

where the one-electron wavefunctions $\psi_i(\mathbf{x_i})$ are called spin orbitals. The coordinates $\mathbf{x_j}$ represent combined coordinates $\mathbf{x_j} = \{\mathbf{r_j}, \sigma\}$, with $\mathbf{r}$ the spatial and σ the spin coordinate: α or β. The spin-orbitals are then given by a product of the spatial orbital $\varphi^\sigma(\mathbf{r})$ and the spin function $\omega(\sigma)$:

$$\begin{aligned} \psi_i(\mathbf{x_j}) &= \varphi_i(\mathbf{r_j})\omega_i(\alpha) \\ \bar{\psi}_i(\mathbf{x_j}) &= \bar{\varphi}_i(\mathbf{r_j})\omega_i(\beta) \end{aligned} \tag{2.9}$$

Approximate solutions to the electronic SE can be obtained using the variational principle which states that the best wavefunction approximated with the single Slater determinant (2.8) is the one that minimizes the energy

$$E_0 = \langle \Phi_0 | \hat{H}_{el} | \Phi_0 \rangle \tag{2.10}$$

The energy of a single determinant is expressed as [74]

$$\begin{aligned} E[\Phi] &= \langle \Phi | \hat{H}_{el} | \Phi \rangle \\ &= \sum_i \langle \psi_i | \hat{h} | \psi_i \rangle + \frac{1}{2} \sum_{i,j} [\langle ij|ij\rangle - \langle ij|ji\rangle] \\ &= \sum_i h_{ii} + \frac{1}{2} \sum_{i,j} [J_{ij} - K_{ij}], \end{aligned} \tag{2.11}$$

where J_{ij} and K_{ij} are called the Coulomb and exchange integrals, respectively.

2.4 Hartree-Fock equations

The first variation of the energy expression (2.11) reads

$$\begin{aligned} \delta E[\Phi] = & \\ &= \sum_i \langle \delta\psi_i | \hat{h} | \psi_i \rangle + \frac{1}{2} \sum_{i,j} [\langle \delta\psi_i \psi_j | \frac{1}{\mathbf{r_{ij}}} | \psi_i \psi_j \rangle - \langle \delta\psi_i \psi_j | \frac{1}{\mathbf{r_{ij}}} | \psi_j \psi_i \rangle] + c.c. \\ &= \sum_i \langle \delta\psi_i | \hat{h} + \hat{J} - \hat{K} | \psi_i \rangle + c.c. \\ &= \sum_i \langle \delta\psi_i | \hat{F} | \psi_i \rangle + c.c., \end{aligned} \tag{2.12}$$

where $\hat{F}$ is referred to as the Fock operator, the one-electron core Hamiltonian $\hat{h}$ is given by

$$\hat{h} = \hat{T}_{el} + \hat{V}(\mathbf{r}, \mathbf{R}) \tag{2.13}$$

The Coulomb $\hat{J}$ and exchange $\hat{K}$ operators are defined as

$$\hat{J}_j(\mathbf{x_1})\psi_j(\mathbf{x_1}) = \big[\int |\psi_i(\mathbf{x_2})|^2 \frac{1}{\mathbf{r_{12}}} d\mathbf{x_2} \big] \psi_j(\mathbf{x_1}) \tag{2.14}$$

$$\hat{K}_j(\mathbf{x_1})\psi_j(\mathbf{x_1}) = \big[\int \psi_i^*(\mathbf{x_2})\psi_j(\mathbf{x_2}) \frac{1}{\mathbf{r_{12}}} d\mathbf{x_2} \big] \psi_i(\mathbf{x_1}) \tag{2.15}$$

From (2.12) it is seen that for $E[\Phi]$ to be stationary, the term in the last line must vanish

$$\langle \delta\psi_1 | \hat{F} | \psi_i \rangle = 0 \tag{2.16}$$

Expanding $\delta\psi_i$ in a complete set of occupied ψ_i (which drop out as their variations leave the Φ invariant) and virtual ψ_s orbitals, and substituting into the above condition, one arrives at the general Hartree-Fock equations

$$\langle \psi_s | \hat{F} | \psi_i \rangle = 0, \tag{2.17}$$

which can be rewritten as

$$\hat{F}\psi_i = \sum_j \lambda_{ji}\psi_j \tag{2.18}$$

or after diagonalization,

$$\hat{F}\psi_j = \varepsilon_j \psi_j, \tag{2.19}$$

where ε_j is called the orbital energy.

The energy E can be written in terms of orbital energies, the Coulomb and exchange operators

$$E = \sum_i \varepsilon_i - \frac{1}{2} \sum_i \langle \psi_i | \hat{J} - \hat{K} | \psi_i \rangle \tag{2.20}$$

2.5 RHF, UHF, ROHF

The Hartree-Fock approximation is based on a single-determinantal wavefunction (2.8). Since the non-relativistic Hamiltonian does not explicitly act on the spin functions, it must commute with spin operators. Therefore, the eigenfunctions of

$\hat{H}$ must also be the eigenfunctions of the spin operators. Consequently, the many-electron wavefunction should satisfy

$$\hat{S}^2\Psi = S(S+1)\Psi \tag{2.21}$$
$$\hat{S}_z\Psi = M_S\Psi \tag{2.22}$$

The simplest case satisfying the requirements (2.21,2.22) is the closed-shell where $S = M_S = 0$. The spin orbitals of paired electrons have in this case the same spatial parts

$$\begin{aligned}\psi_i(\mathbf{x}) &= \varphi_i(\mathbf{r})\alpha \\ \bar{\psi}_i(\mathbf{x}) &= \varphi_i(\mathbf{r})\beta\end{aligned} \tag{2.23}$$

Substitution of (2.23) into (2.20) then yields the restricted Hartree-Fock (RHF) energy

$$E^{RHF} = 2\sum_{i=1}^{N/2}(i|\hat{h}|i) + \sum_{i=1}^{N/2}[2(ii|jj) - (ij|ij)] \tag{2.24}$$

and the Fock operator

$$\hat{F}^{RHF} = \hat{h} + 2\sum_{i=1}^{N/2}\hat{J}_i - \sum_{i=1}^{N/2}\hat{K}_i \tag{2.25}$$

If the electrons are not strictly paired, i.e. the spatial parts in (2.23) are different for the α and β electrons, the condition (2.22) is still satisfied, however the condition (2.21) is no longer obeyed. Substituting now

$$\begin{aligned}\psi_i(\mathbf{x}) &= \varphi_i(\mathbf{r})\alpha \\ \bar{\psi}_i(\mathbf{x}) &= \bar{\varphi}_i(\mathbf{r})\beta\end{aligned} \tag{2.26}$$

into the general expression for the determinantal energy (2.11) one obtains the expression for the unrestricted Hartree-Fock (UHF) energy

$$\begin{aligned}E^{UHF} = &\sum_i \langle i|\hat{h}|i\rangle + \frac{1}{2}\sum_{i^{(\alpha)},j^{(\alpha)}}\langle ij||ij\rangle \\ &+ \frac{1}{2}\sum_{i^{(\beta)},j^{(\beta)}}\langle ij||ij\rangle + \frac{1}{2}\sum_{i^{(\alpha)},j^{(\beta)}}\langle ij|ij\rangle\end{aligned} \tag{2.27}$$

The UHF Fock operators are now distinct for the α and β orbitals

$$\begin{aligned}\hat{F}^{\alpha} &= \hat{h} + \hat{J} - \hat{K}^{\alpha} \\ \hat{F}^{\beta} &= \hat{h} + \hat{J} - \hat{K}^{\beta},\end{aligned} \tag{2.28}$$

where

$$\hat{K}^{\alpha} = \sum_{i^{(\alpha)}} \hat{K}_i; \quad \hat{K}^{\beta} = \sum_{i^{(\beta)}} \hat{K}_i \tag{2.29}$$

Alternatively, one can formulate the Hartree-Fock method for the open-shell case by restricting the spatial parts in (2.26) to be equal. The approach is called the restricted open shell Hartree-Fock (ROHF) method. In the ROHF method the open-shell and closed-shell orbitals are added together and the resulting wavefunction is then projected to possess the correct spin and space symmetry. In some cases this leads to a wavefunction consisting of more than one Slater determinant. For instance the open shell singlet state is represented by the linear combination of the two determinants with singly occupied frontier orbitals

$$\Theta = \frac{1}{\sqrt{2}} \left(|\psi_1 \bar{\psi}_1 \psi_2 \bar{\psi}_2 ... \psi_{N/2} \bar{\psi}_{N/2+1}\rangle + |\psi_1 \bar{\psi}_1 \psi_2 \bar{\psi}_2 ... \bar{\psi}_{N/2} \psi_{N/2+1}\rangle \right), \tag{2.30}$$

where N is the number of electrons.

Consider a Slater determinant constructed of n_c closed-shell orbitals and n_o singly occupied orbitals with α spin:

$$\Phi = |\psi_1 \bar{\psi}_1 ... \psi_{n_c} \bar{\psi}_{n_c} \psi_{n_c+1} ... \psi_{n_c+n_o}\rangle \tag{2.31}$$

Accepting the following labeling of the orbitals,

$$\begin{aligned} i, j, k - &\text{ closed shell (doubly occupied orbitals)} \\ s, t, u - &\text{ open shell (fractionally occupied orbitals)} \\ a, b, c - &\text{ virtual orbitals} \end{aligned} \tag{2.32}$$

the energy (2.27) can be expressed as

$$\begin{aligned} E^{ROHF} = &\sum_i (i|\hat{h}|i) + 2f \sum_s (s|\hat{h}|s) + \sum_{i,j} [2(ii||jj) - (ij|ij)] \\ &+ 2f \sum_{i,s} [2(ii||ss) - (is|is)] + f^2 \sum_{s,t} [2a(ss||tt) - b(st|st)] \end{aligned} \tag{2.33}$$

The variation of (2.33) leads to the ROHF equations

$$\langle \psi_a | \hat{F}^c | \psi_i \rangle = 0; \quad \langle \psi_a | \hat{F}^o | \psi_s \rangle = 0; \quad \langle \psi_i | \hat{F}^c - f\hat{F}^o | \psi_s \rangle = 0, \tag{2.34}$$

where

$$\begin{aligned} \hat{F}^c &= \hat{h} + \sum_i (2\hat{J}_i - \hat{K}_i) + f \sum_s (2\hat{J}_s - \hat{K}_s) \\ \hat{F}^o &= \hat{h} + \sum_i (2\hat{J}_i - \hat{K}_i) + f \sum_s (2a\hat{J}_s - b\hat{K}_s) \end{aligned} \tag{2.35}$$

2.6 Roothaan-Hall equations

The application of the Hartree-Fock method to the description of molecules is impeded by the lack of spherical symmetry present in atoms. The extension of the approach to treat molecules consists in expanding the molecular orbitals in terms of the basis of atomic orbitals

$$\varphi_i = \sum_{\nu=1}^{K} C_{\nu i}\phi_\nu, i = 1, 2, ...K \tag{2.36}$$

Substituting this expansion into the Hartree-Fock equation (2.19), projecting on a particular ϕ_μ and integrating, we obtain

$$\sum_\nu F_{\mu\nu}C_{\nu i} = \varepsilon_i \sum_\nu S_{\mu\nu}C_{\nu i} \tag{2.37}$$

or in matrix form

$$\mathbf{FC} = \mathbf{SC}\boldsymbol{\varepsilon}, \tag{2.38}$$

where $\mathbf{S}$ is the overlap matrix. The Fock matrix has now the form

$$F_{\mu\nu} = h_{\mu\nu} + \sum_i^{N/2} \sum_{\tau\zeta} C_{\tau i}C^*_{\zeta i}[2(\mu\nu|\tau\zeta) - (\mu\tau|\zeta\nu)] \tag{2.39}$$

Equations (2.38) are called the Roothaan-Hall equations. The Fock matrix explicitly depends on the molecular orbital coefficients, therefore the equation must be solved iteratively.

2.7 Configuration Interaction

The exact many-electron wavefunction can be expanded in terms of all possible N-electron Slater determinants (configurations) constructed from a complete set of spin orbitals ψ as

$$\Psi = c_0|\Phi_0\rangle + \sum_{ir} c_i^r|\Phi_i^r\rangle + \sum_{\substack{i<j \\ r<s}} c_{ij}^{rs}|\Phi_{ij}^{rs}\rangle + \sum_{\substack{i<j<k \\ r<s<t}} c_{ijk}^{rst}|\Phi_{ijk}^{rst}\rangle + ... \tag{2.40}$$

In the configuration interaction (CI) method the series (2.40) is optimized with respect to the expansion coefficients [74] $c_0, c_i^r, ...$ The method becomes exact and is termed complete CI if the spin orbitals are expanded in a complete basis set and all possible configurations are included in the expansion (2.40). If a limited basis

set is used the method is called Full CI. In practice a Full CI calculation is only feasible for small systems such as H_2, He_2, etc. The expansion is usually truncated at singly, doubly, etc. excited configurations, and truncated CI methods are referred to respectively as CIS, CISD, CISDT, etc.

The major disadvantage of the truncated CI methods is the non-size consistency. A method is termed size-consistent if the following relation holds $E_{AB}(r \to \infty) = E_A + E_B$.[75] The lack of self-consistency therefore leads to an incorrect description of processes such as e.g. dissociation. Therefore the method is rarely used nowadays and is replaced by coupled clusters (CC) method [76].

An alternative way to reduce the length of the CI expansion, i.e. to obtain an expansion with a limited number of dominating terms in (2.40) is followed in the so-called multiconfiguration self-consistent method (MCSCF) in which both the expansion coefficients and the orbitals ψ_i are optimized. The MCSCF method is briefly discussed in the following section.

2.8 CASSCF and CASPT2

Multiconfiguration self-consistent field (MCSCF) wavefunction is expanded in terms of spin-adapted configurations also known as configuration state functions (CSF)

$$\Psi = \sum_m C_m |\Theta_m\rangle \tag{2.41}$$

The CSFs $|\Theta_m\rangle$ are, in turn, constructed from ground, singly, doubly, etc excited Slater determinants. It is thus advantageous to formulate the theory in terms of number conserving operators. Define the operators which, acting on a closed shell *vacuum* state, preserve the eigenvalues of $\hat{S}_z$ and $\hat{S}^2$ as

$$\hat{E}_{rs} = a^\dagger_{r\alpha} a_{s\alpha} + a^\dagger_{r\beta} a_{s\beta} \tag{2.42}$$

where $a^\dagger$ is the creation and a the annihilation operators. The operators $\hat{E}_{rs}$ are referred to as generators. A one-electron operator can be written as

$$\hat{h} = \sum_{rs} h_{rs} \hat{E}_{rs}, \tag{2.43}$$

with

$$h_{rs} = \int \phi^*_i(\mathbf{x}) \hat{h}(\mathbf{x}) \phi_j(\mathbf{x}) \mathbf{dx} \tag{2.44}$$

A two-electron operator, in turn, can be expressed as

$$\hat{G} = \sum_{rstu} g_{rstu} (\hat{E}_{rs}\hat{E}_{tu} - \delta_{st}\hat{E}_{ru}) \tag{2.45}$$

where

$$g_{rstu} = \int \varphi_r^*(\mathbf{r_1})\varphi_s(\mathbf{r_1})\frac{1}{\mathbf{r_{12}}}\varphi_t^*(\mathbf{r_2})\varphi_u(\mathbf{r_2})\mathbf{dr_1 dr_2} \tag{2.46}$$

The Hamiltonian can be expressed in terms of the generators as follows

$$\hat{H} = \sum_{rs} h_{rs}\hat{E}_{rs} + \frac{1}{2}\sum_{rstu} g_{rstu}(\hat{E}_{rs}\hat{E}_{tu} - \delta_{st}\hat{E}_{ru}) \tag{2.47}$$

The expectation values of one- and two-electron operators between Slater determinants are given, correspondingly, by

$$\langle\Phi_m|\hat{h}|\Phi_n\rangle = \sum_{rs} h_{rs}\langle\Phi_m|\hat{E}_{rs}|\Phi_n\rangle \tag{2.48}$$

and

$$\langle\Phi_m|\hat{G}|\Phi_n\rangle = \frac{1}{2}\sum_{rstu} g_{rstu}\langle\Phi_m|\hat{E}_{rs}\hat{E}_{tu} - \delta_{st}\hat{E}_{ru}|\Phi_n\rangle \tag{2.49}$$

Since the wavefunction $|\Psi\rangle$ (2.41) is a linear combination of SDs, the matrix elements we need are given in terms of the reduced density matrices of the first and second order, correspondingly by

$$D_{rs} = \langle\Psi|\hat{E}_{rs}|\Psi\rangle = \sum_{mn} c_m^* c_n\langle\Phi_m|\hat{E}_{rs}|\Phi_n\rangle \tag{2.50}$$

and

$$P_{rstu} = \sum_{mn} c_m^* c_n\langle\Phi_m|\hat{E}_{rs}\hat{E}_{tu} - \delta_{st}\hat{E}_{ru}|\Phi_n\rangle \tag{2.51}$$

The expectation value of the Hamiltonian (2.47) can thus be given by

$$E = \langle\Psi|\hat{H}|\Psi\rangle = \sum_{rs} h_{rs}D_{rs} + \sum_{rstu} g_{rstu}P_{rstu} \tag{2.52}$$

The minimization of the energy expression (2.52) is performed through variations in the MO and CI spaces. The unitary transformations of MOs and CI coefficients can be performed by exponential operators of the form

$$e^{-\hat{T}}, e^{-\hat{S}}, \tag{2.53}$$

where the orbital variations are performed by use of

$$\hat{T} = \sum_{r>s} T_{rs}(\hat{E}_{rs} - \hat{E}_{sr}), \tag{2.54}$$

the CI coefficients for the MCSCF wavefunction (2.41) are varied using the operator

$$\hat{S} = \sum_{\kappa \neq \Psi} S_{\kappa\Psi}(|\kappa\rangle\langle\Psi| - |\Psi\rangle\langle\kappa|), \tag{2.55}$$

where $|\kappa\rangle$ is an orthogonal complement to the MCSCF state Ψ. In MCSCF method the rotations in the MO and CI spaces are performed simultaneously by means of the transformation

$$|\Psi'\rangle = e^{\hat{T}} e^{\hat{S}} |\Psi\rangle \tag{2.56}$$

The expectation value of the Hamiltonian in the transformed state is therefore given as

$$E(T,S) = \langle\Psi| e^{-\hat{S}} e^{-\hat{T}} \hat{H} e^{\hat{S}} e^{\hat{T}} |\Psi\rangle \tag{2.57}$$

expanding the exponents in (2.57) one can obtain

$$\begin{aligned} E(T,S) = \langle\Psi|\hat{H} + [\hat{H},\hat{T}] + [\hat{H},\hat{S}] \\ + \frac{1}{2}[[\hat{H},\hat{T}],\hat{T}] + \frac{1}{2}[[\hat{H},\hat{S}],\hat{S}] + \frac{1}{2}[[\hat{H},\hat{T}],\hat{S}] + ...|\Psi\rangle, \end{aligned} \tag{2.58}$$

whence the gradients with respect to T_{rs} and $S_{\kappa\Psi}$ are found

$$g_{rs}^{orb} = \langle\Psi|[\hat{H}, \hat{E}_{rs} - \hat{E}_{sr}]|\Psi\rangle \tag{2.59}$$

and

$$g_{rs}^{CI} = 2\langle\Psi|\hat{H}|\kappa\rangle \tag{2.60}$$

Consequently, for the MCSCF orbitals to be optimal, the gradients (2.59,2.60) must vanish.

In complete active space SCF (CASSCF) implementation the MOs are divided into groups of inactive, active and external orbitals. The inactive orbitals are kept doubly occupied, the external orbitals are unoccupied. The active space contains orbitals with occupation numbers $n = 0 \div 2$. Within the active space all possible configurations are accessible. Therefore CASSCF represents a full CI restricted to the active space. Consequently, the rotations within each subspace leave the total wavefunctions invariant and are thus redundant. The convergence is quadratic and thus very efficient if reasonable starting orbitals are used.

CASSCF calculations on excited states, in cases when interesting states lie close in energy, can lead to complications, such as e.g. root flipping. To circumvent the problem, a starting state is obtained by optimizing an average energy of several states

$$\bar{E} = \sum_i \omega_i E_i. \tag{2.61}$$

After identifying the correct roots, it is then possible to perform calculations of specific roots. This method is referred to as state-averaged CASSCF (SA-CASSCF).

The CASSCF method can take into account the static electron correlation as it is based on multiconfigurational wavefunction. However, it inherits from HF theory the deficiency in being unable to account for dynamic correlation fully. This is usually remedied by taking into account the dynamic correlation with the help of perturbation theory using the CASSCF wavefunction as a reference. In perturbation theory the Hamiltonian is partitioned as

$$\hat{H} = \hat{H}_0 + \lambda \hat{H}_1, \tag{2.62}$$

where $\hat{H}_0$ is the zeroth order Hamiltonian for which the zeroth order wavefunction $|\Psi_0\rangle$ is an eigenfunction with an eigenvalue E_0, and λ is a small parameter defining the perturbation $\hat{H}_1$. The zeroth order Hamiltonian may be constructed in different ways with the requirement that the wavefunction $|\Psi_0\rangle$ represents its eigenfunction. The CASPT2 results can be quite sensitive to the choice of the zeroth order Hamiltonian [77, 78] especially in the regions of crossing of (several) states. For instance it has been shown that the vertical excitations in ethylene may be significantly affected by the presence of crossings with Rydberg states. [79] The inappropriate choice of zeroth-order Hamiltonian and the active space may lead, in certain situations, to the so-called intruder states, which originate from small denominators in the expression for the second-order energy due to (near) degeneracy of the eigenvalues of $\hat{H}_0$. The problem can either be solved by use of the level shift, i.e. an addition of a term $\xi \hat{H}_0$ to $\hat{H}_0$, so as to shift the eigenvalues apart, or by the Multi-State CASPT2 method [80, 81] in which the SA-CASSCF reference is used. An alternative method called n-electron valence state perturbation theory NEVPT2 has recently been proposed [82–84] which has does not suffer from the intruder states issue. [85] The results of (MS)CASPT2 calculations strongly depend on the active space used. Too small an active space may lead to inadequate results. As a consequence, the method is quite expensive when applied to even moderate sized molecules. Another issue is the absence of analytic gradients, which, together with the high cost, makes the method inapplicable to, e.g. optimization of geometry or study of reaction paths in molecules of appreciable size.

Chapter 3

Density Functional Theory

The alternative to wave function methods is density functional theory (DFT) in which the many-electron problem is formulated in terms of the electron density. The number of degrees of freedom is thereby reduced to a minimum as the electron density depends only upon 3 spatial coordinates in contrast to 3N coordinates needed for an N-electron wave function. This offers an opportunity to deal with bigger systems, however it also bears certain limitations in practical implementations.

3.1 Basic Concepts

We start from introducing the density matrices which represent quite general and flexible ansatz for the description of a many-electron problem. Starting from density matrices in most general form it is possible to downgrade subsequently to particular cases needed in specific formulations.

Consider a system with the Hamiltonian

$$\hat{H} = \hat{T} + \hat{V} + \hat{W}, \tag{3.1}$$

where

$$\hat{T} = \sum_{i}^{N} \left(-\frac{\nabla_i^2}{2} \right) \tag{3.2}$$

is the electronic kinetic energy operator,

$$\hat{V} = \sum_{i}^{N} v(\mathbf{r_i}) \tag{3.3}$$

is the energy due to nuclear-electron attraction (the external potential), and

$$\hat{W} = \sum_{i<j}^{N} \frac{1}{\mathbf{r_{ij}}} \tag{3.4}$$

is the electron-electron interaction energy operator. Solutions of the Schrödinger equation

$$\hat{H}\Psi = E\Psi, \tag{3.5}$$

are wave functions $\Psi(\mathbf{x_1 x_2}...\mathbf{x_N})$, where $\mathbf{x_i}$ stands for a product of spin s_i and space $\mathbf{r_i}$ coordinates. The product

$$\Psi^*(\mathbf{x_1 x_2}...\mathbf{x_N})\Psi(\mathbf{x_1 x_2}...\mathbf{x_N})\mathbf{dx_1}...\mathbf{dx_N} \tag{3.6}$$

is the probability of finding the system in the spin-space element

$$[(\mathbf{x_1}...\mathbf{x_N}),\ (\mathbf{x_1}+\mathbf{dx_1}...\mathbf{x_N}+\mathbf{dx_N})]$$

If we integrate (3.6) over all variables except $\mathbf{r_1}$, we obtain the electron density

$$\rho(\mathbf{r_1}) = N\int ...\int |\Psi(\mathbf{x_1 x_2}...\mathbf{x_N})|^2 ds_1 \mathbf{dx_2}...d\mathbf{dx_N}, \tag{3.7}$$

which has the meaning of the number of electrons per unit volume in state Ψ. A more general notion is the so-called N-particle density-matrix defined by

$$\gamma_N(\mathbf{x'_1}...\mathbf{x'_N}, \mathbf{x_1}...\mathbf{x_N}) \equiv \Psi(\mathbf{x'_1}...\mathbf{x'_N})\Psi^*(\mathbf{x_1}...\mathbf{x_N}), \tag{3.8}$$

which is in turn the coordinate representation of the density operator (hereafter we will refer to the density operators and matrices as density matrices)

$$\hat{\gamma}_N \equiv |\Psi_N\rangle\langle\Psi_N|. \tag{3.9}$$

Expectation value of an operator in a pure state is defined by

$$\langle\hat{A}\rangle = tr\left(\hat{\gamma}_N\hat{A}\right). \tag{3.10}$$

In case a system is in a mixed state the complete set of accessible states is described by the N-particle ensemble density matrix

$$\hat{\Gamma}_N = \sum_i p_i|\Psi_i\rangle\langle\Psi_i|, \tag{3.11}$$

where p_i is the probability of finding the system in the state $|\Psi_i\rangle$. The expectation value for an operator $\hat{A}$ in a mixed state in this case is given by

$$\langle\hat{A}\rangle = Tr\left(\hat{\Gamma}_N\hat{A}\right) = \sum_i p_i\langle\Psi_i|\hat{A}|\Psi_i\rangle. \tag{3.12}$$

As we are concerned with the Hamiltonian of the form (3.1) with only one- and two- electron operators, the density matrix can be contracted by integrating out $\mathbf{x_3}, \mathbf{x_4}, ..., \mathbf{x_N}$

$$\begin{aligned}&\gamma_2(\mathbf{x'_1 x'_2}, \mathbf{x_1 x_2})\\ &\quad = \frac{N(N-2)}{2}\int ...\int \Psi(\mathbf{x'_1 x'_2 x_3}...\mathbf{x_N})\Psi^*(\mathbf{x_1 x_2 x_3}...\mathbf{x_N})\mathbf{dx_3}...\mathbf{dx_N}\end{aligned} \tag{3.13}$$

this is the so-called two-particle reduced density matrix. By integrating out $\mathbf{x_2}, \mathbf{x_3}, ..., \mathbf{x_N}$

$$\gamma_1(\mathbf{x'_1}, \mathbf{x_1}) = N \int ... \int \Psi(\mathbf{x'_1 x_2}...\mathbf{x_N})\Psi^*(\mathbf{x_1 x_2}...\mathbf{x_N})\mathbf{dx_2}...\mathbf{dx_N} \tag{3.14}$$

we obtain the one-particle reduced density matrix (or one-matrix). The one-matrix possesses eigenvectors and eigenvalues defined by the equation

$$\int \gamma_1(\mathbf{x'_1}, \mathbf{x_1})\psi_i(\mathbf{x'_1})\mathbf{dx_1} = n_i\psi(\mathbf{x'_1}), \tag{3.15}$$

where n_i are called occupation numbers and $|\psi_i\rangle$ natural spin orbitals. The one-particle density operator can therefore be defined as

$$\hat{\gamma}_1 = \sum_i n_i|\psi_i\rangle\langle\psi_i|, \tag{3.16}$$

The density matrices can be further simplified by summing over the spin coordinates. We are allowed to do this as the considered Hamiltonian does not act on spin coordinates explicitly. Thus we obtain, correspondingly, for the two- and one-particle matrices

$$\rho_2(\mathbf{r'_1 r'_2}, \mathbf{r_1 r_2}) = \frac{N(N-2)}{2} \int ... \int \gamma_2(\mathbf{r'_1}s_1\mathbf{r'_2}s_2, \mathbf{r_1}s_1\mathbf{r_2}s_2)ds_1 ds_2 \tag{3.17}$$

$$\rho_1(\mathbf{r'_1}, \mathbf{r_1}) = N \int \gamma_1(\mathbf{r'_1}s_1\mathbf{r_1}s_1)ds_1 \tag{3.18}$$

We will only need the diagonal part of the two-particle reduced spinless density matrix

$$\rho_2(\mathbf{r_1}, \mathbf{r_2}) \equiv \rho_2(\mathbf{r_1 r_2}, \mathbf{r_1 r_2}). \tag{3.19}$$

Note that the diagonal part of the one-matrix (3.18) is the density (3.7)

$$\rho(\mathbf{r}) = \rho_1(\mathbf{r}, \mathbf{r}). \tag{3.20}$$

For future references it is useful to decompose the density matrices $\rho_1(\mathbf{r'_1}, \mathbf{r_1})$ and $\rho_2(\mathbf{r'_1 r'_2}, \mathbf{r_1 r_2})$ into components of up and down spin densities

$$\rho_1(\mathbf{r'_1}, \mathbf{r_1}) = \rho_1^{\alpha\alpha}(\mathbf{r'_1}, \mathbf{r_1}) + \rho_1^{\beta\beta}(\mathbf{r'_1}, \mathbf{r_1}), \tag{3.21}$$

and

$$\begin{aligned}\rho_2(\mathbf{r'_1 r'_2}, \mathbf{r_1 r_2}) = \rho_2^{\alpha\alpha,\alpha\alpha}(\mathbf{r'_1 r'_2}, \mathbf{r_1 r_2}) + \rho_2^{\beta\beta,\beta\beta}(\mathbf{r'_1 r'_2}, \mathbf{r_1 r_2}) \\ +\rho_2^{\alpha\beta,\alpha\beta}(\mathbf{r'_1 r'_2}, \mathbf{r_1 r_2}) + \rho_2^{\beta\alpha,\beta\alpha}(\mathbf{r'_1 r'_2}, \mathbf{r_1 r_2})\end{aligned} \tag{3.22}$$

For the density $\rho(\mathbf{r})$ we also have

$$\rho(\mathbf{r}) = \rho^{\alpha}(\mathbf{r}) + \rho^{\beta}(\mathbf{r}) \tag{3.23}$$

The energy of the system can be evaluated as the expectation value of the given Hamiltonian in terms of the spinless reduced density matrices (3.18), (3.19) and (3.20)

$$E = \int \left[-\frac{1}{2}\nabla_r^2 \rho_1(\mathbf{r}', \mathbf{r}) \right]_{\mathbf{r}'=\mathbf{r}} \mathbf{dr} + \int v(\mathbf{r})\rho(\mathbf{r})\mathbf{dr} + \int\int \frac{1}{\mathbf{r_{12}}} \rho_2(\mathbf{r_1}, \mathbf{r_2})\mathbf{dr_1 dr_2} \tag{3.24}$$

The most complex term in the energy expression (3.24) is the last one which describes electron-electron interaction. Let us separate out the classical Coulomb part

$$J[\rho] = \frac{1}{2}\int\int \frac{\rho(\mathbf{r_1})\rho(\mathbf{r_2})}{\mathbf{r_{12}}}\mathbf{dr_1 dr_2} \tag{3.25}$$

which is interpreted as an electrostatic interaction of two electronic clouds with densities $\rho(\mathbf{r_1})$ and $\rho(\mathbf{r_2})$. The separation of $J[\rho]$ from the last term in expression (3.24) can be performed as follows

$$\begin{aligned} \int\int \frac{\rho_2(\mathbf{r_1}, \mathbf{r_2})}{\mathbf{r_{12}}}\mathbf{dr_1 dr_2} &= \frac{1}{2}\int\int \frac{\rho(\mathbf{r_1})\rho(\mathbf{r_2})[1 + h(\mathbf{r_1}, \mathbf{r_2})]}{\mathbf{r_{12}}}\mathbf{dr_1 dr_2} \\ &= J[\rho] + \frac{1}{2}\int\int \frac{\rho(\mathbf{r_1})\rho(\mathbf{r_2})}{\mathbf{r_{12}}} h(\mathbf{r_1}, \mathbf{r_2})\mathbf{dr_1 dr_2}, \end{aligned} \tag{3.26}$$

where $h(\mathbf{r_1}, \mathbf{r_2})$ is the pair correlation function. The product $\rho(\mathbf{r_2})h(\mathbf{r_1}, \mathbf{r_2})$ is called exchange-correlation hole

$$\rho_{xc}(\mathbf{r_1}, \mathbf{r_2}) = \rho(\mathbf{r_2})h(\mathbf{r_1}, \mathbf{r_2}), \tag{3.27}$$

and it integrates to -1

$$\int \rho_{xc}(\mathbf{r_1}, \mathbf{r_2})\mathbf{dr_2} = -1, \forall \mathbf{r_1}. \tag{3.28}$$

Thus one can rewrite the energy expression (3.24) as

$$E = \int \left[-\frac{1}{2}\nabla_r^2 \rho_1(\mathbf{r}', \mathbf{r}) \right]_{\mathbf{r}'=\mathbf{r}} \mathbf{dr} + \int v(\mathbf{r})\rho(\mathbf{r})\mathbf{dr} + J[\rho] + E_{xc}[\rho], \tag{3.29}$$

where

$$E_{xc}[\rho] = \frac{1}{2}\int\int \frac{\rho(\mathbf{r_1})\rho(\mathbf{r_2})}{\mathbf{r_{12}}} h(\mathbf{r_1}, \mathbf{r_2})\mathbf{dr_1 dr_2} \tag{3.30}$$

Let us express E_{xc} in the usual way as a sum of exchange and correlation parts

$$E_{xc}[\rho] = E_x[\rho] + E_c[\rho]. \tag{3.31}$$

The simplest approximation to E_{xc} is the so-called Local Density Approximation (LDA) that implies a slowly varying density. The exchange energy in that case is approximated by the statistical expression for a uniform electron gas given by Dirac formula

$$E_x^{LDA}[\rho] = -K \int \rho(\mathbf{r})^{4/3} d\mathbf{r} \tag{3.32}$$

In case if the densities of up and down spins are not equal, the Local Spin Density Approximation (LSD) is given by

$$E_x^{LSD}[\rho] = -2^{1/3} K \int \left[\rho_\alpha^{4/3}(\mathbf{r}) + \rho_\beta^{4/3}(\mathbf{r})\right] d\mathbf{r} \tag{3.33}$$

Analytic expression for the correlation energy is not known except for the high-density and low-density limiting cases. The correlation energy functional form can be obtained by interpolating the empirical data for the intermediate densities and reproducing the limiting densities. [86]

3.2 Hohenberg-Kohn Theory

The first Hohenberg-Kohn (HK) theorem states that the ground state expectation value of the Hamiltonian $\hat{H}$ is a unique functional of the exact density

$$\langle \Psi[\rho]|\hat{H}|\Psi[\rho]\rangle = E[\rho] \tag{3.34}$$

and the ground state density determines the external potential of the system up to a constant. In its original form the HK theorem has been formulated for non-degenerate ground states. We will consider the extensions to degenerate states and excited states in the following sections.

Consider sets of external potentials $\{V\}$, densities $\{\rho\}$ and orthonormal states $\{\Psi\}$. In these terms the theorem essentially asserts that there exist one-to-one correspondences $\{\Psi\} \leftrightarrow \{V\}$ and $\{\Psi\} \leftrightarrow \{\rho\}$. The map $\{\Psi\} \rightarrow \{V\}$ is determined by construction: $v = \langle\Psi|\hat{V}|\Psi\rangle$. One needs to prove the map $\{\Psi\} \leftarrow \{V\}$, i.e. to show that two different potentials $\hat{V}(r) \neq \hat{V}'(r) + const$ lead to different nondegenerate ground states $|\Psi\rangle$ and $|\Psi'\rangle$. Assume $|\Psi\rangle = |\Psi'\rangle$, then we have

$$\left(\hat{T} + \hat{V} + \hat{W}\right)|\Psi\rangle = E_{g.s.}|\Psi\rangle \tag{3.35}$$

and

$$\left(\hat{T} + \hat{V}' + \hat{W}\right)|\Psi\rangle = E'_{g.s.}|\Psi\rangle \tag{3.36}$$

subtracting (3.36) from (3.35),

$$\begin{aligned}\left(\hat{V} - \hat{V}'\right)|\Psi\rangle &= \left(E_{g.s.} - E'_{g.s.}\right)|\Psi\rangle \\ \Rightarrow \hat{V} &= \hat{V}' + const\end{aligned}$$

which contradicts the assumption $\hat{V} \neq \hat{V}' + const$ This confirms the bijective correspondence $\{\Psi\} \leftrightarrow \{V\}$. The HK theorem is formulated for densities that are associated with the antisymmetric ground state function of a Hamiltonian (3.1) with some external potential $\hat{V}$, i.e. densities obeying (3.7), which are called pure-state V-representable (P-VR) densities. The above definition leads to the correspondence $\{\Psi\} \rightarrow \{\rho\}$. To prove the map $\{\Psi\} \leftrightarrow \{\rho\}$ we need to show the inverse $\{\Psi\} \leftarrow \{\rho\}$, i.e. different states imply different densities. Due to the Ritz principle we have for the ground state energy,

$$E_{g.s.} = \langle\Psi|\hat{H}|\Psi\rangle < \langle\Psi'|\hat{H}|\Psi'\rangle \tag{3.37}$$

$$E'_{g.s.} = \langle\Psi'|\hat{H}'|\Psi'\rangle < \langle\Psi|\hat{H}'|\Psi\rangle, \tag{3.38}$$

adding the two inequalities (3.37) and (3.38) we obtain

$$\begin{aligned} E_{g.s.} + E'_{g.s.} &< \langle\Psi'|\hat{H}|\Psi'\rangle + \langle\Psi|\hat{H}'|\Psi\rangle \\ &= \langle\Psi'|\hat{H}' + \hat{H} - \hat{H}'|\Psi'\rangle + \langle\Psi|\hat{H} + \hat{H}' - \hat{H}|\Psi\rangle \\ &= E'_{g.s.} + E_{g.s.} + \int (\rho'(\mathbf{r}) - \rho(\mathbf{r}))(v(\mathbf{r}) - v'(\mathbf{r}))\mathbf{dr} \end{aligned}$$

where we used that $\hat{H}' = \hat{T} + \hat{V}' + \hat{W}$ and $\langle\Psi|\hat{V}|\Psi\rangle = \int \rho(\mathbf{r})v(\mathbf{r})\mathbf{dr}$. It is seen that the assumption $\rho'(r) = \rho(r)$ leads to a contradiction. Hence the map $\{\Psi\} \leftrightarrow \{\rho\}$ is proven. The second HK theorem states that the energy functional

$$E_{v_0}[\rho] = \langle\Psi[\rho]|\hat{T} + \hat{W} + \hat{V}_0|\Psi[\rho]\rangle \tag{3.39}$$

possesses a variational minimum and the minimum is the ground state energy of the system (with a non-degenerate ground state).

$$E_0 = \inf_{\rho\in P-VR} E_{v_0}[\rho] = \inf_{\rho\in P-VR} \Big\{F_{HK}[\rho] + \int v(\mathbf{r})\rho(\mathbf{r})d\mathbf{r}\Big\}, \tag{3.40}$$

where

$$F_{HK}[\rho] = \langle\Psi[\rho]|\hat{T} + \hat{W}|\Psi[\rho]\rangle \tag{3.41}$$

is a universal density functional, in the sence that it does not depend on the system under study (i.e. the external potential $v(\mathbf{r})$). The functional $F_{HK}[\rho]$ is convex which means that if $\lambda_1\rho_1 + \lambda_2\rho_2$ belongs to the domain, then it holds

$$F[\lambda_1\rho_1 + \lambda_2\rho_2] \leq F[\lambda_1\rho_1] + F[\lambda_2\rho_2]; \rho_1 + \rho_2 = 1, \lambda_i \geq 0. \tag{3.42}$$

this implies that infimum is also a minimum.

$$E_0 = \min_{\rho\in P-VR} E_{v_0}[\rho] \tag{3.43}$$

The differentiability of $F_{HK}[\rho]$ (which is established for P-VR densities) allows one to replace (3.43) with the condition that the energy is stationary with respect to changes in the density, subject to the constraint $\int \rho(\mathbf{r})d\mathbf{r} = N$

$$\delta E_{v_0}[\rho] - \mu\delta\left[\int \rho(\mathbf{r})d\mathbf{r} - N\right] = 0, \tag{3.44}$$

hence the Euler-Lagrange equation reads

$$\frac{\delta E_{v_0}[\rho]}{\delta\rho} = \mu \tag{3.45}$$

The differentiability of $F_{HK}[\rho]$ and hence $E_{v_0}[\rho]$ has been established only for the P-VR densities. In cases where ρ is not pure state V-representable, universal functionals on different domains must be considered.

3.3 Kohn Sham equations

The Hohenberg-Kohn formalism discussed in the previous section furnishes the connection between the electron density and the external potential of a system and also specifies the domain of definition of the universal density functional. However, the HK theory does not tell us about the explicit form of the universal functional F_{HK}, therefore the set of HK lemmas represent a mathematical assertion of the role of the electronic density as determining the whole system (at certain conditions), but it can not be directly employed in practice. One calls thus for a technical scheme which may perhaps involve approximations.

Kohn and Sham proposed [87] a method in which the problem of finding the density of an interacting system and consequently the external potential is turned into a problem of finding the density of a non-interacting system (i.e. system with $W = 0$) ρ_s that is equal to the density of the interacting system ρ.

Consider a non-interacting auxiliary system with the Hamiltonian

$$\hat{H}_s = \hat{T}_s + \hat{V}_s, \tag{3.46}$$

the corresponding energy will be given by

$$E_s[\rho] = T_s[\rho] + \int v_s(\mathbf{r})\rho(\mathbf{r})\mathbf{dr}, \tag{3.47}$$

where v_s is an effective potential in the non-interacting system that yields the density $\rho_s = \rho$. The energy of an interacting system is

$$E[\rho] = T[\rho] + \int v(\mathbf{r})\rho(\mathbf{r})\mathbf{dr} + W[\rho], \tag{3.48}$$

where $W[\rho]$ is the electron-electron interaction energy which can be expressed as a sum of the classical term $J[\rho]$ (3.25) and a remaining unknown non-classical interaction. Kohn and Sham suggested to reformulate the energy expression (3.48) in such a way that the kinetic energy T is replaced with its non-interacting counterpart T_s, and the electron-electron interaction W is disguised in an unknown density functional E_{xc} :

$$E[\rho] = T_s[\rho] + \int v(\mathbf{r})\rho(\mathbf{r})\mathbf{dr} + J[\rho] + E_{xc}[\rho], \tag{3.49}$$

where

$$E_{xc}[\rho] = F_{HK}[\rho] - J[\rho] - T_s[\rho] \tag{3.50}$$

is termed exchange-correlation functional which incorporates both the troublesome electron-electron interaction $W[\rho]$ and the kinetic energy of the interacting system $T[\rho]$.

The energy functional (3.49) possesses a variational minimum according to the second HK theorem. Performing a variation of the functional $E_{v_0}[\rho]$, that is the functional $E[\rho]$ with the specific external potential $\hat{V}_0$ that delivers the ground state density $\rho_0(\mathbf{r})$ and the ground state energy E_0, and setting the variation δE_{v_0} to zero, after some manipulation, one can arrive at

$$v_s(\mathbf{r}) = v_0(\mathbf{r}) + \int \frac{\rho_0(\mathbf{r_1})}{\mathbf{r_{12}}} \mathbf{dr_1} + v_{xc}(\mathbf{r}), \tag{3.51}$$

with

$$v_{xc}(\mathbf{r}) = \left. \frac{\delta E_{xc}[\rho]}{\delta \rho(\mathbf{r})} \right|_{\rho_0} \tag{3.52}$$

The energy (3.49) can be rewritten

$$E[\rho] = T_s[\rho] + \int v_s(\mathbf{r}) \rho(\mathbf{r}) \mathbf{dr} \tag{3.53}$$

The Kohn-Sham (KS) method in its original form is applied to systems with non-degenerate ground state. In this case the density can be expressed as

$$\rho(\mathbf{r}) = \sum_i^N |\varphi_i(\mathbf{r})|^2, \tag{3.54}$$

where $\varphi_i(\mathbf{r})$ are the lowest N single-particle orbitals which can be found from the Schrödinger equation

$$\left(-\frac{\nabla^2}{2} + v_s(\mathbf{r}) \right) \varphi_i(\mathbf{r}) = \epsilon_i \varphi_i(\mathbf{r}), \epsilon_1 < \epsilon_2 \leq \epsilon_3 \leq ... \tag{3.55}$$

Densities that can be represented in the form (3.54) are called noninteracting V_s-representable (P-V_sR) densities. Equations 3.51 through 3.55 represent the Kohn-Sham equations. Starting with a guess at $\rho(\mathbf{r})$ one obtains v_s from (3.51) and (3.52), then solving (3.55) for φ_i constructs the new $\rho(\mathbf{r})$ via (3.54). The process is repeated until convergence within a given threshold.

3.4 Time-dependent DFT

Excitation energies in the framework of DFT can be obtained with the use of the linear response approach to the time-dependent DFT (TDDFT) formalism. The TDDFT formalism is based on the Runge-Gross theorem. [88] The theorem is derived

for electrons moving in an external time-dependent electric field $v(\mathbf{r},t)$. The system is described by the time-dependent Schrödinger equation

$$\hat{H}(\mathbf{r},t)|\Psi(\mathbf{r},t)\rangle = i\frac{\partial}{\partial t}|\Psi(\mathbf{r},t)\rangle \tag{3.56}$$

The external potential $v(\mathbf{r},t)$ generates the wavefunction $|\Psi(\mathbf{r},t)\rangle$ and the time-dependent electron density $\rho(\mathbf{r},t)$. The Runge-Gross theorem establishes the existence of a one-one mapping between the external potential modulo a time-dependent constant, the wavefunction up to a phase factor and the density:

$$v(\mathbf{r},t) + C(t) \leftrightarrow e^{-iK(t)}|\Psi(\mathbf{r},t)\rangle \leftrightarrow \rho(\mathbf{r},t) \tag{3.57}$$

In analogy with the KS theory an auxiliary noninteracting system can be introduced with the same density as in the interacting one, which can be represented in terms of one-electron functions as

$$\rho(\mathbf{r},t) = \sum_i |\varphi_i(\mathbf{r},t)|^2, \tag{3.58}$$

The orbitals are defined from the time-dependent KS equation

$$\Big[-\frac{\nabla^2}{2} + v(\mathbf{r},t) + \int \frac{\rho(\mathbf{r}',t)}{\mathbf{r_{12}}}\mathbf{dr}' + v_{xc}(\mathbf{r},t)\Big]\varphi_i(\mathbf{r},t) = i\frac{\partial}{\partial t}\varphi_i(\mathbf{r},t), \tag{3.59}$$

where v_{xc} is an exchange-correlation potential [88] usually approximated by the adiabatic expression [23]

$$v_{xc}(\mathbf{r},t) \approx \frac{\delta E_{xc}}{\delta\rho(\mathbf{r}',t)}. \tag{3.60}$$

The excitation energies are obtained from the TDDFT linear response theory. [23] In this theory the response of polarizability $\alpha(\omega)$ to a time-dependent electric perturbation $\omega(\mathbf{r},t) = E_z(t)$ is the central property. The mean dynamic polarizability is shown [23] to be

$$\bar{\alpha}(\omega) = \sum_I \frac{f_I}{\omega_I^2 - \omega^2}, \tag{3.61}$$

where $\omega_I = E_I - E_0$ is the vertical excitation energy and

$$f_I = \frac{2}{3}\omega_I \sum_{i=x,y,z} |\langle\Psi_0|\hat{x}_i|\Psi_I\rangle|^2$$

is the corresponding oscillator strength. From the poles of (3.61) it is possible to determine the spectrum of excitations ω_I.

Using the adiabatic approximation and a finite basis set, the problem of finding excitation energies within TDDFT can be reduced to the solution of an eigenvalue

problem, which in a two-level approximation (i.e., including only single excitations) is given by,[23]

$$\begin{bmatrix} \mathbf{A} & \mathbf{B} \\ \mathbf{B} & \mathbf{A} \end{bmatrix} \vec{F}_I = \omega_I \begin{bmatrix} \mathbf{1} & \mathbf{0} \\ \mathbf{0} & \mathbf{-1} \end{bmatrix} \vec{F}_I, \tag{3.62}$$

where $\mathbf{A}$ and $\mathbf{B}$ are the Hessians of the electronic energy. The dominant contributions to the $\mathbf{A}$ matrix are the transition energies $\Delta\varepsilon = \varepsilon_{unocc} - \varepsilon_{occ}$ between the unoccupied and occupied Kohn-Sham orbitals (3.55). The matrix $\mathbf{B}$ represents a coupling between different transitions. In many cases an approximation can be made where $\mathbf{B}$ matrix is omitted leading to the Tamm-Dancoff approximation (TDA). [89] In case when a hybrid functional is used with exchange-only part, the TDDFT-TDA method reduces to the CIS method (see section 2.7).

The method in its approximate form can be successfully applied to analyze the spectra of various molecular systems. However, there are several deficiencies, which limit the accuracy of description of certain types of the excited states, for example the states with substantial admixture of double excitations.

Owing to the nature of the approximation of linear response to the Kohn-Sham reference, the excitation energies in situations with strong non-dynamic correlation in the ground state are usually inadequate. The issue is more pronounced due to the self interaction error originating from the use of approximate density functionals. This makes the method less accurate for the description of excitations to ionic states where the electron cloud tends to delocalize, thus reducing the effect of the self-interaction error. For example, TDDFT in its approximate form fails to accurately describe the ${}^1\Sigma_u^+ \leftarrow {}^1\Sigma_g^+$ excitation in H_2 molecule. [90–92]

3.5 Alternative DFT methods for ground and excited states.

3.5.1 Ensemble DFT for the ground state

It was demonstrated by Schipper and co-workers [93] that even if the interacting density is P-VR density, the noninteracting counterpart does not always correspond to a pure state Ψ_s but it may correspond to an ensemble N-particle density matrix Γ (3.11), i.e. the density ρ_s can be represented in certain cases only by an ensemble of single-determinantal densities[1]

$$\rho_s(\mathbf{r}) = Tr\{\hat{\rho}\hat{\Gamma}\} = \sum_{L=1}^{\infty}\sum_{M=1}^{N} w_M \langle\Phi_L^s|\Phi_M^s\rangle\langle\Phi_M^s|\hat{\rho}|\Phi_L^s\rangle = \sum_{L=1}^{N} w_L \rho_L^s(\mathbf{r}) \tag{3.63}$$

[1] The complete set of states can be constructed from the single determinants

Densities (3.63) are referred to as noninteracting ensemble V_s-representable (E-V_sR). Several test cases were considered [93, 94] such as H_2+H_2, C_2 and CH_2. Although the ground states of these molecules are nondegenerate, the molecules exhibit strong static electron correlation due to near degeneracy of several configurations. It was demonstrated that even if the exact exchange-correlation functionals were used, the standard KS scheme would fail in these cases. As a consequence, the KS method in its conventional form cannot be applied to description of bond dissociation, bond formation or photoisomerization and other processes which are typified by strong nondynamic electron correlation.

The KS method can be generalized with the help of ensemble DFT approach for which the mathematical foundation was developed by Lieb. [95] By construction the functional $E[\rho]$ is defined on the set of P-V_sR densities. The functional can be extended, however, to a more general class of densities. Lieb [95] proposed an extended functional F_L, given by

$$F_L[\rho] \equiv \inf_{\substack{\hat{\Gamma}\to\rho \\ \hat{\Gamma}=\sum w_L|\Phi_L\rangle\langle\Phi_L|, \\ \sum w_L=1}} Tr\{\hat{\Gamma}\hat{H}\} \tag{3.64}$$

The functional F_L is defined for arbitrary nonnegative normalizable densities[2] ρ. Consequently, the KS scheme can be extended to ensemble densities (3.63), which can be represented by single-particle states φ_i as [98]

$$\rho_s(\mathbf{r}) = \sum_{i<i^{HOMO}} |\varphi_i(\mathbf{r})|^2 + \sum_{i=i^{HOMO}} n_i|\varphi_i(\mathbf{r})|^2, \tag{3.65}$$

where the fractional occupation numbers n_i are related to the coefficients w_K in (3.63) and the integer occupation numbers θ_{Li} of the orbitals φ in the density ρ_L^s corresponding to a single determinant Φ_L^s, (henceforth referred to as microstates).

$$\rho_L^s(\mathbf{r}) = \langle\Phi_L^s|\hat{\rho}(\mathbf{r})|\Phi_L^s\rangle = \sum_i \theta_{Li}|\varphi_i(\mathbf{r})|^2 \tag{3.66}$$

as

$$n_i = \sum_{L=1}^{N} w_L\theta_{Li} \tag{3.67}$$

3.5.2 Multiplet states in DFT

The early examples of application of the ensemble formalism appear in the work of Slater and coworkers in 1969 [99] where it was attempted to extend the Hartree-Fock

[2] In the Kohn-Sham formalism the functional F_L is reduced to only kinetic part T_L. The differentiability of T_L was proven for all E-V_sR densities[96, 97]

procedure to describe multiplet bands and therefore multiplet states of atoms which are given by several configurations rather than one determinant. It was proposed in an intuitive way to use nonintegral occupation numbers for the atomic orbitals.

The knowledge of multiplet energies allows one to estimate the excitation energies between the respective multiplet states. Excited states within DFT formalism can be estimated using the sum method [100] from which energies and densities of interesting multiplets can be derived as explained below.

A pioneering work on application of DFT to multiplet states and therefore to calculation of excitation energies was done by Ziegler and coworkers. [100] The formalism was developed within the Slater-Hartree-Fock (X_α) method, which is the LDA (LSDA) method with E_c neglected (see section 3.1). The energy (3.29) can be cast as

$$E \approx E[\rho_1] + \epsilon, \tag{3.68}$$

where $E[\rho_1]$ is the energy with the LSD exchange only term, it is also called statistical energy. The statistical energy $E[\rho_1]$ can be represented by a single-determinant density, while ϵ is the part of the energy that can not be reduced to a single determinantal energy.

The residual ϵ is not zero for multiplets with a multideterminantal wave function, i.e. the energy of a multiplet cannot in general be represented by a single determinant. On the other hand the energy of a multiplet E^m can be expressed as a weighted sum of one-determinantal energies $E(\Phi_i)$,

$$E^m = \sum_i A_i E(\Phi_i) \tag{3.69}$$

The idea was to express the energy of a single determinant by a weighted sum of energies of multiplets

$$E(D_i) = \sum_j C_{ij} E_j^m \tag{3.70}$$

which can accordingly be approximated by the statistical energy $E[\rho_1]$ and therefore one can obtain a set of equations

$$E[\rho_1^i] = \sum_j C_{ij} E_j^m \tag{3.71}$$

from which the multiplet of interest E_k^m can be obtained given the number of different determinants with energies $E[\rho_1^i]$ is the same as the number of different multiplets. The procedure was called the sum method. Consider for instance configurations with all but highest two orbitals doubly occupied, whereas the HOMO-1 (a) and HOMO (b) are singly occupied. The following states arise in this case: $|ab|$, $\frac{1}{\sqrt{2}}(|a\bar{b}|+|\bar{a}b|)$, $|\bar{a}\bar{b}|$ and $\frac{1}{\sqrt{2}}(|a\bar{b}|-|\bar{a}b|)$, where the three first states are triplets and the last one is a singlet.

The configurations $|a\bar{b}|$ and $|\bar{a}b|$ are mixed half triplet and half singlet states with the energy

$$E_{|a\bar{b}|} = E_{|\bar{a}b|} = \frac{1}{2}(E_t + E_s), \tag{3.72}$$

From the sum method we have for the singlet:

$$E_s = 2E_{|a\bar{b}|} - E_t. \tag{3.73}$$

The further investigation of multiplet energies and splittings were carried out by Gunnarsson and Lundgvist [101] in the context of LSD approach. The authors proposed to restrict the minimization of the universal density functional to a subspace $M(\Gamma, S)$, where Γ and S are the species of irreducible representations in the given space G and spin Σ groups. The energy is minimized with respect to the spin-density[3] $\underline{\rho}$. Therefore the method allows to minimize the energy for a specified symmetry i.e. to find the energy of a given multiplet. One can hence obtain the excitation energy provided the energies of the ground state and a higher lying multiplet are known. The shortcoming of the proposed technique is that the symmetry constraints imposed upon the densities are to be incorporated also into the exchange-correlation functional for which there is no clear prescription.

In a later work by von Barth [102] it has been proposed to use only the spherically symmetric part of the density for the construction of $E_{xc}[\rho]$. The idea was further developed in works of Görling[103], Theophilou[104], and Daul[105].

The practical implementations of the sum method in DFT include variants of the so-called restricted open-shell Kohn-Sham (ROKS) [106, 107]. One of the ROKS schemes will be briefly discussed in Section3.6.1. While the method allows one to calculate the properties of a state of a given symmetry, its application is only justified when applied to the lowest energy state in the given symmetry.

3.5.3 Ensemble DFT for excited states

The lack of HK theorem for excited states [108, 109] poses principal difficulties in defining an excited state density functional because for a given excited state density $\rho_i(\mathbf{r})$, the corresponding external potential is, in general, not uniquely determined. However, according to the HK theorem, a given ground state density $\rho(\mathbf{r})$ determines the external potential up to a constant, which implies that the full Hamiltonian is known. Therefore, one can determine the excited states provided the ground state is

[3] Spin-density in the sense of the one-particle density matrix that is complete in the spin space $\underline{\rho} \equiv \begin{pmatrix} \rho^{\alpha}(\mathbf{r}) & \frac{1}{\sqrt{2}}\rho^{\gamma}(\mathbf{r}) + \frac{i}{\sqrt{2}}\rho^{\delta}(\mathbf{r}) \\ \frac{1}{\sqrt{2}}\rho^{\gamma}(\mathbf{r}) - \frac{i}{\sqrt{2}}\rho^{\delta}(\mathbf{r}) & \rho^{\beta}(\mathbf{r}) \end{pmatrix}$. The conventional DFT is formulated in terms of the trace of $\underline{\rho}(\mathbf{r})$, that is $\rho(\mathbf{r})$ or with the diagonal parts ρ^{α} and ρ^{β}).

known. This is the key idea in the ensemble-DFT methods, where a weighted sum of energies of the ground and excited states is minimized w.r.t. the corresponding ensemble densities.

The alternative method of calculation of excited states is based on the Rayleigh-Ritz principle for ensembles. The pioneering work in this direction was done by Theophilou [110] who essentially applied the HK formalism to a composite density of ground and excited states [111]. It has been shown that there is a one-to-one correspondence between the ground state density of a composite system $\rho(\mathbf{r}) = \frac{1}{2}(\rho_0(\mathbf{r}) + \rho_1(\mathbf{r}))$ and a local potential $v(\mathbf{r}) = v_0(\mathbf{r}) + v_1(\mathbf{r})$. This allowed one to formulate a variational problem from which one could obtain the excited state density $\rho_1(\mathbf{r}) = 2\rho(\mathbf{r}) - \rho_0(\mathbf{r})$ (ρ_0 can be obtained from conventional HK theory).

The formalism was further developed to include ensembles with unequal weights and to systems with degenerate excited states. [112–114] For simplicity we will discuss an ensemble of the ground $|\Psi_1\rangle$ and the lowest excited $|\Psi_2\rangle$ states. The ensemble Rayleigh-Ritz principle assures that

$$E^w = w_1 E_1 + w_2 E_2 \leq w_1 \langle \Psi_1 | \hat{H} | \Psi_1 \rangle + w_2 \langle \Psi_2 | \hat{H} | \Psi_2 \rangle \tag{3.74}$$

for arbitrary fixed w_i satisfying $0 \leq w_2 \leq w_1 \leq 1$. The density matrix $\hat{\Gamma}$ (3.11) can be written in this case

$$\hat{\Gamma} = w_1 |\Psi_1\rangle\langle\Psi_1| + w_2 |\Psi_2\rangle\langle\Psi_2| \tag{3.75}$$

The ensemble density functional will be given

$$F^w[\rho] = w_1 \langle \Psi_1[\rho] | \hat{H} | \Psi_1[\rho] \rangle + w_2 \langle \Psi_2[\rho] | \hat{H} | \Psi_2[\rho] \rangle, \tag{3.76}$$

and the corresponding density,

$$\rho(\mathbf{r}) = Tr\{\hat{\Gamma}\hat{\rho}\} = w_1\rho_1(\mathbf{r}) + w_2\rho_2(\mathbf{r}), \text{ with } \rho_i = \langle \Psi_i | \hat{\rho}(\mathbf{r}) | \Psi_i \rangle \tag{3.77}$$

The energy

$$E^w_{v0}[\rho] = F^w[\rho] + \int v_0(\mathbf{r})\rho(\mathbf{r})\mathbf{dr} \tag{3.78}$$

is minimized with respect to the density[4] ρ (3.77) at fixed w_i. The excitation energy can be calculated as

$$E_2 = \frac{E^w - w_1 E^w|_{w_2=0}}{w_2} \tag{3.79}$$

[4]The problem is turned, similarly to the KS method, to a noninteracting problem where the actual optimization is carried out for the density composed of fractionally occupied one-electron orbitals as in (3.65)

3.6 Practical implementations of Ensemble-DFT

3.6.1 Restricted Open Shell KS (ROKS)

When applying the ensemble formalism to a specific multiplet state it is convenient to express the density and the ground state energy of a multiplet as a weighted sum of densities (energies) of the individual KS determinants (microstates). In this case one can employ the standard exchange-correlation functionals because they obey the sum rules derived for single determinant densities.

The density of a multiplet state can thus be expressed as a weighted sum of the respective densities of microstates $\rho_L(\mathbf{r})$

$$\rho(\mathbf{r}) = \sum_L w_L \rho_L(\mathbf{r}) \tag{3.80}$$

where the weighting factors w_L are determined by the symmetry of the system and are kept fixed. The density (3.80) is an average of all densities corresponding to the components of the given multiplet state. [102]

According to the vector coupling scheme discussed in section 3.5.2, the energy is expressed as a linear combination of the open-shell single KS determinants Φ_L (microstates) of the Kohn-Sham system

$$E = \sum_L w_L E_L(\Phi_L) \tag{3.81}$$

The one-electron equations can be obtained by optimizing the multiplet energy w.r.t. the density $\rho(\mathbf{r})$ (3.80). In the spin-restricted open shell Kohn-Sham (ROKS) method the optimization of the energy expression is carried out w.r.t. the KS orbitals. The common set of orbitals is used to construct the KS determinants Φ_L. The orbitals are split into two subsets: the closed shell subset of doubly occupied orbitals and the open-shell subset with partially occupied orbitals. The same space parts of the orbitals are used for both α and β spin electrons. This guarantees that the non-interacting KS wavefunction and the density obeys the correct spin and spatial symmetry requirements. [115]

Single-determinantal energies $E(\Phi_L)$ occuring in (3.81) can be expressed similarly to the ROHF energy (2.33) with the difference that the HF exchange energies are replaced with the DFT exchange-correlation energies. The density of an open-shell can be expressed in terms of the KS orbitals as

$$\rho_L^\sigma(\mathbf{r}) = \sum_i |\varphi_i|^2 + \sum_s n_{s,L}^\sigma |\varphi_s|^2, \sigma = \alpha, \beta \tag{3.82}$$

The respective symmetry adapted density $\rho(\mathbf{r})$ (3.80) is then given via the fractionally occupied KS orbitals by

$$\rho(\mathbf{r}) = 2\sum_i |\varphi_i|^2 + 2\sum_s f_s|\varphi_s|^2. \tag{3.83}$$

The occupation numbers in (3.83) are fixed, and the minimization of the energy (3.81) is performed w.r.t. the orbitals φ_i and φ_s subject to the constraint of orthonormality

$$\langle\varphi_i|\varphi_j\rangle = \delta_{ij}, \tag{3.84}$$

so that one can write $E = E[\varphi]$. The ROKS equations are derived in a way similar to the ROHF equations. [115, 116] The constraints are incorporated via the Lagrangian multipliers ε_{ij} and the functional

$$E' = E - \sum_{i,j}\varepsilon_{ij}(\langle\varphi_i|\varphi_j\rangle - \delta_{ij}) \tag{3.85}$$

is required to be stationary,

$$\delta E' = \sum_i \Big[\langle\delta\varphi_i|\hat{F}_i|\varphi_j\rangle + \langle\varphi_j|\hat{F}_i|\delta\varphi_i\rangle\Big] - \sum_{ij}\varepsilon_{ij}\Big[\langle\delta\varphi_i|\varphi_j\rangle + \langle\varphi_i|\delta\varphi_j\rangle\Big] = 0, \tag{3.86}$$

where $\hat{F}$ is a Fock-like operator. The variations $\langle\delta\varphi_i|$ and $|\delta\varphi_i\rangle$ are arbitrary, therefore, one obtains two sets of equations

$$\hat{F}_i|\varphi_i\rangle = \sum_j \varepsilon_{ji}|\varphi_j\rangle, \tag{3.87}$$

$$\langle\varphi_i|\hat{F}_i = \sum_j \varepsilon_{ij}\langle\varphi_j| \tag{3.88}$$

subtracting the complex conjugate of (3.87) from (3.88) yields that the Lagrangian multipliers are the elements a Hermitian matrix

$$\varepsilon_{ji} = \varepsilon_{ij}^* \tag{3.89}$$

From the orthonormality condition (3.84), the equations (3.87) and (3.89) can be rewritten as

$$\hat{F}_i|\varphi_i\rangle = \sum_j |\varphi_j\rangle\langle\varphi_j|\hat{F}_i|\varphi_i\rangle \tag{3.90}$$

$$\langle\varphi_i|\hat{F}_i - \hat{F}_j|\varphi_i\rangle = 0 \tag{3.91}$$

In a close-shell case only the first equation needs to be taken care of, as the second is automatically fulfilled by the generalized Brillouin theorem. [117] Therefore, only

one Fock operator $\hat{F}$ is needed, which allows one to recast the problem as a single pseudoeigenvalue equation. However, in an open-shell case, both variational conditions must be explicitly satisfied. The two equations can be solved together with the help of Lagrangian multipliers λ_{ij} by adding the condition (3.89) to the equation (3.87)

$$\hat{F}_i|\varphi_i\rangle = \sum_j \left[(1-\lambda_{ji})\varepsilon_{ji} + \lambda_{ji}\varepsilon^*_{ij}\right]|\varphi_j\rangle \tag{3.92}$$

The matrix of multipliers λ should be antisymmetric, [116] but otherwise arbitrary. The equations can be formulated as a single pseudoeigenvalue problem by the use of Roothaan's coupling operators technique. The derivation of the ROKS equations can be found in reference. [107] After the described modifications the final ROKS equations can be written as

$$\hat{F}_i|\varphi_i\rangle = \epsilon_i|\varphi_i\rangle, \tag{3.93}$$

where the effective Hamiltonian $\hat{F}$ can be divided by projection operators [107] into closed cc, open oo, virtual uu and mixed $co, cv, ov, ...$ subblocks in the form

$$\begin{pmatrix} \hat{F}_{cc} & \hat{F}_{co} & \hat{F}_{co} & \hat{F}_{cu} \\ \hat{F}_{oc} & \hat{F}_{oo} & \hat{F}_{oo} & \hat{F}_{ou} \\ \hat{F}_{oc} & \hat{F}_{oo} & \hat{F}_{oo} & \hat{F}_{ou} \\ \hat{F}_{uc} & \hat{F}_{uo} & \hat{F}_{uo} & \hat{F}_{uu}, \end{pmatrix} \tag{3.94}$$

The method has been successefully aplied to multiplet states of molecules [118] where the given multiplet represents the ground state of the molecule and the orbital degeneracy is symmetry related.

Attempts to extend the use of ROKS for handling excited states have been reported by Frank et al. [72] where the energy of the excited state was optimized with respect to the excited state density. The direct optimization of the energy (3.81) with respect to the excited state density (3.80) is however not formally justified [108, 109] as pointed out in the section 3.5.2, and can lead to certain artefacts as has been found out by Buda et al. [119, 120]

3.6.2 Restricted Ensemble-Referenced KS (REKS)

In the ROKS method discussed in the previous section the energy and density are expressed as weighted sums of the respective energies and densities of microstates with weighting factors w_L fixed. The method can be extended to also treat situations where strong static correlation results from near-degeneracy, such as in, e.g. biradicaloids. The approach called restricted ensemble-referenced Kohn-Sham (REKS) method [118, 121–123] introduces a variational freedom to the expansion coefficients

w_i and hence to the fractional occupation numbers n_i (3.67). The derivation proceeds as follows, first, a highly symmetric system with orbitally degenerate states Ψ_1 and Ψ_2 is considered (e.g. D_{2d} ethylene). The diabatic states Ψ are built from the configurations $\varphi_{r\bar{r}}$ and $\varphi_{s\bar{s}}$, where indices r and s correspond to the HOMO and the LUMO from the conventional single-determinantal KS calculation. In this case the densities and diabatic energies E_{d_1} and E_{d_2} can be obtained within the ROKS approach. Next, apply a weak perturbation (e.g. a twist by a small angle from 90° in ethylene) thereby lifting the degeneracy between the configurations $\varphi_{r\bar{r}}$ and $\varphi_{s\bar{s}}$. This will induce an interaction $d = \langle\Psi_1|\hat{H}|\Psi_2\rangle$ between the reference states, leading to a secular problem, whence the adiabatic energy of the ground state is obtained

$$E = \frac{1}{2}(E_{d_1} + E_{d_2}) - \frac{1}{2}\sqrt{(E_{d_1} - E_{d_2})^2 + d^2} \tag{3.95}$$

After some manipulations the energy can be expressed as a weighted sum of the energies of the reference microstates $E_{r\bar{r}}$, $E_{s\bar{s}}$ and single excitations thereof

$$E = \frac{n_r}{2}E_{r\bar{r}} + \frac{n_s}{2}E_{s\bar{s}} + (n_r n_s)^{3/4}(E_{rs} - \frac{1}{2}E_{r\bar{s}} - \frac{1}{2}E_{s\bar{r}}), \tag{3.96}$$

where n_r and n_s are the fractional occupation numbers of the orbitals φ_r and φ_s which are obtained variationally together with the orbitals. To be able to cover the "normal" case ($n_r = 2$, $n_s = 0$), i.e., when the static correlation is insignificant (e.g. D_{2h} ethylene), the energy expression is modified. The modification addresses the dependence of the last term in (3.96) on the occupation numbers n_r, n_s, which should become (nearly) linear in the case of the "normal" state. In this way, the REKS energy for a state with $n_r = 2$ and $n_s = 0$ is the same as the energy from the conventional single reference KS method. [118, 124]

The density can be expressed as a weighted sum of the densities of microstates in accordance with the ensemble-DFT formalism. [95] In this particular case, however, the densities corresponding to the microstates $rs, r\bar{s}$ and $s\bar{r}$ compensate each other leaving only the densities of the microstates $r\bar{r}$ and $s\bar{s}$ which can be represented in terms of the KS orbitals as

$$\rho(\mathbf{r}) = \sum_{j}^{core} 2|\varphi_j(\mathbf{r})|^2 + n_r|\varphi_r(\mathbf{r})|^2 + n_s|\varphi_s(\mathbf{r})|^2 \tag{3.97}$$

The fractional occupation numbers of the orbitals φ_r, φ_s are analogous to the natural orbital occupation numbers (3.15) in CASSCF(2,2).

The REKS method has been tested in the calculation of a large number of strongly correlated molecular systems: molecules with dissociating bonds, biradicals [118, 122, 125], magnetic coupling in organic, organometallic and inorganic complexes [124, 126, 127]

These calculations have shown that the method is capable of describing these difficult cases with high accuracy.

Chapter 4

State-Averaged REKS (SA-REKS) method

The ROKS and REKS methods discussed in sections 3.6.1 and 3.6.2 are strictly applicable to the ground states (or to the lowest energy states in the given symmetry class) of molecules where mapping between the density and the potential is justified by the Hohenberg-Kohn theorems. [128] A direct optimization of the excited state energy with respect to the excited state density within the framework of DFT is however questionable [108] and may lead to certain artifacts in practical calculations. [119, 120] In developing a time-independent density functional theory for excited states one has to include the ground state density into consideration. [129–132]

In the present thesis, we suggest a time-independent method to the calculation of excited states in DFT which is based on the ensemble approach. Within the ensemble approach to DFT, [95, 133] the variational principle can be applied strictly to the optimization of energies of equiensembles of N lowest states of the interacting Hamiltonian as well as to ensembles of fractionally occupied and unequally weighted states. [113, 114, 134, 135] Thus the aforementioned difficulties with the direct optimization of the excited state energy w.r.t. its own density are avoided. For obtaining the excited state energy, we suggest to optimize variationally a weighted sum of the energies of the ground state described by the REKS method to account for the strong static correlation in the ground state and of the excited state described by the ROKS method. The KS orbitals obtained in this variational procedure are used to calculate the ground and the excited state energies with the REKS and ROKS methods, respectively. Because the outlined computational approach bears a similarity with the state-averaged (SA) method in multi-reference wave function *ab initio* theory, the new approach is dubbed SA-REKS.

In practical implementation of the SA-REKS method, the ground singlet state energy is combined with the energy of the lowest excited singlet state which can be obtained by a single electronic excitation from the ground state. Thus, this method can be used for theoretical modeling of photoexcitation processes [136–138] in systems where the standard DFT/TDDFT methods may be not applicable because of the presence of near degeneracy effects in the ground state. [91, 139–142] In the following section, the SA-REKS formalism will be described and it will be applied to the calculation of the ground and excited state energies in a number of

model systems in Section 4.2. The excitation energies and the profiles of the excited state potential energy surface obtained in the SA-REKS calculations will be compared with the experimental data, with the results of TDDFT calculations and with the results of multi-reference wave function *ab initio* calculations carried out at the CASSCF/CASPT2 level. [143, 144]

4.1 Method of calculation

Let us consider first an illustrative example of a system in the singlet state with two near-degenerate electronic configurations, $(\ldots \varphi_r^2\ \varphi_s^0)$ and $(\ldots \varphi_r^0\ \varphi_s^2)$. [136–138, 145] Restricting the description to the active orbitals φ_r and φ_s only, the configurations shown in Fig. 4.1 can be constructed within wave function theory. Solutions of the Schrödinger equation in the space of these configurations will generally be given by superpositions of all four configurations.

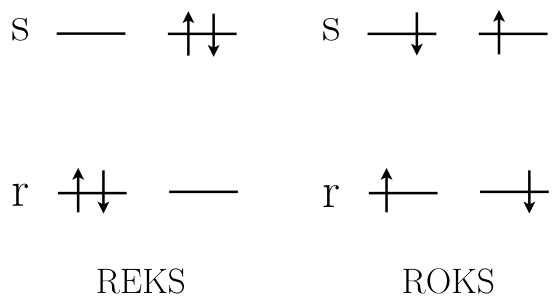

Figure 4.1: *HOMO (r) and LUMO (s) orbitals in the ROKS and the REKS approaches.*

However, if the orbitals φ_r and φ_s are optimized by a suitable unitary transformation which mixes φ_r and φ_s leaving them orthonormal, then the exact solutions for the two-electron two-orbital model system can be represented as in Eq. (4.1), [138]

$$\begin{aligned}
\Theta_{S_0} &= \lambda\,|\varphi_r\bar{\varphi}_r\rangle - \sqrt{1-\lambda^2}\,|\varphi_s\bar{\varphi}_s\rangle \\
\Theta_{S_1} &= \frac{1}{\sqrt{2}}\left(|\varphi_r\bar{\varphi}_s\rangle + |\varphi_s\bar{\varphi}_r\rangle\right) \\
\Theta_{S_2} &= \sqrt{1-\lambda^2}\,|\varphi_r\bar{\varphi}_r\rangle + \lambda\,|\varphi_s\bar{\varphi}_s\rangle \\
\Theta_{T_0} &= \frac{1}{\sqrt{2}}\left(|\varphi_r\bar{\varphi}_s\rangle - |\varphi_s\bar{\varphi}_r\rangle\right)
\end{aligned} \tag{4.1}$$

where the Slater determinants $|\varphi_r\bar{\varphi}_s\rangle$ are properly normalized and it is assumed that the determinant $|\varphi_r\bar{\varphi}_r\rangle$ possesses the lowest expectation value of the Hamiltonian. Note that, as a consequence of the orbital optimization, there will be no mixing between the Θ_{S_0} and Θ_{S_1} functions. Thus, within the two-electron – two-orbital model, the ground state wave function is given by Θ_{S_0}. The Θ_{S_1} wave function represents the state created by a single excitation from the ground state. It is these two states, Θ_{S_0} and Θ_{S_1}, that are targeted in the suggested density functional scheme. Within the density functional formalism, the S_0 state can be described with the use of REKS, and S_1 state - ROKS.

Although the REKS method discussed in the section 3.6.2 is formulated for the ground state only, the energy of the open-shell singlet excited state S_1 in Eq. (4.1) can be calculated non-variationally using the REKS optimized orbitals. For this purpose, the ROKS method [100, 102, 106, 107, 146, 147] can be employed, in which the energy of the S_1 state is given by Eq. (4.2).

$$E^{ROKS-S_1} = E^{KS}_{r\bar{s}} + E^{KS}_{\bar{r}s} - E^{KS}_{rs}, \tag{4.2}$$

where $E^{KS}_{r\bar{s}}, E^{KS}_{\bar{r}s}$ and E^{KS}_{rs} are the Kohn-Sham energies of the individual configurations $(\ldots\varphi^1_r\bar{\varphi}^1_s), (\ldots\bar{\varphi}^1_r\varphi^1_s)$ and $(\ldots\varphi^1_r\varphi^1_s)$, respectively.

Such a non-variational calculation yields an upper limit to the energy of the excited S_1 state. Similar to wave function theory, where the excited state energy can be variationally optimized under the constraint of orthogonality w.r.t. the lower lying states, an improved estimate of the $S_1 \leftarrow S_0$ excitation energy can be obtained with the use of the ensemble formalism by optimizing a weighted sum (ensemble) of the ground S_0 state and the singly-excited S_1 state as in Eq. (4.3),

$$E^{SA-REKS} = C_1\, E^{REKS-S_0} + C_2\, E^{ROKS-S_1} \tag{4.3}$$

where the (positive definite) coefficients C_1 and C_2 sum up to unity. As has been pointed out in the Introduction and in section 3.5, the variational principle is valid for such an ensemble within the context of DFT. [113, 114, 134, 135] The energy (4.3) is optimized with repsect to both the Kohn-Sham orbitals and the fractional occupation numbers in the REKS energy expression. The Kohn-Sham orbitals obtained from this variational procedure can be used to calculate the energies of the S_0 (Eq. (3.96)) and S_1 (Eq. (4.2)) states. Note that, when calculating the S_0 energy according to Eq. (3.96), the fractional occupation numbers of the active orbitals are optimized, however the orbitals are kept frozen. Because the outlined procedure bears a similarity with the state-averaged (SA) approach in conventional wave function theory, it is suggested to dub the new procedure as SA-REKS.

The described computational procedure has been implemented in the COLOGNE08 code, [148] with the help of which the ground state REKS calcula-

tions and the SA-REKS calculations have been carried out. In all density functional calculations, the 6-311G+(3df,2p) basis set [149] was employed unless noted otherwise. DFT calculations we carried out with the use of B3LYP [150] and BH&HLYP [86, 151]. The CASSCF/CASPT2 [143, 144] calculations have been carried out with the help of the MOLCAS 7 code. [152] In the following section, the results of the SA-REKS calculations will be presented and compared with the excitation energies obtained in TDDFT calculations and in the CASSCF/CASPT2 calculations.

4.2 Results

The formalism described in the preceding section has been tested in the calculations of the lowest excited singlet states for a number of model systems. The benchmark set comprises the following molecules: hydrogen molecule H_2, ethylene C_2H_4, and hexa-1,3,5-triene C_6H_8, which is often used in modeling photoisomerization of large unsaturated molecules [70, 71, 153]. The results of the SA-REKS calculations are compared with the excitation energies calculated with the use of time-dependent density functional theory, with high level multi-reference *ab initio* methods and with the available experimental data.

4.2.1 Excitation energy in H_2 along the bond stretching mode

Hydrogen molecule at stretched interatomic distance is often employed as a prototypal system to study the effect of non-dynamic electron correlation. [90, 140, 154] Failure of single-reference spin-restricted wave function *ab initio* and density functional methods to describe the potential energy curve of dissociating H_2 is well documented. [140, 154] Beyond the Coulson-Fischer point (*ca.* 2.75 bohr for R_{H-H} [155]) the single-reference description breaks down and the dissociation curve produced by single-reference spin-restricted methods goes to a higher energy than the energy of two noninteracting atoms.

The excitation energy to the lowest $^1\Sigma_u^+$ state of hydrogen molecule as a function of internuclear distance has been previously calculated with the use of TDDFT [90]. In the present work, the REKS method is applied to this system besides the TDDFT approach, which is used for comparison. The potential energy curves for the ground $^1\Sigma_g^+$ and excited $^1\Sigma_u^+$ states of H_2 are shown in Figure 4.2 and the $^1\Sigma_u^+ \leftarrow {}^1\Sigma_g^+$ excitation energy is shown in Figure 4.3 as a function of distance. At short internuclear distances (less than 2 bohr), the excited state curves obtained in TD-B3LYP and in TD-BH&HLYP calculations match reasonably well the shape of the exact curve obtained from the calculations of Kołos and Wolniewicz [156, 157], which are used as a reference in this work. However, beyond the Coulson-Fischer point, the curves

obtained with TDDFT begin to deviate rapidly from the exact behavior and at large separations a negative excitation energy is obtained, which indicates the breakdown of the spin-restricted single-reference description of the reference ground state [90].

The wrong behavior of the excitation energy from TDDFT on H–H distance is clearly visible in Figure 4.3. The exact excitation energy has a minimum at R_{H-H} = 4.1 bohr. The TD-B3LYP and TD-BH&HLYP excitation curves do not show any minimum and go monotonously down as the internuclear distance increases. It is the behavior of the TDDFT method that has been previously documented in Ref. [90].

The ground $^1\Sigma_g^+$ and excited $^1\Sigma_u^+$ states potential energy curves obtained with REKS and state-averaged REKS methods using the B3LYP and BH&HLYP density functionals are shown in Figure 4.2. REKS calculations with both density functionals reproduce nicely the exact potential energy curve for the ground state. B3LYP functional shows slightly better performance which can be attributed to the fact that this functional was empirically optimized to accurately reproduce thermochemical parameters of molecules in ground states. The ground state energies obtained in the SA-REKS calculations are within 1 kcal/mol from the values obtained in the state-specific REKS calculations.

For the $^1\Sigma_u^+ \leftarrow {}^1\Sigma_g^+$ excitation energy, the difference between the state-averaged and state-specific REKS calculations is more pronounced. Although, at large interatomic distances, both methods (state-averaged and state-specific) agree reasonably well, there is a marked difference at short H–H separations. Near the equilibrium bond length, the state-specific REKS method converges to the usual closed-shell single-reference solution with the bonding $1\sigma_g$ Kohn-Sham orbital doubly occupied and the anti-bonding $1\sigma_u$ orbital empty. Because the ground-state energy in such a case does not depend on the shape of the anti-bonding orbital, this orbital does not attain a shape suitable for good description of the $^1\Sigma_u^+$ excited state, where both orbitals, $1\sigma_g$ and $1\sigma_u$, are singly occupied. In the state-averaged calculation, both orbitals are optimized in such a way so as to minimize the weighted average of the ground and excited state energies (4.3) with $S_0 = {}^1\Sigma_g^+$ and $S_1 = {}^1\Sigma_u^+$.

The state-averaged optimization of REKS orbitals results in a much better agreement of the excited $^1\Sigma_u^+$ state energy with the exact energy as evidenced by Figures 4.2 and 4.3. The discrepancy between the REKS excitation energy and the exact energy at short H–H distances is considerably improved. The excitation energy curve shows a shallow minimum at 5.1 bohr from SA-REB3LYP calculation and at 4.3 bohr from SA-REBH&HLYP calculation which is to be compared with the exact minimum at 4.1 bohr (see Figure 4.3). The magnitude of the $^1\Sigma_u^+ \leftarrow {}^1\Sigma_g^+$ excitation energy is somewhat underestimated at the large H–H distances. This can be interpreted as originating from overstabilization of ionic states with respect to covalent states by approximate density functionals. Note that the $^1\Sigma_u^+$ excited state of H_2 has an ionic

Table 4.1: *Total energies of the ground $^1\Sigma_g^+$ and excited $^1\Sigma_u^+$ states of H_2 and the corresponding excitation energies as obtained with different density functional methods. The distances are in Bohr and energies in Hartree.*

Functional	State	R_{H-H}	TD-DFT	REKS	SA-REKS[a]	Exact[b]
1[c]	$^1\Sigma_g^+$	1	-1.1291	-1.1323	-1.1219	-1.1245
		3	-1.0532	-1.0583	-1.0522	-1.0573
		7	-0.9197	-1.0047	-0.9994	-1.0002
	$^1\Sigma_u^+$	1	-0.6497	-0.1506	-0.5927	-0.5813
		3	-0.7891	-0.7999	-0.8329	-0.7525
		7	-0.8461	-0.8050	-0.8210	-0.6772
	Δ	1	0.4794	0.9817	0.5292	0.5432
		3	0.2640	0.2584	0.2193	0.3048
		7	0.0736	0.1997	0.1784	0.3230
2[d]	$^1\Sigma_g^+$	1	-1.1206	-1.1206	-1.1132	-1.1245
		3	-1.0342	-1.0462	-1.0336	-1.0573
		7	-0.8775	-0.9974	-0.9858	-1.0002
	$^1\Sigma_u^+$	1	-0.6099	-0.0973	-0.5812	-0.5813
		3	-0.7716	-0.7452	-0.7950	-0.7525
		7	-0.8041	-0.7116	-0.7464	-0.6772
	Δ	1	0.5107	1.0234	0.5320	0.5432
		3	0.2626	0.3010	0.2386	0.3048
		7	0.0734	0.2857	0.2393	0.3230

[a] Equal weighting factors are used in the state-averaged calculations.
[b] From Ref. [156, 157]
[c] B3LYP
[d] BH&HLYP

character, whereas the $^1\Sigma_g^+$ ground state possesses a covalent character. The overstabilization of ionic states can be traced back to the effect of electron self-interaction error in approximate density functionals, [122, 158, 159] which leads to somewhat too diffuse occupied KS orbitals. As more self-interaction error free Hartree-Fock exchange energy is mixed into a hybrid HF/DFT functional, such as BH&HLYP, the overall effect of such an overstabilization subsides and the the excitation energy to the ionic $^1\Sigma_u^+$ state obtained in REKS calculations improves (see Figure 4.3).

The state-averaged REKS calculations reported in Figures 4.2 and 4.3 are carried out with the use of equal weighting factors in Eq. (4.3). With a different choice of the weighting factors C_1 and $C_2 = 1-C_1$, a slightly different value of the excitation energy

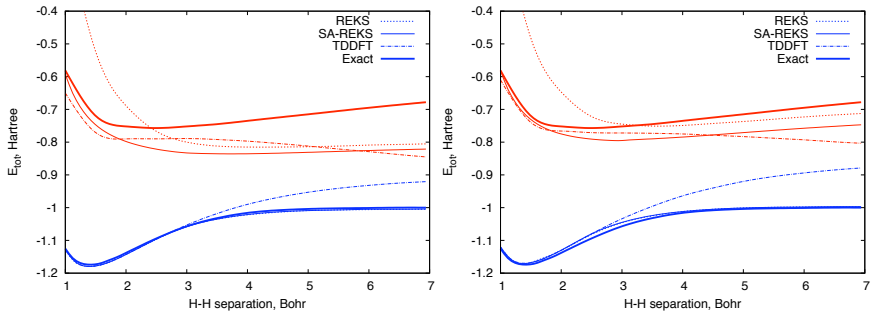

Figure 4.2: *Total energies of H_2 at varying internuclear distance in $^1\Sigma_g^+-$ (blue curves) and $^1\Sigma_u^+-$ (red curves) states. The calculations were performed with B3LYP (left plot) and BH&HLYP (right plot) functionals. The exact curves are from Refs. [156, 157].*

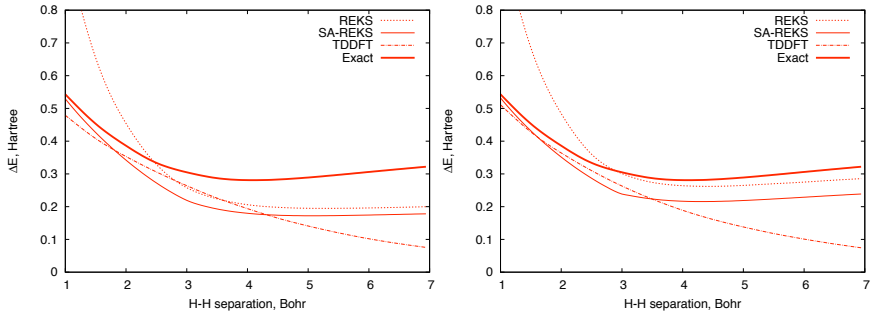

Figure 4.3: *Energies of excitation from $^1\Sigma_g^+-$ to $^1\Sigma_u^+-$ state at varying internuclear distance. The calculations were performed with B3LYP (left plot) and BH&HLYP (right plot) functionals. The exact curve is from Ref. [157].*

can be obtained. Figure 3 shows the dependence of the $^1\Sigma_u^+ \leftarrow {}^1\Sigma_g^+$ excitation energy obtained in state-averaged REKS calculations on the choice of weighting factors. Obviously, with the $C_1 = 1$ the results of a state-specific calculation are reproduced. However, with C_1 varying between 0.1 and 0.9 the excitation energy curves bundle within a narrow range around the curve corresponding to $C_1 = 0.5$. Such that the choice of equal weighting factors in Eq. (4.3) corresponds to a median value of the excitation energy which can be obtained in state-averaged calculation with varying weighting factors. This choice of the weighting factors, $C_1 = C_2 = 0.5$, in state-averaged REKS calculations is adopted throughout this work.

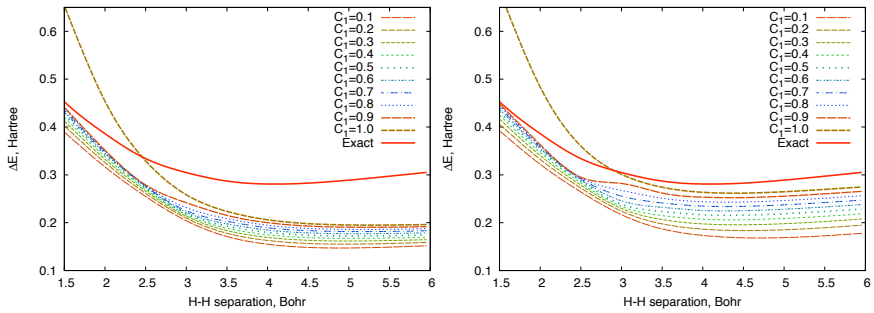

Figure 4.4: *Excitation energies calculated with SA-REKS with varying weighting factors C_1 and C_2 (see Eq.(4.3)). The exact curve is from Ref. [157].*

4.2.2 Ethylene

Twisting about the double bond in ethylene represents another widely used example where strong non-dynamic correlation occurs in the ground state of the molecule. [136–138] In the ground ^1A_g state, ethylene attains a planar conformation (D_{2h} point group) with two carbon atoms bound by a double bond. Along the twisting mode, as the twisting angle approaches 90° the energy gap between the π and π^* orbitals of the double bond decreases and the non-dynamic correlation due to near degeneracy of the $(\ldots(\pi)^2)$ and $(\ldots(\pi^*)^2)$ configurations sets in. At 90° of twist, the two configurations are strictly degenerate due to symmetry in the D_{2d} point group and both orbitals, π and π^*, are singly occupied. [136–138]

The π-bond breaking along the twisting mode in ethylene can not be described within a single-reference approach, such as the usual spin-restricted Kohn-Sham approach. This failure is well documented in the literature [79, 118] and is illustrated in Figure 4.5, where the results of the spin-restricted KS and TDDFT calculations are shown with dashed-dotted lines. In Figure 4.5, it is clearly seen that, in the single reference description, the ground state energy even after 90° of twist corresponds to a doubly occupied π orbital and does not smoothly switch to the $(\ldots(\pi^*)^2)$ configuration.

The $^1B_{1u}$ excited state of the planar C_2H_4 is well described within the TDDFT approach with the use of both density functionals, B3LYP and BH&HLYP. The excitation energy is somewhat underestimated with the use of the B3LYP functional whereas the TD-BH&HLYP energy is in a fairly good agreement with the experiment. The TD-BH&HLYP excitation energy is in markedly better agreement with the experiment than the (6,4)CASPT2 energy which is overestimated by *ca.* 0.3 eV. In all the calculations, TDDFT and CASSCF/CASPT2, the geometry optimized with the

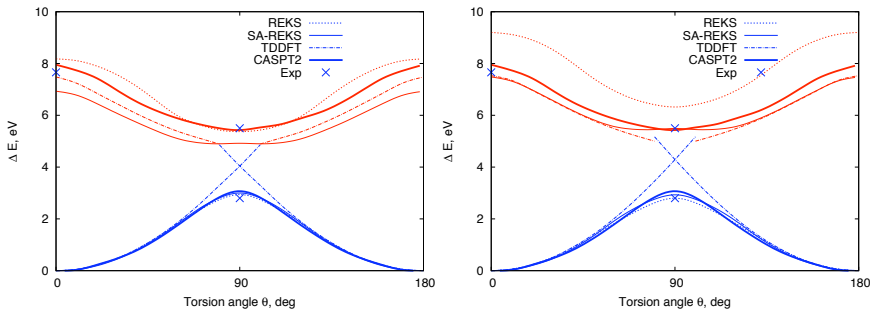

Figure 4.5: *The potential energy profiles of ethylene along torsional angle θ around $C = C$ double bond. The blue curves correspond to 1^1A_1- state and the red ones to 1^1B_1- state. The TDDFT, REKS and SA-REKS calculations were performed with B3LYP (left) and BH&HLYP (right) exchange-correlation functionals. The DFT ground state energy was obtained by optimization forth $\theta = 0 \div 100$ and back $\theta = 180 \div 80$. The experimental vertical excitation energy is from Ref. [160], the adiabatic excitation energy (at 90^0) is from Ref. [161]. The rotation barrier height is from Ref. [162].*

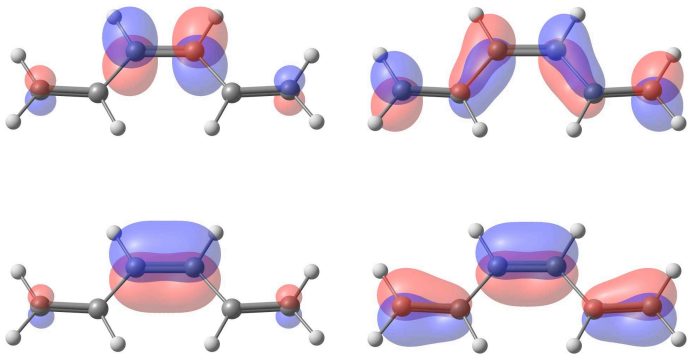

Figure 4.6: *HOMO and LUMO orbitals of 1,3,5-cis-hexatriene obtained by REKS (left) and SA-REKS (right) methods.*

REB3LYP/6-311G+(3df,2p) method along the minimal energy path on the ground state potential energy surface was employed. For the planar ethylene, this geometry is identical to the geometry obtained with the usual single reference B3LYP method.

With the use of the RE-B3LYP/6-311G+(3df,2p) molecular geometry, the exci-

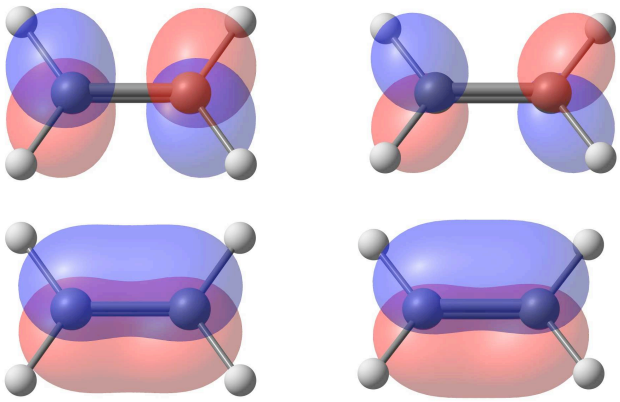

Figure 4.7: *HOMO and LUMO orbitals of ethylene obtained by REKS (left) and SA-REKS (right) methods.*

tation energy to the lowest $^1B_1$ (D_2 point group) state was calculated within the TDDFT approach. At small twisting angles, the TDDFT excited state PES follows more or less accurately the profile of the CASPT2 PES. However, beyond *ca.* 70° of twist, the TDDFT excited state surface crosses the ground state energy surface which leads to the breakdown of the TDDFT calculations thus rendering impossible to describe the excited state PES with TDDFT in this region.

The excited state PES along the twisting mode in ethylene is nicely described within the REKS approach as shows comparison with the (6,4)CASPT2 energies and with the available experimental data [160–162], see Figure 4.5 and Table 4.2. With the use of the REKS orbitals optimized for the ground state, the excitation energy in the planar conformation is overestimated in both sets of calculations, REB3LYP and REBH&HLYP. Similar to the case of H_2 at the equilibrium bond length, this is a consequence of the fact that the π^* orbital is empty in the planar ground state electronic configurations and is not optimized during the state-specific REKS calculation.

Optimizing the REKS orbitals with respect to the average energy, $0.5E(^1A_g) + 0.5E(^1B_{1u})$, of the ground and excited states leads to a noticeable lowering (*ca.* 1 eV) of the excitation energy as obtained with the SA-REKS method. The excitation energy obtained with the SA-REBH&HLYP method is in a very good agreement with the experimental value. Interestingly, the excited state PESs obtained with the SA-REBH&HLYP and TD-BH&HLYP methods are nearly indistinguishable at twisting angles below *ca.* 50°. The shape of the excited state PES obtained in the SA-REB3LYP and SA-REBH&HLYP calculations follows the profile of the (6,4)CASPT2

Table 4.2: *The $S_1 \leftarrow S_0$ excitation energies in ethylene and the barrier to rotation α in the ground S_0 state as obtained with different methods.*

Functional	α	State	REKS	SA-REKS[a]	TD-DFT	CASPT2	Exp
1[b]	0	S_0	-	-	-	-	-
		S_1	8.18	6.93	7.17	7.95	7.66[c]
	90	S_0	2.94	3.00	4.06	3.06	2.8[d]
		S_1	5.36	4.92	-	5.48	5.5[e]
2[f]	0	S_0	-	-	-	-	-
		S_1	9.20	7.48	7.53	7.95	7.66[c]
	90	S_0	2.80	2.93	3.46	3.06	2.8[d]
		S_1	6.32	5.49	-	5.48	5.5[e]

[a)] Equal weighting factors are used in the state-averaged calculations.
[b)] B3LYP.
[c)] From Ref. [160].
[d)] From Ref. [162].
[e)] From Ref. [161].
[f)] BH&HLYP.

PES fairly well (see Figure 4.5). The excited state PES obtained with SA-REB3LYP is shifted downwards by *ca.* 0.5–1 eV with respect to the (6,4)CASPT2 PES. This is yet another manifestation of the effect of self-interaction error in density functional calculations. Mixing in more Hartree-Fock exchange leads to narrowing of the gap between SA-REKS and CASPT2 PESs and the SA-REBH&HLYP excited state PES is in a much better agreement with the (6,4)CASPT2 curve. It is noteworthy that there is a very nice agreement between the SA-REBH&HLYP excitation energies and the experimental data at both planar and 90°-twisted conformations of ethylene (see Table 4.2).

4.2.3 Hexa-1,3,5-triene

Hexa-1,3,5-triene is often used as a prototype system in studying photoisomerization processes in large unsaturated molecules, such as synthetic molecular motors and biologic photosensitive molecules [70, 71, 163]. In hexa-1,3,5-triene, the frontier orbitals, the highest occupied molecular orbital (HOMO) and the lowest unoccupied molecular

orbital (LUMO), correspond to the bonding and the anti-bonding π orbitals of the central double bond, see Fig. 4.8.

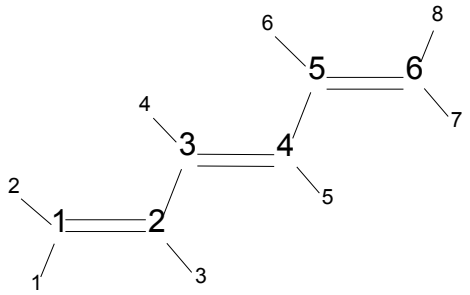

Figure 4.8: *Numbering of atoms in trans-1,3,5-hexatriene.*

In the photoexcitation of hexa-1,3,5-triene, a HOMO–LUMO electronic transition takes place, which leads to breaking of the central C_3–C_4 double bond. As a result, the two allyl fragments, C_1–C_2–C_3 and C_4–C_5–C_6, can rotate freely about the C_3–C_4 bond which leads to isomerization of the *trans*- and *cis*-conformations. Similarly to the case of ethylene twisting and hydrogen dissociation, the correct description of the ground and excited state potential energy surfaces of hexa-1,3,5-triene requires the inclusion of non-dynamic electron correlation, because near the 90° of twist about the C_3–C_4 bond, the configurations corresponding to the doubly occupied HOMO and the doubly occupied LUMO become nearly degenerate.

The single-reference spin-restricted DFT approach fails to describe the PES of the ground state of hexa-1,3,5-triene along the C_3–C_4 twisting mode. Similar to the case of ethylene, there is a cusp on the DFT PES near 90° of twist. The geometry along the minimal energy path along the C_3–C_4 twisting mode was obtained in the REB3LYP/6-311G+(3df,2p) geometry optimization. The REKS ground state potential energy surface is smooth and compares fairly well with the ground state PES obtained in the (6,6)CASPT2 calculation (see Figure 4.9).

The geometry of *trans*-hexa-1,3,5-triene is compared in Table 4.3 with the available experimental data [165, 166] and the results of the wave function *ab initio* calculations carried out at the second order Møller-Plesset (MP2) many-body perturbation theory level. [167] The ground state molecular geometry of *trans*-hexa-1,3,5-triene obtained with REB3LYP/6-311G+(3df,2p) method is in a very good agreement with the MP2 geometry.

The excitation energy of the planar *trans*-hexa-1,3,5-triene calculated with TDDFT is in a fairly good agreement with the experimental datum [164] (see Table

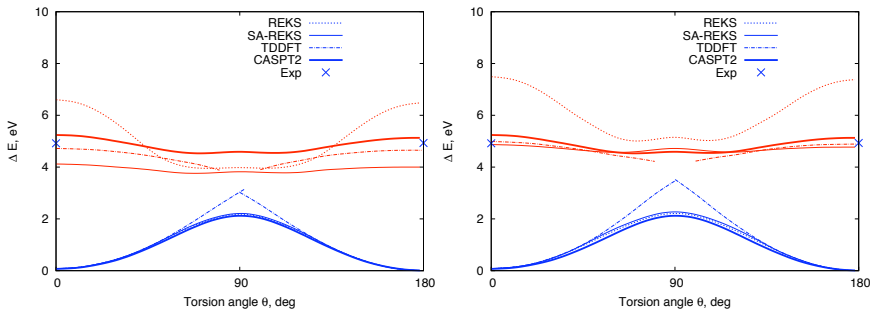

Figure 4.9: *The potential energy profiles along torsional angle $\angle C_2C_3C_4C_5$. The calculated energies corresponding to the 1^1A- state are in red and those corresponding to 1^1B- state are in blue. The TDDFT, REKS and SA-REKS calculations were performed with B3LYP (left) and BH&HLYP (right) exchange-correlation functionals. The DFT ground state energy was obtained by optimization forth $\theta = 0 \div 90$ and back $\theta = 180 \div 90$. The experimental value is from Ref. [164]*

Table 4.3: *The geometry of trans-hexa-1,3,5-triene in the ground ^1A_g state as obtained with different methods. See Fig. 4.8 for atomic labels.*

	REKS	MP2/cc-pVTZ [167]	Experiment [165, 166]
$C_1 = C_2$	1.337	1.350	1.337
$C_2 = C_3$	1.445	1.446	1.458
$C_3 = C_4$	1.346	1.343	1.368
$C_1 = H_2$	1.083	1.082	1.104
$C_1 = H_1$	1.081	1.080	1.104
$C_2 = H_3$	1.086	1.085	1.104
$C_3 = H_4$	1.087	1.086	1.104
$\angle C_1C_2C_3$	124.489	123.678	121.7
$\angle C_2C_3C_4$	124.300	123.684	124.4
$\angle C_2C_1H_2$	121.497	120.860	120.5
$\angle C_2C_1H_1$	121.652	121.410	120.5
$\angle C_4C_3H_4$	118.944	118.966	115.0
$\angle C_3C_2H_3$	116.407	116.908	121.3

4.4). Both density functionals employed, B3LYP and BH&HLYP, predict the excitation energies within 0.3 eV from the experimental figure. For small twisting angles, the profile of the excited state PES along the minimal energy path of the C_3–C_4 twisting obtained in the TDDFT calculations follows reasonably well the PES obtained in the (6,6)CASPT2 calculations. However, beyond *ca.* 50° of twist the TDDFT excited state PES begins to deviate from the shape predicted by (6,6)CASPT2 and around *ca.* 80° of twist the TDDFT description of the excited state breaks down. Beyond this twisting angle, it was not possible to obtain converged TDDFT excitation energies.

Table 4.4: *The energies of $S_1 \leftarrow S_0$ excitation and the barrier to rotation α about the central double bond in trans-hexa-1,3,5-triene.*

Functional	α	State	REKS	SA-REKS[a]	TD-DFT	CASPT2	Exp[b]
1[c]	180	S_0	-	-	-	-	-
		S_1	6.49	4.04	4.65	5.13	4.93
	90	S_0	2.18	2.19	3.03	2.12	-
		S_1	3.98	3.93	-	4.59	-
2[d]	180	S_0	-		-	-	-
		S_1	7.47	4.77	4.89	5.13	4.93
	90	S_0	2.19	2.27	3.52	2.12	-
		S_1	5.13	4.72	-	4.59	-

[a] Equal weighting factors are used in the state-averaged calculations.
[b] From Ref. [164].
[c] B3LYP.
[d] BH&HLYP.

The excited state PES obtained in the REKS calculation using the orbitals optimized for the ground state alone, shows fairly strong deviation from both the experimental excitation energy and from the (6,6)CASPT2 PES for the planar *trans*-hexa-1,3,5-triene. Similar to the case of the ground state of planar ethylene this can be explained by the fact that the LUMO in the ground state is empty and is thus poorly optimized in the REKS calculation. When the twisting angle approaches 90°, the non-dynamic correlation leads to (nearly) equal populations of the HOMO and LUMO and both orbitals are optimized in the REKS calculation equally well. Thus the part of the excited state PES which corresponds to these twisting angles is reproduced fairly well in the state-specific REKS calculations.

Switching to the state-averaged REKS method brings in a considerable improvement of the excited state PES. The excitation energy of the planar *trans*-hexa-1,3,5-triene is lowered by almost 3 eV, which brings this energy in much better agreement with the experimental and (6,6)CASPT2 energies. Such a huge energy lowering due to using state-averaged approach can be explained by the difference in the shapes of frontier orbitals obtained in state-specific and state-averaged calculations. The HOMO and LUMO of the planar *trans*-hexa-1,3,5-triene optimized with respect to the energy of the ground state only and the orbitals optimized with respect to the average energy of the ground and excited states, $0.5E_{g.s.} + 0.5E_{e.s.}$, are shown in Figure 4.6. It is clearly seen that the orbitals optimized in the state-averaged approach are more delocalized as compared to the orbitals optimized with respect to the ground state energy alone. This is a clear reflection of the ionic nature of the excited state of hexatriene. In comparison with ethylene, the frontier orbitals of which optimized using the two approaches are shown in Figure 4.7, there is much more pronounced change in the shape of the frontier orbitals with the use of the state-averaged approach. Indeed, in ethylene, the shape of the frontier orbitals is defined primarily by molecular symmetry and the possibilities for delocalization of the HOMO and LUMO are fairly limited. Thus the excitation energy changes by *ca.* 1 eV only when switching from the state-specific to the state-averaged method. In hexatriene, the delocalization of frontier orbitals along the terminal double bonds take place which leads to a more pronounced effect on the excitation energy. This comparison demonstrates the superiority of the state-averaged method over the state-specific one for the calculation of excitation energies.

The shape of the excited state PES along the C_3–C_4 twisting mode obtained in the SA-REB3LYP and in the SA-REBH&HLYP calculations follows the shape of the (6,6)CASPT2 PES for all twisting angles. It is interesting that, similar to the case of ethylene twisting, the SA-REBH&HLYP PES coincides with the respective TDDFT PES for small twisting angles. In this region, the non-dynamic correlation is weak and the single-reference description of the ground state is sufficient. It is gratifying that, for large twisting angles, the SA-REBH&HLYP PES is nearly indistinguishable from the (6,6)CASPT2 PES. This demonstrates that, for all twisting angles, the SA-REKS method is capable of describing the ground and excited potential energy surfaces with high accuracy.

4.3 Conclusions

The present work was motivated by the necessity to describe the excited states of molecules in the ground states of which the strong non-dynamic electron correlation is present. Diradicals in the low-spin states, molecules with partially dissociated

bonds are typified by the presence of the non-dynamic correlation resulting from near degeneracy of several electronic configurations. [138, 168] The correct description of the ground states of these molecules can be achieved with the use of the so-called spin-restricted ensemble-referenced Kohn-Sham (REKS) method, [118] in which the non-dynamic correlation is taken into account via the use of fractional occupation numbers of several frontier Kohn-Sham orbitals resulting from the ensemble averaging of a few non-interacting KS reference determinants. Previously, this approach has been successfully applied to study the ground states of various diradicaloid species [118, 121–124, 127] and the present work extends its domain of applicability to the excited states.

The new method suggested in the present work is based on the use of the variational principle for optimizing the energy of the ensemble of states, the ground state and the excited state created by single excitation from the ground state. While the variational optimization of the excited state energy w.r.t. its own density is not permitted in DFT,[108, 119, 120, 129–132] the variational optimization of the ensemble is allowed. [112–114]

In the present work, we have formulated and tested a state-averaged version of the REKS method, in which the KS orbitals are optimized with respect to the weighted sum of the energies of the ground state and the singly excited state. The ground state energy is represented as in the ground state REKS method, whereas, for the excited open-shell singlet state, the ROKS formalism is employed.

In the calculations of several model systems, which include the hydrogen molecule with stretched bond, twisting about the double bond in ethylene and twisting about the central double bond in hexa-1,3,5-triene, the applicability of the new approach to the calculation of the ground and excited state potential energy surfaces has been tested. In comparison with the available experimental data and with the results of *ab initio* CASSCF/CASPT2 calculations, it has been found that the new method, SA-REKS, is capable of describing the ground and excited state PESs with high accuracy. The excited state PESs obtained with SA-REKS, correctly reproduce the shape predicted by the high-level *ab initio* method. The magnitude of the excitation energies obtained in the SA-REBH&HLYP calculations are within 0.2 eV from the experimental values. It should be noted that the TDDFT description of the excited state PESs breaks down in the systems typified by the strong non-dynamic correlation and unrealistic excitation energies result in these situations. However, in situations where the near degeneracy effects are not present, such as the ground state of planar ethylene or of planar hexa-1,3,5-triene, the TDDFT formalism yields accurate excitation energies. It is gratifying that, for these systems, the new SA-REKS method is capable of reproducing the TDDFT results. Thus, the new method describes accurately the lowest singlet excited states in both situations, when the

near degeneracy effects are strong and when they are weak or absent. This method is therefore well suited for modeling of the photoisomerization processes.

Chapter 5

S_0 and S_1 PESs of biphenanthrylidene-based molecular motor

5.1 Introduction

Light-driven rotary molecular motors based on helical overcrowded alkenes represent a new promising class of functional compounds. Optical control of the rotary motion in these compounds is achieved via the *cis* to *trans* isomerization of a carbon-carbon double bond which allows for a 180° rotation of one part of the molecule (rotor) with respect to another (stator). One of the first synthetic compounds in this class is the (3R,3'R)-(P,P)-trans-1,1',2,2',3,3',4,4'-octahydro-3,3'-dimethyl-4,4'-biphenanthrylidene (**1**), which contains two identical fragments connected by a central carbon-carbon double bond. [169, 170] Unidirectional rotation around the central double bond is carried out in four steps (strokes): two photo-isomerization steps interconnected by two thermal relaxation steps shown schematically in Figure 5.1.

Fast light-induced isomerization (P,P)-*trans*-**1** to (M,M)-*cis*-**2**, in the first stroke, is followed, in the second stroke, by the thermal relaxation to a more stable (P,P)-*cis*-**2** isomer, which is photoisomerized, in the third stroke, to the (M,M)-*trans*-**1** and, in the fourth stroke, relaxes thermally to the starting conformation (P,P)-*trans*-**1**.[169, 170] Experimental observations suggest the occurrence of a unidirectional rotation in this system whereby the direction of rotation is governed by the helicity, (P,P) or (M,M), and the configuration at the stereogenic centers, (3R,3'R) or (3S,3'S), around the central carbon-carbon double bond.[170]

The maximum rotation rate is restricted by the rate of the thermally controlled helicity inversion steps. A substantial progress in adjusting these energy barriers by various structural modifications has led to a noticeable increase in the rotation rate.[171, 172] At the same time, the photo-induced steps remain less studied and possibilities for their modification/optimization are much less investigated. In a recent ultrafast optical study of a rotary molecular motor, a mechanism of the photoisomerization step schematically shown in Fig. 5.2 was suggested on the basis of experimental results.[173]

In particular, it was hypothesized[173] that the landscape of the potential energy

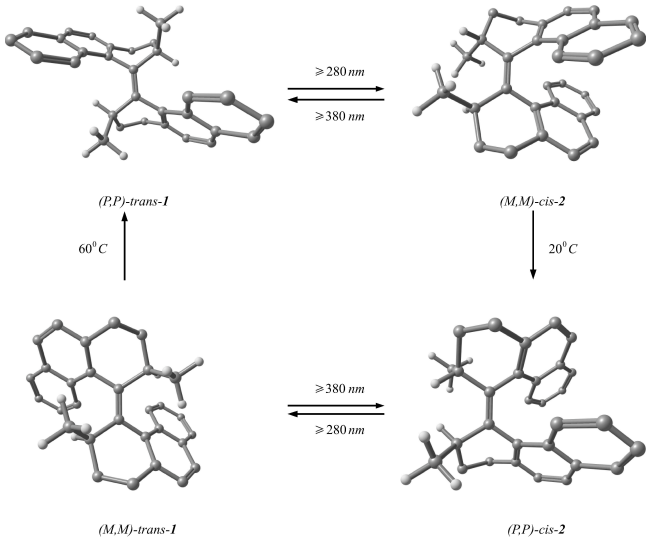

Figure 5.1: *The four-stroke cycle of rotation in (3R,3'R)-(P,P)-trans-1,1',2,2',3,3',4,4'-octahydro-3,3'-dimethyl-4,4'-biphenanthrylidene molecular motor. [169]*

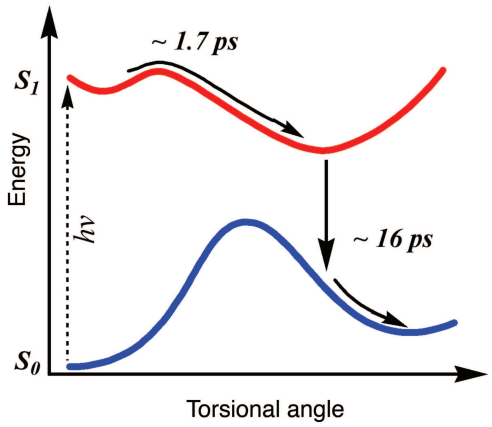

Figure 5.2: *Schematic representation of the mechanism of trans-cis photoisomerisation in a rotary molecular motor suggested in Ref. [173] on the basis of ultrafast optical experiments.*

surface (PES) of the first excited singlet state S_1 along the twisting mode features a minimum the position of which is displaced with respect to the maximum on the

ground S_0 PES towards the isomerized product. Thus, upon a photoexcitation, the molecule undergoes a very fast (*ca.* 2 ps) twisting motion which ends up in a conformation matching the product of isomerization. The subsequent relaxation to the ground state PES (*ca.* 16 ps) brings the molecule to the final isomer.[173] Although within this essentially one-dimensional twisting model relaxation to the ground state and occurrence of the conical inresections can not be described, an attractive feature of this model is that the preferred direction of rotation can be seen already at the photoisomerization stage as given by the slope of the potential energy surface of the excited state.

To verify this model, we undertake, in the present work, a SA-REKS and TDDFT investigation of the potential energy surfaces of the ground and the lowest excited singlet states at the first and third (photoisomerization) steps in Figure 5.1. The major question which is addressed in this study is whether the potential landscapes of the ground and the first excited singlet states of the (3R,3'R)-(P,P)-trans-1,1',2,2',3,3',4,4'-octahydro-3,3'-dimethyl-4,4'-biphenanthrylidene in different conformations can contribute to better understanding of unidirectionality of the rotation. Of course, complete modeling of the rotation process should include molecular dynamics simulations and should address the problem of radiationless relaxation to the ground state. To approach the latter problem one needs to analyze the non-adiabatic coupling vectors along possible trajectories on the excited state surface and to locate conical intersection points (seams) between the surfaces. The conical intersections are known to be very efficient funnels of radiationless relaxation processes.[174–176] However to locate these points (or seams) one needs to go beyond the one-dimensional model and to take into account other degrees of freedom, such as a pyramidalization motion. An extended investigation of the potential energy surfaces which considers additional degrees of freedom is presented in the Chapter 6.

5.2 Calculation of PE profiles

The potential energy surface of the ground and the first excited singlet states of compound **1** have been studied with the use of state-averaged (SA) variant of the REKS method.[178] The minimal energy path (MEP) on the ground state potential energy surface (PES) along the $C_4{=}C_{4'}$ twisting mode (see Fig. 5.3) has been scanned with the use of the REKS method [118, 121–123, 127] for the (P,P)-*trans*-**1** to (M,M)-*cis*-**2** and for the (P,P)-*cis*-**2** to (M,M)-*trans*-**1** transitions. The B3LYP hybrid density functional [150] was employed in the PES scans.

Using the geometries obtained in the PES scan steps, the ground (S_0) and the first excited singlet (S_1) state energies have been calculated with the use of the SA-REKS method.[178] Along with the SA-REKS method, the time-dependent DFT

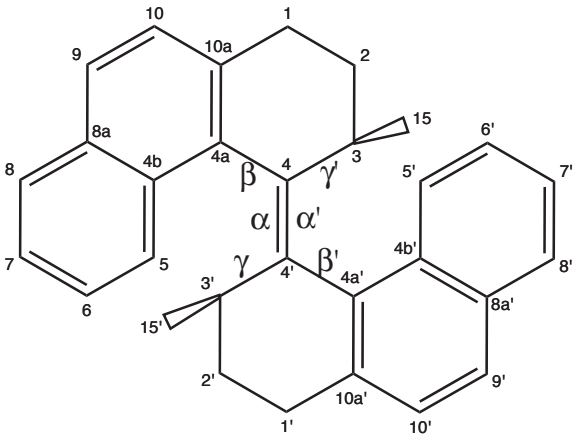

α=(4a, 4, 4',4a'); α'=(3, 4, 4',3')
β=(4', 4, 4a,4b); β'=(4, 4', 4a',4b')
γ=(4, 4', 3',15'); γ'=(4', 4, 3,15)
ζ=(3, 4, 4',4a); φ=(3, 4, 4')
1=44'; 2=44a; 3=4a10a;
4=10a1; 5=12; 6=23; 7=34

Figure 5.3: *The numbering of atoms in (3R,3'R)-(P,P)-trans-1,1',2,2',3,3',4,4'-octahydro-3,3'-dimethyl-4,4'-biphenanthrylidene.*

(TD-DFT) formalism[23] has been used in the (S_0) and (S_1) PES calculations. The excited state calculations with both formalisms employed the BH&HLYP density functional.[86, 151] Although the use of the BH&HLYP functional in the TD-DFT calculations leads to somewhat inferrior excitation energies than with the B3LYP functional, [177] this functional is employed in the present work because it provides a better compensation for the self-interaction error, which is important for the SA-REKS calculations [178] as has been pointed out in the Chapter 4.

The basis set employed in the MEP scan was constructed from the standard 6-31G* basis set [149] on the central atoms and the STO-3G basis set[179] on the peripheral atoms. Stability of the so-obtained geometries with respect to basis set extension was checked at a number of points along the MEP by replacing this basis with the 6-31G* basis on all atoms. In the SA-REKS and TD-DFT calculations for the S_0 and S_1 PES, the 6-31G* basis set on all atoms was employed. At a number of selected points along the MEP, the calculations with the 6-311G** basis set[149]

have been carried out to assess the significance of basis set effects.

5.3 Results and discussion

The results of the calculations are collected in Table 5.1 and in Figure 5.4. The optimized geometries are shown in the Tab. 5.2.

Table 5.1: *The vertical excitation energies in the (P,P)-trans-***1** *and (P,P)-cis-***2** *conformations. The geometries optimized with two different basis sets*[a] *were used. The excitation energies were calculated with the use of TD-BH&HLYP and SA-REBH&HLYP and three different basis sets*[b]*. Deviations from the experimental data are shown. All energies are in eV.*

	SA-REKS				TDDFT			
	A		B		A		B	
(P,P)-*trans*-**1**								
	S_1-S_0	Error	S_1-S_0	Error	S_1-S_0	Error	S_1-S_0	Error
1	4.87	0.81	4.88	0.82	4.79	0.73	4.80	0.74
2	4.47	0.41	4.50	0.44	4.27	0.21	4.30	0.24
3	4.41	0.35	4.44	0.38	4.19	0.14	4.23	0.17
Exp.[c]	4.06		4.06		4.06		4.06	
(P,P)-*cis*-**2**								
	S_1-S_0	Error	S_1-S_0	Error	S_1-S_0	Error	S_1-S_0	Error
1	4.65	0.44	4.65	0.44	4.63	0.42	4.63	0.42
2	4.23	0.02	4.29	0.08	4.17	-0.04	4.20	-0.01
3	4.18	-0.03	4.24	0.03	4.10	-0.11	4.14	-0.07
Exp.[c]	4.21		4.21		4.21		4.21	

[a] A: REB3LYP/hybrid 6-31G*/STO-3G optimized structures; B: REB3LYP/6-31G* optimized structures.
[b] 1: hybrid 6-31G*/STO-3G; 2: 6-31G*; 3: 6-311G**
[c] Cited from Ref. [169].

Figure 5.4 shows the profiles of the S_0 and S_1 PES along the MEP on the ground state surface. For both photo-isomerization steps, (P,P)-*trans*-**1** to (M,M)-*cis*-**2** and (P,P)-*cis*-**2** to (M,M)-*trans*-**1**, the REKS method yields smooth PESs which feature potential energy barriers of 2.11 eV and 2.26 eV on the S_0 surfaces at the twisting angles near -100° and 95° of twist, respectively. These barriers originate from the avoided crossing between the diabatic $(...\pi^2)$ and $(...(\pi^*)^2)$ states which result from breaking of the C_4=$C_{4'}$ double bond near 90° of twist.[136, 138] In a re-

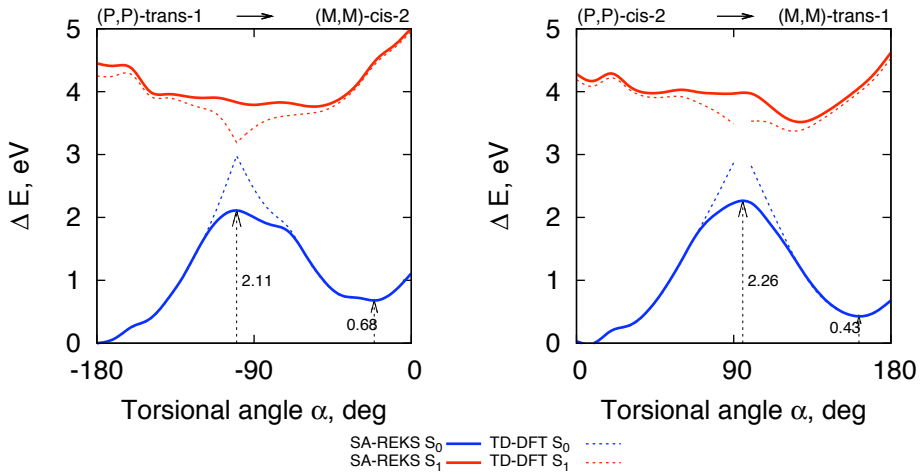

Figure 5.4: *The profiles of the S_0 and S_1 PES for (P,P)-trans-***1** *to (M,M)-cis-***2** *(left panel) and (P,P)-cis-***2** *to (M,M)-trans-***1** *(right panel) photoisomerization steps along the $C_4 = C_{4'}$ double bond twisting mode. The energies are given relative to the S_0 state energy of the most stable, (P,P)-trans-***1**, *conformation at -180° of twist. The energy difference between (P,P)-trans-***1** *and (P,P)-cis-***2** *in the S_0 state is ca. 0.03 eV. See text for details of calculations.*

cent study, Torras *et al.*[180] with the help of the broken-symmetry spin-unrestricted B3LYP/6-31G* and MP2/6-31G* calculations have obtained somewhat lower energy barriers of 1.36 eV (BS-UB3LYP/6-31G*) and 1.41 eV (BS-UMP2/6-31G*) on the ground state PES of another synthetic molecular rotary motor, 9-(2,3-dihydro-2-phenyl-1H-benz[e]inden-1-ylidene)-9H-fluorene. The experimental estimates for the barrier heights are not available.

The S_1 PESs of the two steps feature minima at -56° (stroke 1) and 129° (stroke 3) of twist, which are displaced with respect to the maxima on the S_0 PESs towards the reaction products. Although the PESs plotted in Figure 5.4 were obtained with the use of the 6-31G* basis set, the extension to the 6-311G** basis set leads to rather modest variation (of *ca.* 0.05 eV) in the obtained excitation energies (see Table 5.1). The geometries obtained in the MEP scan with the combined 6-31G*/STO-3G basis do not substantially change upon replacement with the 6-31G* basis on all atoms. The use of the latter geometries optimized at a few points along the MEP leads to the energy variations in the subsequent SA-REKS calculations of the order of 0.01 - 0.03 eV.

The vertical excitation energies obtained with the use of the SA-REKS method

Table 5.2: *The geometry parameters of the (3R,3'R)-(P,P)-trans-1,1',2,2',3,3',4,4'-octahydro-3,3'-dimethyl-4,4'-biphenanthrylidene molecular motor (see Fig. 5.3 for the labels) in the four conformations: (P,P)-trans-***1**, *(M,M)-cis-***2**, *(P,P)-cis-***2**, *(M,M)-trans-***1** *(denoted in the table as PPT, MMC, PPC, MMT, correspondingly), optimized with B3LYP using two different basis sets and the relative B3LYP ground state energies with respect to PP-trans conformation in eV. The experimental values [169] are shown in brackets*

	6-31G*/STO-3G				6-31G*			
	PPT	MMC	PPC	MMT	PPT	MMC	PPC	MMT
α	186.6	-17.8	2.2 (-3.2)	160.1	188.6	-17.6	0.9 (-3.2)	161.1
α'	-165.6	-21.2	5.4 (5.9)	151.7	-164.0	-22.7	7.2 (5.9)	150.8
β	67.1	-46.1	54.1 (54.4)	-44.0	68.6	-48.2	56.1 (54.4)	-45.1
γ	-121.8	-41.8	-94.3 (-97.0)	-44.8	-118.9	-40.3	-95.1 (-97.0)	-44.1
γ'	-121.8	-41.8	-94.3 (-96.0)	-44.8	-118.9	-40.3	-95.1 (-96.0)	-44.1
ζ	190.5	178.3	181.6	175.8	192.3	177.4	183.1	174.8
φ	124.3	120.7	124.4	122.1	123.7	120.9	124.9	122.1
1	1.356	1.377	1.362 (1.347)	1.378	1.357	1.377	1.361 (1.347)	1.378
2	1.495	1.500	1.494	1.495	1.494	1.498	1.493	1.492
3	1.399	1.402	1.400	1.406	1.393	1.396	1.394	1.399
4	1.523	1.520	1.523	1.520	1.509	1.506	1.509	1.506
5	1.569	1.558	1.562	1.558	1.544	1.535	1.538	1.535
6	1.580	1.562	1.569	1.556	1.570	1.551	1.558	1.545
7	1.532	1.559	1.541	1.563	1.532	1.557	1.540	1.559
ΔE	0.00	0.56	-0.01	0.45	0.00	0.62	0.03	0.43

and the 6-311G** basis set[149] for the (P,P)-*trans*-**1** (4.41 eV) and (P,P)-*cis*-**2** (4.18 eV) conformations are in a reasonable agreement with the available experimental data of 4.06 eV and 4.21 eV, respectively (see Table 5.1). It is noteworthy that the SA-REKS results (4.41 eV and 4.18 eV) are in a reasonably close agreement with the TD-DFT results for the two isomers, 4.19 eV and 4.10 eV, respectively. However, near the potential energy barrier on the ground state PES of both species, the single reference description employed in the TD-DFT formalism breaks down and the method can not produce reliable excitation energies for these geometries.[178] This can be seen from the cusp on the S_0 PES and from the discontinuity of the S_1 PES as obtained in the TD-DFT calculations. However, near the energy minima on the ground state PES, where the single reference description is sufficiently adequate, the S_0 and the S_1 surfaces obtained in the SA-REKS and in the TD-DFT calculations are in a good agreement with one another. The relative energies of the thermally unstable products of the photoisomerization steps, (M,M)-*cis*-**2** and (M,M)-*trans*-**1** with respect to the starting conformations (P,P)-*trans*-**1** and (P,P)-*cis*-**2** are predicted to be 0.68 eV and 0.43 eV, respectively, with the use of both SA-REKS and TD-DFT methods.

The most striking feature of the obtained PESs of the ground and the first excited singlet states of the compounds **1** and **2** is the mismatch between the maxima on the S_0 PES and the minima on the S_1 PES. If one considers possible evolution of the molecular geometry of these species upon excitation, the most likely scenario

is the relaxation of the geometry towards the minima on the excited state PES. The molecular geometry near these minima matches closely the geometry of the photo-isomerization products, the (M,M)-*cis*-**2** and the (M,M)-*trans*-**1** species. This observation suggests that the relaxation to the ground S_0 state may proceed from a conformation which already matches the isomerization products. Therefore the probability of falling back to the reactants should be rather small. Thus, the profile of the ground S_0 and the excited S_1 surfaces corroborates the observed uni-directionality of rotation in these species.[169, 170]

Let us now turn to the electronic factors underlying the observed preference for the (M,M)-*cis*-**2** and the (M,M)-*trans*-**1** conformations on the excited state PES. Upon the photoexcitation of the reactants, (P,P)-*trans*-**1** and (P,P)-*cis*-**2**, the central C_4=$C_{4'}$ double bond is broken due to excitation of one electron from the π bonding to the π^* anti-bonding orbital of this bond. Therefore, the electronic structure of the excited S_1 state can be described as originating from a weak coupling between two substituted 1-methylnaphthyl radicals connected via a single C–C bond, see Fig. 5.5.

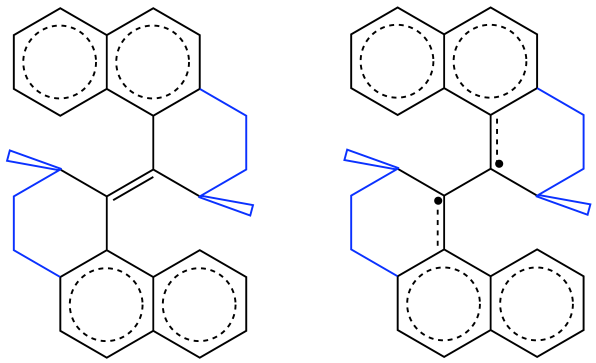

Figure 5.5: *Schematic representation of the leading Lewis structures of (3R,3'R)-(P,P)-trans-1,1',2,2',3,3',4,4'-octahydro-3,3'-dimethyl-4,4'-biphenanthrylidene in the ground (left panel) and the exited (right panel) states. The substituents to the 1-methylnaphthyl radicals are shown in blue.*

In such a configuration, the π-conjugation between the C_4 and C_{4a} ($C_{4'}$ and $C_{4a'}$) is much stronger than in the ground state where the double C_4=$C_{4'}$ bond is relatively weakly conjugated with the naphthyl rings. Therefore, one can conjecture that, in the excited states, the deviation from the planarity of the 1-methylnaphthyl groups should result in a destabilization of the whole structure and vice versa.

To test this hypothesis, we have undertaken density functional calculations of the (appropriately substituted) 1-methylnaphtyl radical in the conformations taken from

the geometries of the points on the MEP of **1** and **2** at -180°, -130°, -50°, 10°, and 130° of twist (see Figure 5.6).

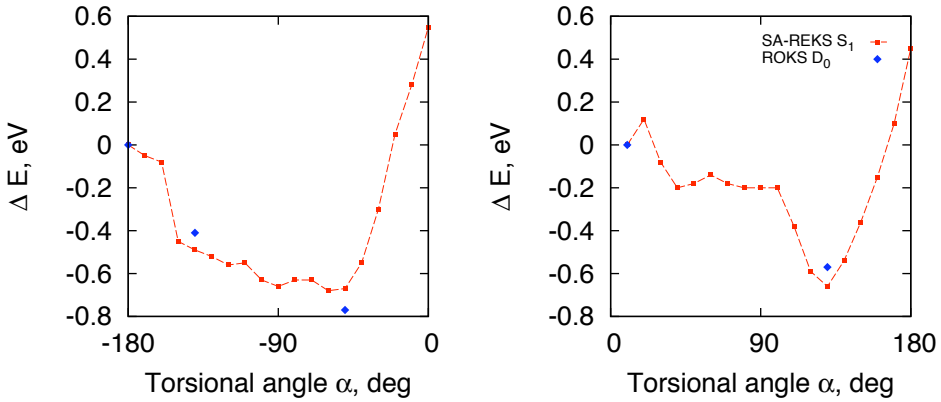

Figure 5.6: *The energies of two substituted 1-methylnaphtyl radicals in comparison with the profiles of the excited state PES of both photoisomerization steps. The energies are given relative to the energy of the substituted 1-methylnaphtyl radical at -180° of twist (left panel) and at 10° of twist (right panel). See text for details of calculations.*

The relative energies (with respect to the -180° structure) of two isolated 1-methylnaphtyl radicals obtained from the ROKS/BH&HLYP/6-31G* calculations[106, 107, 146, 147] in these conformations are shown in Figure 5.6 in comparison with the profiles of the excited state PESs for both photo-isomerization steps. It is clearly seen that the minimum on the excited state PES originates due to the stabilization in the 1-methylnaphtyl radical units. Near the minima, the (M,M)-*cis*-**2** and the (M,M)-*trans*-**1** isomers adopt conformations in which the C_{4b}-C_{4a}-C_4-$C_{4'}$ ($C_{4b'}$-$C_{4a'}$-$C_{4'}$-C_4) dihedral angle is close to planarity thus providing better π-conjugation within the 1-methylnaphtyl radical units.

The ground state geometries of the (M,M)-*cis*-**2** and the (M,M)-*trans*-**1** conformations are strongly influenced by the steric repulsion between the lobes of the molecular rotor. The increased steric repulsion (as compared to the more stable (P,P)-*trans*-**1** and (P,P)-*cis*-**2** conformations) leads to an elongation of the central C_4=$C_{4'}$ double bond which then acquires some diradicaloid character. This, in turn, leads to a stronger π-conjugation between the C_4 and C_{4a} ($C_{4'}$ and $C_{4a'}$) atoms similar to that observed in the excited state. It is obvious therefore that the C_{4b}-C_{4a}-C_4-$C_{4'}$ ($C_{4b'}$-$C_{4a'}$-$C_{4'}$-C_4) dihedral angle in the ground state (M,M)-*cis*-**2** and (M,M)-*trans*-**1** conformations will be closer to planarity than in the more stable (P,P)-*trans*-**1**

and (P,P)-*cis*-**2** conformations. This discussion implies that there is a correlation between the preference for the (M,M)-*cis*-**2** and the (M,M)-*trans*-**1** conformations on the excited state PES and their geometry near the corresponding minima on the ground state PES. Therefore, one can argue that the true energy minimum on the excited state PES of the above species can be found for the molecular geometry which strongly resembles the structure near the minimum on the ground state PES.

Although the profiles of the S_0 and S_1 PESs of **1** and **2** presented in Figure 5.4 may help one to explain the origin of the observed uni-directionality of rotation during the photo-isomerization steps in Figure 5.1, the mechanism of relaxation to the ground state is not yet fully rationalized. The most likely scenario of the radiationless $S_0 \leftarrow S_1$ relaxation is that it proceeds via the non-adiabatic coupling to vibrational modes. Occurrence of the conical intersection (CI) points (or seams)[174–176] between the S_0 and S_1 surfaces near the minima on the excited state PESs of both species can indicate clearly the strength of non-adiabatic coupling in these regions. To find the CI points (see *e. g.* Ref. [181] for a recent review on the search algorithms) one needs to go beyond the effectively one-dimensional model shown in Figure 5.4 and to consider motion of the lobes of molecular rotor along other degrees of freedom, such as the pyramidalization motion at the C_4 and $C_{4'}$ atoms. The search for the CI points of a similar molecular motor is discussed in Chapters 6 and 8.

5.4 Conclusion

In this work, we have undertaken a density functional study of the potential energy surfaces of the ground S_0 and the first excited singlet S_1 states of the (3R,3'R)-(P,P)-trans-1,1',2,2',3,3',4,4'-octahydro-3,3'-dimethyl-4,4'-biphenanthrylidene (**1**) molecular motor. The S_1 excited state potential energy surface obtained in the SA-REKS calculations along the minimal energy path connecting the (P,P)-*trans*-**1** to (M,M)-*cis*-**2** conformations and the (P,P)-*cis*-**2** to (M,M)-*trans*-**1** conformations feature minima near the molecular geometries matching the isomerization products, (M,M)-*cis*-**2** and (M,M)-*trans*-**1**. Occurrence of the minima on the excited state PES is explained by the improved π-conjugation within the C_4-C_{4a}-C_{4b}-C_{10a} ($C_{4'}$-$C_{4a'}$-$C_{4b'}$-$C_{10a'}$) fragments (see Figures 5.3 and 5.5) in these conformations. The slope on the S_1 PESs of both conformations indicates that there is a preferred direction of rotation upon photoexcitation of the molecular motor. These theoretical findings are consistent with the conclusions made by Augulis *et al.*[173] on the basis of ultrafast optical experiments.

The results of the present study suggest that upon photoexcitation to the S_1 state, the molecular geometry of (P,P)-*trans*-**1** ((P,P)-*cis*-**2**) evolves quickly towards the isomerization product whereupon relaxation to the ground S_0 state occurs due to the

non-adiabatic coupling with the vibrational modes. Although, in the present work, we do not report on the study of the radiationless relaxation process, the preliminary results obtained so far indicate that there is a conical intersection between the S_0 and S_1 PESs near the minimum on the S_1 surface. The presence of conical intersection points indicates a strong non-adiabatic coupling [175] in the regions adjacent to the minima on the S_1 PES. An investigation of the dynamics of radiationless relaxation for a structure similar to **1** is undertaken in the Chapter 6 and a search for the conical intersection points (seams) is discussed in Chapter 8.

Chapter 6

Fluorene-based Molecular Motor: hybrid quantum-classical simulation

6.1 Introduction

In the previous Chapter we presented a study of the energy profiles of the first generation molecular motor in the S_0 and S_1 states. In this Chapter we discuss a combined quantum chemical and molecular dynamics study of the mechanism of the rotational cycle of the fluorene based molecular rotary motor 9-(2,4,7-trimethyl-2,3-dihydro-1H-inden-1-ylidene)-9H-fluorene within this chapter denoted as **1**. The potential energy surfaces of the ground and excited singlet states of **1** were calculated and it is argued that the conical intersections play a central role in the mechanism of photo conversion between the stable conformer of **1** and its metastable conformer. Molecular dynamics simulations indicate that the average life time of the fluorene motor in the excited state is 1.40±0.10 ps when starting from the stable conformer, which increases to 1.77±0.13 ps for the reverse photoisomerization. These simulations indicate that the quantum yield of photoisomerization of the stable conformer is 0.92 whereas it is only 0.40 for the reverse photoisomerization. A theoretical understanding of the experimentally observed photostationary state of **1** is presented, which provides a qualitative picture of the photoisomerization dynamics in overcrowded alkene based molecular motor **1**. The analysis of the electronic structure of the fluorene molecular motor holds considerable implications for the design of molecular motors. Importantly the role of pyramidalization and conical intersections offer new insight into the factors which dominate the photostationary state achieved in these systems.

Here, we show that quantum chemical, molecular dynamics and experimental data allow for a better understanding of the photoisomerization process. A theoretical investigation of the ground and excited state potential energy surfaces (PESs) of the molecular motor 9-(2,4,7-trimethyl-2,3-dihydro-1H-inden-1-ylidene)-9H-fluorene **1**[62] presents a first step towards understanding the dynamics that lie at the heart of the rearrangements, both photochemical and thermal. In studying the photoisomerization, the key questions that will be addressed are: How important are conical intersections (CIs) and avoided crossing regions in the photochemistry of this motor

(and related compounds)? Can the photostationary state of **1**, in which the ratio of the concentrations of the stable conformer **1-P** to the metastable conformer **1-M** is 1:3, [62] be modified in a predictable manner? In determining the relative contribution of CIs and avoided crossings what implications does the electronic structure of **1** have for the design of molecular motors? These questions will be addressed in a combined quantum chemical and molecular dynamics study of the operation cycle of the motor **1**, in which quantum chemistry is used to describe the energy landscape and molecular dynamics to use this landscape to predict empirically observed properties.

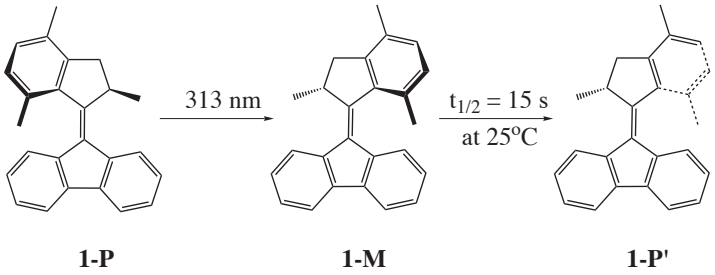

Figure 6.1: *The photochemical and thermal components of the rotary cycle of fluorene based molecular motor **1**.*

Currently, it is widely accepted that CI points or seams play a crucial role for the photochemistry of molecules as they represent funnels for highly efficient radiationless relaxation [17]. With the advent of ultra-fast optical spectroscopic methods [182] it has become apparent that the excited states of molecules undergo transformation and radiationless relaxation to the ground state on too fast a timescale to be described in terms of the non-adiabatic coupling in the avoided crossing regions alone [17]. The role of CIs in molecular photochemistry and for predicting the direction of molecular photo-rearrangements has been recognized since the pioneering work of Yarkony [183] and Robb [184]. A clear example is the understanding of the photochemistry of small organic alkenes, such as ethylene, for which CIs occur upon pyramidalization of one of the carbon atoms accompanied by a twist about the double bond. This plays a crucial role in the course of the photorearrangement of ethylene, stilbene, *etc.* [17, 185–187]

Thus, in the present study, the dynamics behind the photoisomerization of **1** are explored employing a balanced description of the avoided crossing regions and the regions where CI points or seams occur. Although such a description can be provided reliably by high level multi-reference ab initio methods, the application of these methods to fluorene based, and indeed many other molecular motors, is restricted by the sheer size of these molecules. Therefore, in this work, we employ the SA-REKS computational scheme [178, 188] based on the ensemble approach [95, 118, 189] within

density functional theory (DFT) [87, 128]. This approach is capable of providing a reliable description of the ground and excited states of molecular systems in which processes of bond breaking and bond formation occur based on comparison with empirical data [118, 121–124, 127, 178, 188]. This computational scheme will be applied in the present study to understand the ground and excited state potential energy surfaces of **1** along the internal coordinates describing the twisting motion about the central double bond and pyramidalization of one of the adjacent carbon atoms. Based on the computational results the geometric distortions necessary for **1** to reach the CIs will be analyzed and a sequence of geometric transformations that the molecular motor undergoes during its photochemical isomerization will be constructed. The data obtained for the ground and excited state potential energy profiles will be used to parametrize a suitable force field for molecular dynamics simulations and the dynamics of photorearrangement are thereby studied. The results of the theoretical calculations are considered in the context of the experimentally observed photostationary state of **1** [62] and of the results of a recent ultra-fast transient absorption study of the excited state dynamics of molecules related to **1**. [190] The theoretical results obtained hold considerable implications in achieving a rational synthetic design of future molecular motors with application defined functionality.

6.2 Theoretical methods

The ground state PES of the motor **1** was studied using the B3LYP density functional [86, 151, 191]. The Gaussian 03 quantum chemical program [192] was used in these calculations. In the calculations on the first step of the operation cycle of **1** (see 6.1), during which breaking of the central C_9–$C_{1'}$ double bond occurs, the spin-restricted ensemble-referenced Kohn-Sham (REKS) method [118, 121–124, 127] was used in combination with the B3LYP functional. The REKS method is capable of correctly describing the systems where avoided crossing of the PESs occurs due to near degeneracy of several electronic configurations, such as molecules with broken bonds. In the ground state calculations, the 6-31G* basis set [149] was employed on all atoms. The REKS and SA-REKS calculations were carried out with the use of the Cologne08 code [148].

The excitation energies and the lowest singlet excited state PES of **1** were calculated with the use of a recently developed state-averaged (SA) variant of the REKS method.[178, 188] In these calculations the BH&HLYP density functional was employed, because it provides for a better compensation of the self-interaction error of the approximate density functional [158, 159], which is important for the SA-REKS calculations.[178, 188] The functionals with increased fraction of the exact exchange, such as the BH&HLYP density functional, are capable of accurately describing the excited states with electron transfer character [193] and provide balanced description of the zwitterionic excited states within the SA-REKS formalism.[178, 188] In the SA-REKS calculations, the molecular geometries obtained in the ground state PES scans with the RE-B3LYP/6-31G* method were used in combination with the basis sets of varying size ranging from 6-31G* to 6-311+G**. A coarse grid with an increment of 10° for dihedral angles was used in these scans that was supplemented with a finer grid with an increment of 1° in the vicinity of conical intersections. For comparison, the TD-DFT calculations with the BH&HLYP functional were carried out for the geometries in proximity of the **1-P** and **1-M** conformers.

The MD simulations were carried out with the Gromacs (v4.0.5) program package. [194] The OPLS all-atom force field[195] was used, with the parametrization of the excited state PES as described in this work. A 1-fs time step was used to integrate the equations of motion, since no constraints were applied to the bonds and angles. No cut-off's were used for the non-bonded interactions.

All MD simulations in the excited state were initiated from equally-spaced snapshots taken from a 1-ns ground state simulation that was equilibrated at -40°C (temperature at which the PSS was experimentally measured) using velocity rescaling temperature coupling according to Bussi *et al.*[196] with a coupling time constant of 0.1 ps. As expected from the large energy barriers on S_0 for double bond isomeriza-

tion and helix inversion, the molecule stayed in the starting conformation during the ground state equilibration. During the subsequent simulations, in which the system was first propagated on S_1 and, after the surface hop, evolved on the S_0 surface, no temperature coupling was applied.

In this work, a surface hopping procedure similar in spirit to the approach of Groenhof *et al.*[197] was followed. A surface hop back to the ground state occurred as soon as the molecule reached the vicinity of the CI seam. The heavy-atom coordinates RMSD from the quantum chemically obtained geometries of the CI_1 and CI_2 points was followed during the S_1 dynamics. A surface hop was imposed as soon as the RMSD to any of the two CI structures dropped below a certain threshold value. This threshold was chosen such that differences between the structures obtained with the force field and the quantum chemical calculations as well as finite-temperature effects are taken into account. To that end, we calculated the heavy-atom RMSD during the equilibrium 1-ns ground state force field MD simulation in the **1-P** conformation with respect to the quantum chemically optimized geometry, which yielded $\langle \text{RMSD} \rangle = 0.2$ Å with a standard deviation of $\sigma = 0.06$ Å. Finally, an RMSD-threshold of 0.32 Å, as defined by adding 2σ to $\langle \text{RMSD} \rangle$, was used in the MD simulations.

6.3 Results and Discussion

The operation cycle of fluorene motor **1** consists of four steps: two photoisomerization steps (power strokes), of which only one is shown in 6.1, and two thermally activated helix inversion steps [62]. The theoretical study begins with the investigation of the ground state PES of the first semi-cycle of **1** as shown in 6.1. Note that, in the ground state of **1**, breaking of the central double C=C bond occurs en route from the stable conformer **1-P** to the metastable conformer **1-M**. The purpose of this part of the study is to evaluate the kinetic stability of the conformers during the operation cycle of motor **1**. The next stage of the study addresses the excited state PES of the **1-P** $\rightarrow$ **1-M** photoisomerization in the regions of avoided crossing of the ground and excited state PESs and near possible CI points or seams. The ground and excited state PESs were scanned along the twisting and pyramidalization modes and the surfaces obtained were used in molecular dynamics simulations. Throughout this Chapter the atomic numbering and the geometric parameters of **1**, which are shown in 6.2, are employed.

6.3.1 Ground state PES of the fluorene rotary motor 1

The ground S_0 state PES of fluorene motor **1** was studied using B3LYP [86, 151, 191] calculations with the 6-31G* basis set [149] and together with the semiempirical PM3

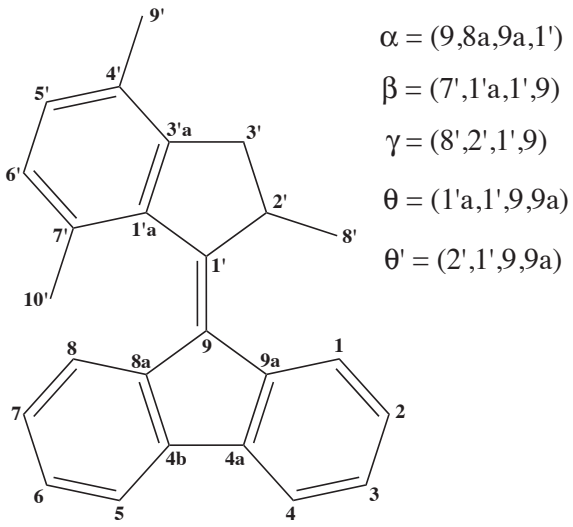

1

Figure 6.2: *Atom numbering scheme and definition of dihedral angles in **1**.*

method [198, 199]. First, the stable conformations of **1** were optimized with the PM3 method and then reoptimized with the B3LYP method. Fluorene motor **1** features two minima in the ground state: the stable conformer **1-P**, in which the methyl group in 2' position adopts the axial orientation, and the metastable conformer **1-M**, in which the methyl group in 2' position is in equatorial orientation with respect to the ring axis (see 6.2). Note that the two identical stable conformers in 6.1 are denoted as **1-P** and **1-P'** to distinguish between the starting orientation of the motor and its orientation after the first half loop. The **1-M** conformer is less stable than **1-P** by 3.45 kcal/mol according to the B3LYP calculations. The most important geometry parameters and relative energies of the two conformers are listed in 6.1.

The S_0 PES for the thermal helix inversion step **1-M** $\rightarrow$ **1-P'** (second stroke in the operation cycle of **1**, 6.1) was first scanned with the PM3 method along the dihedral angles θ (twist about the C_9–$C_{1'}$ double bond) and β (see 6.2 for definitions). According to the calculations, it is these angles that undergo the greatest variation during the thermal helix inversion step **1-M** $\rightarrow$ **1-P'** (see 6.1). All other geometry variables were optimized during the scan. The ground state PES, which is shown in 6.3, reveals that a transition state between the two structures is located at $\theta = 18.1°$

Table 6.1: *Geometry parameters (see 6.2 for definitions) and relative electronic energies of the **1-P** and **1-M** conformations obtained with the B3LYP/6-31G* method and with the PM3 semi-empirical method (angle in deg., bond length in Å, energy in kcal/mol).*

	1-P		**1-M**		**1-P'**	
Parameter	B3LYP	PM3	B3LYP	PM3	B3LYP	PM3
α	1.7	1.7	1.6	1.0	-1.7	-1.7
β	-43.1	-41.0	30.2	22.4	-43.1	-41.0
γ	105.5	98.6	32.3	48.9	105.5	98.6
θ	169.2	168.9	31.5	29.2	-15.6	-15.4
θ'	-22.6	-23.2	-143.4	-147.2	153.0	152.5
$R_{C_9C_{1'}}$	1.368	1.349	1.376	1.354	1.368	1.349
ΔE	0	0	3.45	2.43	0	0

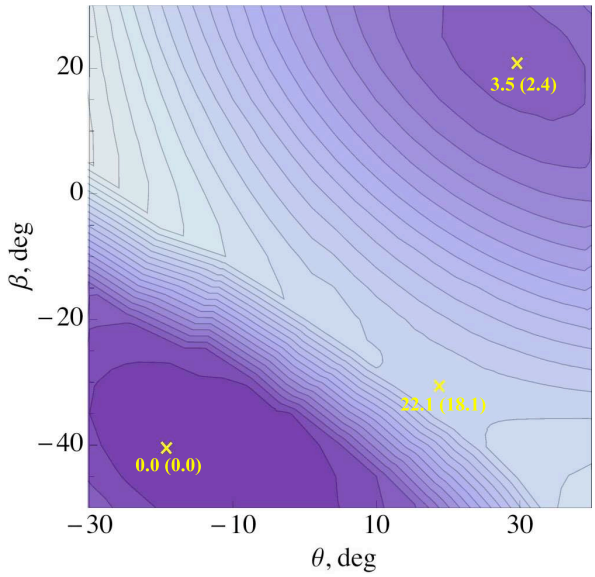

Figure 6.3: *Ground state potential energy surface of the thermal helix inversion step. B3LYP/6-31G* energies outside parentheses, PM3 energies in parentheses.*

and $\beta = -32.2°$ according to the PM3 calculations. Using this geometry as the starting structure, a B3LYP/6-31G* search for transition state has been carried out and the resulting structure ($\theta = 10.8°$ and $\beta = -25.4°$) was characterized by the vibrational analysis. A single imaginary vibrational frequency was found at the

geometry of the transition state with all other frequencies real. The transition state found in the B3LYP/6-31G* calculation lies 22.1 kcal/mol higher than the **1-P'** conformer (see 6.5). Thus, the activation energy $\Delta^{\ddagger}$E for the **1-M** $\rightarrow$ **1-P'** transition is 18.7 kcal/mol which upon correction for the thermal free energy yields $\Delta^{\ddagger}G^{\circ} = 20.0$ kcal/mol. This activation free energy agrees reasonably well with the experimentally estimated $\Delta^{\ddagger}G^{\circ}$ of 18.9 kcal/mol. [62]

The ground state PES of the **1-P** $\rightarrow$ **1-M** step (first stroke in the operation cycle of **1**, 6.1) involves breaking of the C_9=$C_{1'}$ double bond and reliable modeling of this process requires a theoretical method capable of describing strong non-dynamic electron correlations resulting from avoided crossing of the ground and the doubly excited electronic states near 90° of twist. Thus, the spin-restricted ensemble-referenced Kohn-Sham (REKS) method was employed in this work which has proved to be capable of reliably describing electronic states typified by the strong electron correlation [118, 121–124, 127].

For the photoisomerization step **1-P** $\rightarrow$ **1-M**, the ground state PES obtained in the RE-B3LYP/6-31G* calculations is shown in 6.4. This PES was scanned along the twisting angle θ and pyramidalization angle α (see 6.2) with all other geometric parameters fully optimized. This was done for the subsequent modeling of the excited state PES and for the identification of regions where CIs may occur. The dihedral angle α characterizes pyramidalization of the atom C_9 and it was selected for the scan, because reaching a CI between the S_0 and S_1 PESs in alkenes requires both a twist about the double bond and pyramidalization of one of the adjacent carbon atoms [17, 183, 184, 187]. It is noteworthy that pyramidalization of the $C_{1'}$ carbon did not lead to occurrence of CI points as was established in the ground and the lowest excited singlet state calculations (see below). Because we are interested in locating CIs between these states, we did not pursue the $C_{1'}$ pyramidalization in the PES scans.

The ground state PES of the **1-P** $\rightarrow$ **1-M** step features a transition state at $\theta = 91^{\circ}$ and $\alpha = 1^{\circ}$ which lies 32.1 kcal/mol above the stable conformer **1-P** as shown in 6.4 and in 6.5. Thus, there is a substantial energy difference between the barrier heights of the **1-P** $\rightarrow$ **1-M** and the **1-M** $\rightarrow$ **1-P'** steps, which implies that the back transformation **1-M** $\rightarrow$ **1-P** via twist about the C_9=$C_{1'}$ double bond is very unlikely and the thermal isomerization occurs in the direction **1-M** $\rightarrow$ **1-P'** via an inversion of helicity.

6.3.2 Excited state PES of the fluorene rotary motor 1

The lowest singlet excited states of the **1-P** and **1-M** conformers were studied with the TD-BH&HLYP/6-31G* method. In these calculations, the geometries of **1-P** and

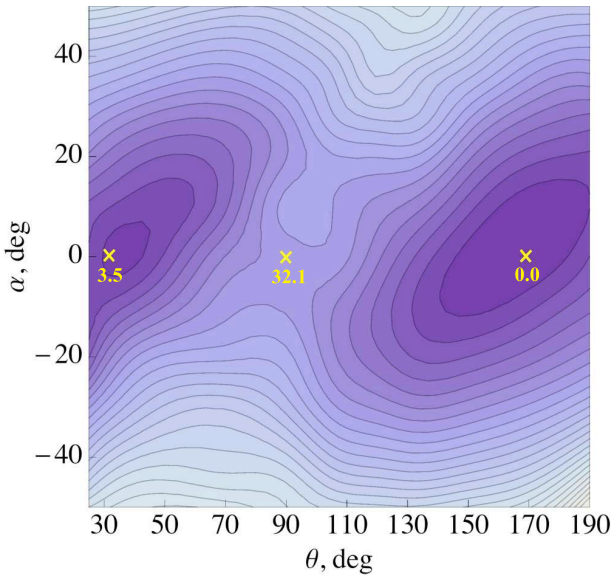

Figure 6.4: *Ground state potential energy surface of the photoisomerization step as obtained with the RE-B3LYP/6-31G* method.*

1-M were taken from the B3LYP/6-31G* calculations. These calculations revealed that the lowest singlet excited state corresponds to the excitation of a single electron from the π-bonding to the π-antibonding orbital of the C_9=$C_{1'}$ double bond. The calculated oscillator strenght of the $S_0 \rightarrow S_1$ excitation is 0.63 in the **1-P** conformer and 0.59 in the **1-M** conformer. The next four transitions have oscillator strenghts below 0.05 and the next significant absorption band is to a state 1.6 eV above the S_1 state. Thus, the S_1 state, which has zwitterionic character and through which the **1-P** $\rightarrow$ **1-M** photoisomerization occurs, is optically accessible. As there are no other signlet excited states below S_1, it is sufficient to consider only this state in the analysis of the **1-P** $\rightarrow$ **1-M** photoisomerization. Note that this is different from the widely accepted models which consider transitions between two (or more) excited states at the early stage of photisomerization of molecules related to **1**, *e.g.* stilbene [200].

The S_1 state of **1** was studied with the use of the state averaged REKS (SA-REKS) method, because this method is capable of describing excitation energies of molecules in regions where strong non-dynamic electron correlation dominates the electronic structure, such as in avoided crossing regions [178, 188]. It is important to note that

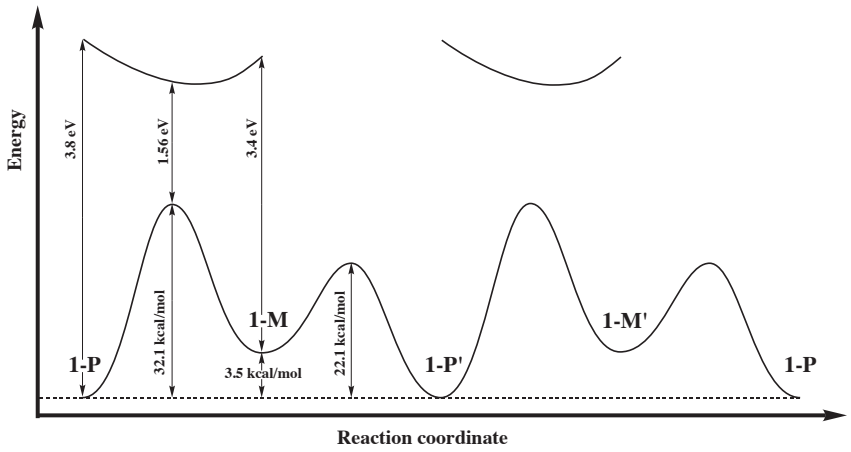

Figure 6.5: *Profiles of the ground (S_0) and the lowest singlet excited (S_1) state potential energy surfaces of **1** along the minimal energy path connecting the stable (P) and the metastable (M) isomers.*

the more widely used time-dependent DFT (TD-DFT) methods [23] can not yield reliable excitation energies in these regions [178]. The $S_0 \rightarrow S_1$ excitation energies of the **1-P** and **1-M** conformers obtained using the SA-REBH&HLYP method and the TD-BH&HLYP method using the 6-31G*, 6-311G**, and 6-311+G** basis sets [149] are listed in 6.2. Experimentally measured maxima of major absorption bands of the **1-P** and **1-M** conformers in hexane at -40°C are 360 nm and 385 nm, respectively [62]. Considering that environment's effects and the vibrational corrections to the excitation energies were not taken into account in the calculations, the agreement with the experimental data is good. There is also a good agreement between the TD-BH&HLYP calculations and the SA-REKS calculations. The time-dependent formalism however is not applicable in the avoided crossing region, near $\theta = 90°$, where breaking of the $C_9{=}C_{1'}$ double bond occurs, whereas the SA-REKS method is capable of reliably describing the lowest excited states of molecular systems with broken bonds. [178, 188]

The ground S_0 and the excited S_1 state PESs obtained in the SA-REBH&HLYP/6-31G* calculations are shown in 6.6 [1]. The S_0 and S_1 PESs were

[1] Note that the SA-REKS method is capable of describing the covalent doubly excited state with the leading electronic configuration $(\ldots \pi^0 \pi^{*2})$. However, these results are not reported here because this state lies above the zwitterionic S_1 state (the gap drops to *ca.* 0.05 eV only near $\theta = 90°$ and $\alpha = 0°$) and does not seem to play a role in the photochemistry of **1**. This can be explained by the asymmetry of **1** which leads to some stabilization of the zwitterionic S_1 state with respect to the

Table 6.2: *Excitation energies, in eV and in nm (in parentheses), of the stable conformers* ***1-P*** *and* ***1-M*** *calculated with the SA-REBH&HLYP and TD-BH&HLYP methods.*

	SA-REBH&HLYP		TD-BH&HLYP	
Basis set	**1-P**	**1-M**	**1-P**	**1-M**
6-31G*	3.80 (327)	3.40 (365)	3.78 (328)	3.39 (366)
6-311G**	3.74 (331)	3.34 (371)	3.72 (333)	3.32 (373)
6-311+G**	3.71 (334)	3.31 (375)	3.68 (337)	3.28 (378)

calculated using the geometries optimized in the RE-B3LYP/6-31G* calculations for the ground state (see above). For comparison, the TD-BH&HLYP/6-31G* calculations were carried out at a number of points on the $\theta - \alpha$ grid. In the regions near the local minima on the ground state PES there is a good agreement between the two methods, similar to that reported in 6.2. However, in the region $80° \leq \theta \leq 110°$ and $-30° \leq \alpha \leq 30°$, where there is an avoided crossing of the two PESs, the TD-DFT formalism fails [178]. In the ground S_0 state, the $(\ldots \pi^2 \pi^{*0})$ and $(\ldots \pi^0 \pi^{*2})$ electronic configurations become (nearly) degenerate and this leads to break down of computational methods based on the single reference description of the ground state [118, 189]. The REKS method can be used in these cases, because it provides a multi-reference description of non-dynamic electron correlation by adopting fractional occupation numbers of the frontier orbitals [118, 121–124, 127].

Near the transition state on the ground state PES ($\theta = 91°$ and $\alpha = 1°$) the energy gap between the S_0 and S_1 states as obtained in the SA-REBH&HLYP/6-31G* calculation amounts to 1.56 eV. With increase in the angle α, the gap between the surfaces narrows down and at $\alpha = 34°$ and $\theta = 120°$ it becomes 0.16 eV (3.7 kcal/mol). This small value indicates the presence of CI near this geometry. [201] Because analytic energy gradients are not yet implemented in the SA-REKS formalism, we did not attempt to optimize a minimal energy CI (MECI) point [2]. using SA-REKS [3]. However, population transfer from the excited S_1 state to the ground S_0 state occurs via a funnel in which the whole manifold of CI points plays an important role, especially the CIs closest to the Franck-Condon point. [17, 187] The CI point identified in the S_0–S_1 PESs scan indicates that to reach this funnel a simultaneous twist about the double bond and a substantial pyramidalization of the C_9 atom are

covalent doubly excited state in the avoided crossing region.

[2] Although the analytic energy gradients for the excited state are not yet available in the SA-REKS implementation, this does not affect the results of the molecular dynamics simulations carried out in this work with the use of the OPLS molecular force field for which the analytic energy gradients are easily available.

[3] The optimization of MECI points and seams using OM2/GUGA-CI method [73] is discussed in the Chapter 8

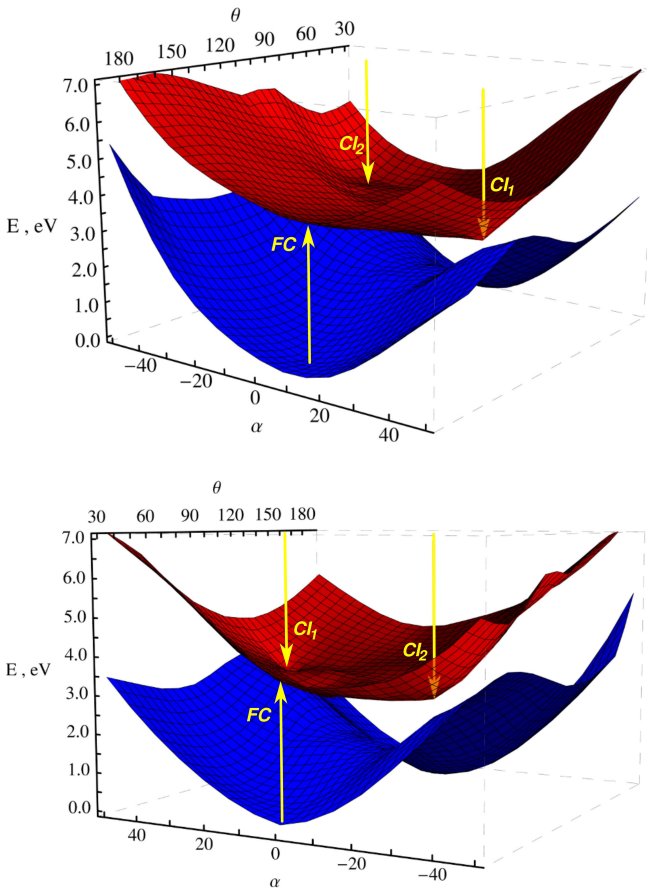

Figure 6.6: *Profiles of the S_0 (blue) and S_1 (red) PESs of* ***1*** *obtained in SA-REBH&HLYP/6-31G* calculations (see text for details). Left panel: view from the side of the* ***1-P*** *conformation. Lower panel: view from the side of the* ***1-M*** *conformation. Positions of the Franck-Condon points and conical intersections are shown with yellow arrows.*

necessary. This is consistent with the results obtained for simple alkenes, such as ethylene or butadiene,[17, 185, 187] and for stilbene [185]. Note that the pyramidalization angle of the atom C_9 (*i.e.* the angle between the C_9–C_{8a}–C_{9a} plane and the C_9–$C_{1'}$ bond) obtained for the CI point of **1** is 52.7° which is close to the pyramidalization angle of 58.8° obtained by Levine *et al.*[187] in the CASPT2 calculations on ethylene.

The CI point at $\alpha = 34°$ and $\theta = 120°$ lies *ca.* 3 eV above the ground state energy of the **1-P** conformer and *ca.* 0.7 eV below the Franck-Condon point. As can be seen in 6.6, this CI has peaked topography which implies that reaching the crossing seam on the S_1 surface should proceed without delays. [17] This observation is consistent with the results of the ultra-fast transient absorption study of molecular motors by Augulis *et al.*[190] who found that on average the molecule spends *ca.* 1.7 ps in the excited state. Note that the CI point corresponds to a local minimum on the S_1 PES that can be reached easily from the Franck-Condon region (near the **1-P** geometry). Thus the decay to the ground state occurs as an essentially barrierless process[17] which is consistent with the short excited state decay time observed experimentally.

In addition to the CI point at $\alpha = 34°$ and $\theta = 120°$ (CI_1) the onset of another CI point was observed at $\alpha = -28°$ and $\theta = 64°$ (CI_2). Indeed, if in a molecule with reflection symmetry, such as ethylene, there would be two CI points on opposite sides of the avoided crossing region and related by mirror symmetry. In a chiral molecule, such as the fluorene motor **1**, the two CI points can not be precise mirror images of one another, however both occur on opposite sides of the avoided crossing region. In our calculations, the CI_2 structure could not be precisely located on the grid chosen for the PES scans; the energy gap at $\alpha = -28°$ and $\theta = 64°$ is 0.16 eV and this structure lies *ca.* 0.5 eV lower in energy than the nearest Franck-Condon point (**1-M** conformer). Although the CI_2 structure can in principle be reached upon excitation from both conformers, the molecular dynamics simulations described in the subsequent section reveal that the majority of the trajectories on the S_1 PES started in the **1-P** conformer pass near the CI_1 structure, whereas the CI_2 point plays a minor role in the dynamics of the motor. Therefore, CI_1 can be considered as a more important mechanistic feature in the **1-P** $\rightarrow$ **1-M** photoisomerization and in the following is referred to as **1-CI** for brevity.

Using the results of our calculations the full operation cycle of the fluorene motor **1** can be presented as shown in 6.7. The initial structure **1-P** undergoes photo excitation to the S_1 state upon which it relaxes via the conical intersection **1-CI** to the ground S_0 state. On the ground state PES, it undergoes rapid barrierless relaxation to the **1-M** conformer which then undergoes a thermal helix inversion step passing through the **1-TS** transition state ($\Delta^{\ddagger}E = 18.7$ kcal/mol). After that, the system arrives at the **1-P'** structure, which is the **1-P** conformer rotated through 180° about a line passing through the central double bond, and the system repeats the above steps starting from the **1-P'** conformer. This completes the full rotation cycle of the fluorene motor **1**. Of note, in a recent combined experimental and theoretical study on a molecular switch structurally close to **1** a barrierless excited state reaction path leading to conical intersections was found by Sinicropi *et al.* [202] and Rivado-Casas *et al.* [203]

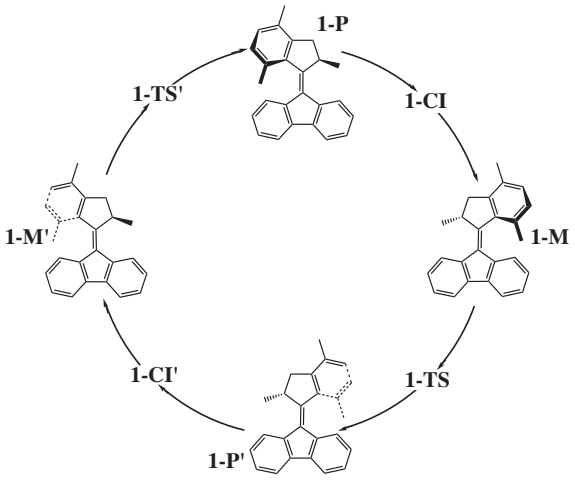

Figure 6.7: *Full rotation cycle of fluorene motor **1**.*

The molecular geometries of the **1-P**, **1-CI**, **1-M**, and **1-TS** structures are shown in 6.8. It can be seen that en route to the **1-M** conformer, **1** undergoes strong pyramidalization of the C_9 atom (in the **1-CI** structure) which results in a substantial tilt of the rotating part of the molecule from the axis of rotation (the C_9–$C_{1'}$ double bond). Somewhat less of a deviation from the rotation axis occurs during the helix inversion step, where pyramidalization of both C_9 and $C_{1'}$ atoms occurs in the **1-TS** structure. Note however, that, in **1-TS**, the upper part of the molecule tilts to the opposite side of the molecule than occurs during the photo-isomerization step. Thus, during the first half cycle in 6.7, the rotating part of the motor **1** carries out a combined tilt–twist motion which resembles motion of a butterfly wing rather than a pure rotation.

These results also help to understand the dynamics of relaxation from the **1-CI** structure to the **1-M** conformer which proceeds on the ground state PES. Because there is a substantial difference in the tilting angle of the rotor in these structures, a noticeable excitation of the respective vibrational modes of **1-M** can be expected (these modes have frequencies of *ca.* 400 cm^{-1} according to the calculations). Vibrational cooling of the **1-M** is expected to occur within characteristic times of the order of 10–20 ps[204] which is consistent with the experimental observations of Augulis *et al.* [190]

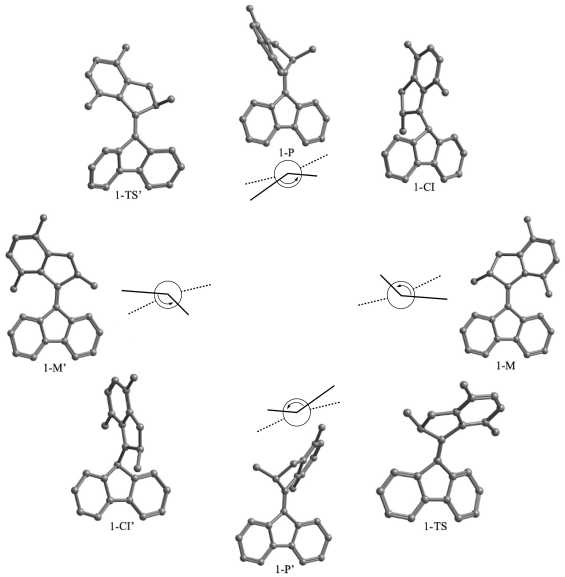

Figure 6.8: *Geometries of the most important structures involved in the rotation cycle of fluorene motor* ***1*** *as obtained from our quantum chemical calculations. Hydrogen atoms were removed for clarity.*

6.3.3 Molecular Dynamics Simulations

In the preceding section, the study of the S_0 and S_1 PESs was carried out for static molecular structures. It reveals a number of key features of the potential energy landscapes. The question remains however as to how important dynamic effects are for the photoisomerization? Can the quantum yields of photoisomerization when starting from the **1-P** or from the **1-M** conformer be understood? Hence, are we able to explain the photostationary state (PSS) observed experimentally? To address these questions and to obtain a more realistic theoretical description of light driven molecular motion we carried out molecular dynamics (MD) simulations based on the PESs of the ground and excited states obtained.

Excited state MD simulations[205] employing an on-the-fly quantum-chemical description of the PESs involved have been applied recently to a range of molecules, such as chromophores of photoreceptor proteins,[206–210] rhodopsin,[211–215] and fluorescent proteins,[216–218] as well as to DNA bases. [197, 219–223] In these studies, wavefunction-based quantum-chemical methods, such as CASSCF and CASPT2, as well as density functional methods and semi-empirical methods specifically adapted

to describe avoided crossings, conical intersections and bond breaking processes in molecules were used. In a recent study of a first-generation molecular rotor,[224] a density functional method not suited for the description of bond breaking processes and avoided crossing regions was employed. In the vast majority of the cases, the large computational cost of the quantum-chemical calculations limited the accessible time and length scales of simulations, rendering it impossible to obtain a statistically significant number of trajectories. In the present case, the size of the molecular motor **1** prohibits a straightforward application of quantum-chemical methods to study the excited state dynamics. Thus, we resorted to the OPLS all-atom force field[195] as an efficient alternative, enabling us to run a large number of independent simulations. As detailed below, the statistics provided by this approach allows different possible photochemical reaction pathways to be distinguished.

The OPLS all-atom force field was parametrized against the S_0 and S_1 potential energy surfaces obtained from our SA-REKS calculations, with a particular focus on the important torsion θ and pyramidalization α coordinates in setting up the MD simulations (for details, see Supporting Information). The mean absolute errors of the S_0 and S_1 surfaces with respect to those obtained from our REKS calculations are in the order of 0.2 eV (4.6 kcal/mol), which is acceptable for our purposes. Furthermore, the OPLS and REKS surfaces (for the details the reader is referred to the Supporting Information to Ref. [225]) exhibit the same qualitative features: a barrierless rotation about the C_9–$C_{1'}$ bond (dihedral angle θ) and a minimum at non-zero pyramidalization (dihedral angle α) in the excited S_1 state, and a large energy barrier to C_9–$C_{1'}$ double bond rotation of *ca.* 37 kcal/mol in the ground S_0 state.

In the MD simulations, 100 trajectories were initiated from both the **1-P** conformer and the **1-M** conformer, respectively. The S_1 trajectories were initiated from snapshots taken from equilibrated ground state simulations. At time $t = 0$, the molecule is excited vertically to the S_1 state where it evolves freely until it reaches a region where surface hopping occurs. After the surface hop back to the ground S_0 state, the molecule relaxes towards one of the conformers, **1-P** or **1-M**. According to the Landau-Zener formula,[226] the probability of the surface hop, P_{hop}, depends exponentially on the magnitude of the energy gap ΔE between the PESs, $P_{hop} = \exp\left[-\frac{\pi \Delta E}{4\hbar D}\right]$ (D is the non-adiabatic coupling between the two states). Thus P_{hop} reaches a maximum at or near the CI seams ($\Delta E = 0$). Here we adopted an assumption that surface hopping occurs exclusively at the CI. [197] The root mean square deviation (RMSD) of the coordinates of heavy atoms from the CI structures obtained in the SA-REBH&HLYP calculations was used as a criterion of proximity to the CI. As soon as the heavy-atom RMSD dropped below a threshold of 0.32 Å during the S_1 dynamics, a surface hop back to S_0 was imposed (see theoretical

methods section).

Table 6.3 summarizes the results of the MD simulations. All excited state trajectories sample structural regions close to CI_1 (with $\alpha = 34°$ and $\theta = 120°$) or CI_2 (with $\alpha = -28°$ and $\theta = 64°$), and ultimately successfully hop to the ground state. In each trajectory, the time spent on S_1 was taken as the excited state lifetime. The individual S_1 lifetimes range from 0.66 ps to 6.31 ps and 0.17 ps to 5.92 ps in the simulations initiated in the **1-P** and **1-M** conformer, respectively. Fitting a single-exponential decay to the lifetimes observed in the simulations initiated in the **1-P** conformation yielded a respective ensemble decay time[227] $\tau_{S_1} = 1.40 \pm 0.10$ ps. Closer analysis of the lifetime distributions revealed that the simulations initiated in the **1-M** conformer follow a bi-exponential decay: In 15 out of 100 simulations, an excited state lifetime below 0.24 ps is observed (with an ensemble decay time of $\tau_{S_1} = 0.20 \pm 0.01$ ps), whereas the remaining 85 simulations exhibit a significantly slower S_1 decay, with $\tau_{S_1} = 1.77 \pm 0.13$ ps. These lifetimes agree with the excited state decay time of about 1.7 ps measured for a similar molecular motor[190].

Table 6.3: *Excited state decay times τ_{S_1} and quantum yields ϕ_{iso} of photoisomerization obtained from MD simulations. 100 simulations were initiated from the **1-P** and **1-M** conformation, respectively.*

	1-P conformer	**1-M** conformer
τ_{S_1} (ps)	1.40 ± 0.10	1.77 ± 0.13
ϕ_{iso} (%)	92	40
SH[a] at CI_1 (%)	63	49
SH at CI_2 (%)	37	51
ϕ_{iso,CI_1} [b] (%)	98	37
ϕ_{iso,CI_2} (%)	81	43

[a] SH: surface hop; [b] Quantum yield of photoisomerization at the respective CI point.

The quantum yields for the photoisomerizations initiated in the **1-P** and **1-M** conformers, respectively, are quite different (6.3): Whereas $\phi_{P\rightarrow M}$ is as large as 92%, the $\phi_{M\rightarrow P}$ is only 40%. Interestingly, all 15 simulations with an S_1 lifetime <0.24 ps successfully isomerize and thus significantly contribute to $\phi_{M\rightarrow P}$. Taken together, the ratio $\phi_{P\rightarrow M}/\phi_{M\rightarrow P}$ is *ca.* 2.3 : 1, which needs to be corrected for the ratio of

optical absorption cross sections of both conformers to obtain the photostationary state ratio. At $\lambda = 365$ nm, the observed ratio of molar absorptivites of the **1-P** to **1-M** conformers is *ca.* 1.5 : 1. [62] Hence, the theoretical estimate for PSS is *ca.* 3.5 : 1, in excellent agreement with the experimental value of *ca.* 3 : 1. [62]

Next, we analyzed whether a certain part of the S_1/S_0 intersection seam is predominantly accessed, and if so, whether the vicinity of CI_1 or CI_2 is preferred. Indeed, as shown in 6.3, S_1 decay predominantly occurs at CI_1, when starting from the **1-P** conformation. From the 100 simulations initiated in the **1-P** conformer, 63 decay at CI_1, and only 37 at CI_2. This behavior might have been expected due to the proximity of CI_1 to the Franck-Condon region of **1-P** (see 6.6). For the trajectories initiated in the **1-M** conformer, the surface hop at CI_1 occurs at about the same frequency as at CI_2, despite that CI_1 is farther away from the **1-M** Franck-Condon region than CI_2. This result underlines the importance of the dynamics in the excited state process. In this context, it is crucial to run many independent simulations (here: 100) to be able to distinguish between different possible photochemical reaction pathways. Finally, we separately analyzed the isomerization quantum yields in the vicinity of the two CI structures. The analysis shows that the high $\phi_{P\rightarrow M}$ is due to a very high isomerization quantum yield of 98% at CI_1. Likewise, the lower value of $\phi_{M\rightarrow P}$ is also determined by the isomerization quantum yield at CI_1, which in this case is only 37%.

Table 6.9 shows the time evolution of the twist and pyramidalization angle (θ and α, respectively) along a representative MD trajectory. The dynamics can be separated into three phases: (i) evolution on the ground state S_0, (ii) excitation and evolution on the excited state S_1, and (iii) decay back to S_0 at the CI and subsequent relaxation on the ground state surface. Within ca. 1 ps after excitation to S_1, rapid rotation about the C_9–$C_{1'}$ double bond (dihedral angle θ) occurs. However, this motion does not immediately lead to a surface hop, since the vibrational period of the pyramidalization motion (dihedral angle α) is faster: α adopted a value of about $+30°$ already at around 0.4 ps, a time at which the rotor part of the molecule did not yet reach a fully perpendicular orientation with respect to the stator part due to its inertia. The CI seam is then accessed upon the second vibrational motion of the pyramidalization angle towards $+30°$, which occurs after about 1.3 ps (see inset in 6.9). Subsequently, the molecule isomerizes to the M-conformation, a motion that is already completed after 1.6 ps. The final relaxation in the S_0 M-minimum is accompanied by a damped pyramidalization motion.

Taken together, the MD simulations provide a detailed picture of the structural dynamics that governs the photo conversion processes, and support the conclusions based on the study of the topology of the ground and excited state PESs of **1**. The characteristic lifetimes of the excited state and the ratio of quantum yields of the two

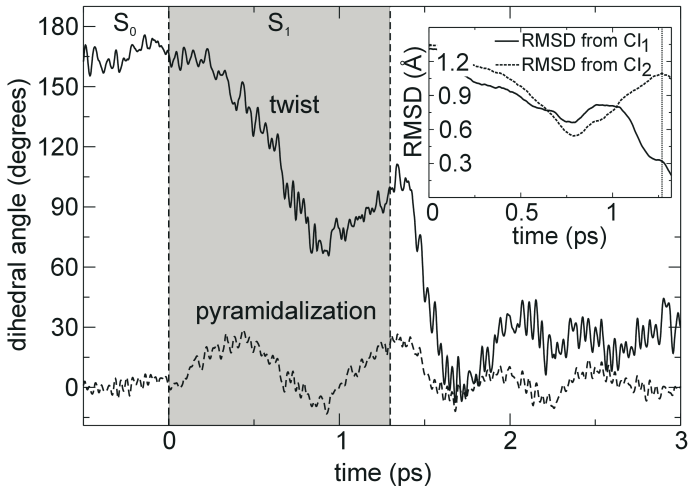

Figure 6.9: *Time evolution of twist θ (solid line) and pyramidalization α (dashed line) during P-to-M photoisomerization trajectory. The grey-shaded area indicates evolution in the excited state S_1. The inset shows the heavy-atom RMSD from the CI_1 and CI_2 geometries during system evolution in the excited state; the surface hop is indicated by a dashed line (see text for detail).*

possible photoisomerizations (the photostationary state) nicely match and explain the experimentally observed data [62, 190], confirming the validity of the undertaken analysis of the photoisomerization mechanism.

6.4 Conclusions

In this Chapter, the results of a combined quantum chemical and molecular dynamics study of the mechanism of the photoisomerization step of the rotational cycle of fluorene based molecular rotary motor **1** [62] are presented. Uni-directional rotation in this motor is achieved due to the periodic repetition of photoisomerization and thermal relaxation steps. A high degree of control over the thermally activated helix inversion step was achieved which led to the formulation of clear design principles for the thermal step in molecular rotary motors based on overcrowded alkenes [60–62]. Hitherto, the photoisomerization step remained poorly understood and less subject to rational design based on a firm understanding of the underlying principles.

The analysis of the ground and lowest singlet excited state potential energy sur-

faces obtained in quantum chemical calculations suggests that conical intersections [17, 183, 184] play a central role in the mechanism of photo conversion between the stable **1-P** conformer and the metastable **1-M** conformer. Although, in this study, we focus on the zwitterionic singlet excited state [4] the obtained results provide ample evidence that the photoisomerization of **1** occurs via a mechanism similar to ethylene and stilbene. [17, 185, 187] Low energy points on the CI seam are reached through a combined twist–pyramidalization motion of the rotor part of **1**, thus leading to a substantial tilt of the rotor from the axis of rotation. Molecular dynamics simulations carried out for both possible photoisomerization reactions, **1-P** $\rightarrow$ **1-M** and **1-M** $\rightarrow$ **1-P**, predict different quantum yields of isomerization, $\phi_{\mathrm{P}\rightarrow\mathrm{M}} = 0.92$ and $\phi_{\mathrm{M}\rightarrow\mathrm{P}} = 0.40$, which upon correction for the spectral overlap explain the occurrence of a photostationary state with the experimentally measured ratio of *ca.* 3:1 of the concentrations of the metastable and stable conformers [62]. Because conical intersections govern the photostationary state, rational synthetic design of the photoisomerization step should be directed towards controlling the regions where CIs occur. In this respect, theoretical study of the factors dominating the electronic structure in the CI seams and avoided crossing regions can provide a crucial piece of information complementing experimental studies. For example, it is expected that flattening the rotor and the stator geometries (that is, making them less pyramidalized) at the CI points as a result of substitution/chemical modification may lead to a different dynamics and, as a consequence, to a different photostationary state.

Interestingly, molecular dynamics simulations of the excited state dynamics of **1** indicate that the excited states may show multi-modal decay patterns. Whereas for the **1-P** $\rightarrow$ **1-M** photoisomerization reaction a single-exponential decay with the average excited state lifetime of $\tau_{\mathrm{S}_1} = 1.40 \pm 0.10$ ps was found in the simulations, the reverse photoisomerization, **1-M** $\rightarrow$ **1-P**, shows a bi-exponential decay with the lifetimes of $\tau_{\mathrm{S}_1} = 0.20 \pm 0.01$ ps and $\tau_{\mathrm{S}_1} = 1.77 \pm 0.13$ ps. This observation offers an alternative explanation to the transient absorption experiments where different decay times were interpreted in terms of a multi-state model as resulting from transitions between several excited states [190, 200, 228]. Indeed, if, on the excited state surface, the system can follow several trajectories with distinct lifetimes, the interpretation of the experimentally observed multi-exponential decay times can be achieved in terms of two states only, the ground state and the lowest excited state. This conjecture should be verified experimentally in future studies where information provided by solvent effects and the effects of substitution on the observed photostationary state should be investigated.

[4] See the footnote on page 6.3.2

Chapter 7

Conical Intersections and Nonadiabatic coupling

7.1 Introduction

The Born-Oppenheimer approximation implied in many quantum chemical descriptions of photochemical reactions is strictly applicable when the coupling between the nuclear and electronic wave functions is negligible. The measure of the coupling in the adiabatic representation, i.e. when the potential energy operator for nuclei is diagonal, is the momentum coupling between adiabatic states (eigenstates of the BO Hamiltonian) referred to as the nonadiabatic coupling (NAC)[1] The NAC elements are not negligible in the regions of avoided crossings and at conical intersections they tend to infinity. As the probability of transition is exponentially dependent on the NAC through the Landau-Zener formula, the transitions near conical intersections are highly efficient. Therefore for the study of photoisomerization processes, proceeding via nonradiative decay, the knowledge about NAC elements and conical intersections is vital. The efficiency of a reaction can be assessed by the study of reaction paths passing via conical intersection points and seams. Consequently, it is necessary to be able to localize the conical intersection geometries.

In the section 7.1 we briefly write main expressions for the NAC elements. After the introduction of NAC elements we discuss the NAC vectors and gradient difference vectors, where we follow closely the derivation by Lengsfield and Yarkony [229]. The NAC vectors are different albeit akin to the NAC elements. The former together with the gradient difference vector represent the basis of the branching space, i.e. structural deformations of a molecule along these vectors lift the degeneracy thus leading to/away from the conical intersection.

The explanations of NAC matrices and vectors are followed by considering main points of conical intersection geometry optimization, which will be addressed in the section 7.3 where the results of optimizations of MECI geometries in model systems will be discussed. In the chapter 8 we will discuss the study of reaction paths and con-

[1] We neglect in current discussion the second order nonadiabatic coupling matrix element which is known to be sufficiently small in most of the cases.

ical intersection seams in the fluorene-based molecular motor using the OM2/MRCI approach [181] where we will refer to the basic notions explained in this chapter.

In the final section 7.4 of this chapter we present a study of NAC elements of ethylene using CASSCF, CASPT2 and SA-REKS methods.

7.2 General theory

We begin with a sketchy discussion of a generalization of the Born-Oppenheimer (BO) approximation that explicitly includes the couplings between BO surfaces. The Schrödinger equation is given by

$$i\hbar\frac{\partial\Psi}{\partial t} = \hat{H}\Psi, \tag{7.1}$$

where $\hat{H}$ is the molecular Hamiltonian and Ψ the wave function. The Hamiltonian can in general be partitioned into the nuclear kinetic energy $\hat{T}_n$ and the electronic Hamiltonian $\hat{H}_{el}$ as

$$\hat{H}(\mathbf{R},\mathbf{r}) = \hat{T}_n(\mathbf{R}) + \hat{H}_{el}(\mathbf{R},\mathbf{r}), \tag{7.2}$$

with

$$\hat{H}_{el}(\mathbf{R},\mathbf{r}) = \hat{T}_e(\mathbf{r}) + U(\mathbf{R},\mathbf{r}) \tag{7.3}$$

where the kinetic energy operators are given by

$$\hat{T}_n(\mathbf{R}) = -\sum_j \frac{\nabla^2_{R_j}}{2M_j}, \quad \hat{T}_e(\mathbf{r}) = -\sum_i \frac{\nabla^2_{r_i}}{2} \tag{7.4}$$

Assuming clumped nuclei $\hat{T}_n(\mathbf{R}) = 0$, the Schr̈odinger equation (SE) (7.1) can be rewritten

$$\hat{H}_{el}\Phi_i(\mathbf{r};\mathbf{R}) = V_i(\mathbf{R})\Phi_i(\mathbf{r};\mathbf{R}), \tag{7.5}$$

where semicolon indicates the parametric dependence. Suppose the solutions $\Phi_i(\mathbf{r};\mathbf{R})$ to the time-independent electronic SE (7.11) are known and form a complete and orthonormal set. The total wave function Ψ can then be expanded in the basis of the electronic wave functions

$$\Psi(\mathbf{R},\mathbf{r}) = \sum_j \chi_j(\mathbf{R})\Phi_j(\mathbf{r};\mathbf{R}), \tag{7.6}$$

where expansion coefficients $\chi_j(\mathbf{R})$ are the nuclear wavefunctions. This representation is called Born-Huang expansion. Substituting equation (7.6) into the SE (7.1)

and projecting on a particular electronic wave function Φ_i one obtains a set of differential equations

$$[\hat{T}_n + V_i]\chi_i - \sum_j \hat{\Lambda}_{ij}\chi_j = i\frac{\partial \chi_i}{\partial t}, \tag{7.7}$$

where $\hat{\Lambda}_{ij}$ are the nonadiabatic coupling operators given by

$$\hat{\Lambda}_{ij} = \frac{1}{2M}\left(2\langle\Phi_i|\hat{\boldsymbol{\nabla}}|\Phi_j\rangle \cdot \hat{\boldsymbol{\nabla}} + \langle\Phi_i|\hat{\nabla}^2|\Phi_j\rangle\right). \tag{7.8}$$

The second term on the right hand side of the expression (7.8) contains a matrix element $\hat{\nabla}^2_{ij}$ which has been shown to be negligibly small in many situations. [230] However, the matrix element

$$\hat{\boldsymbol{\nabla}}_{ij} = \langle\Phi_i|\hat{\boldsymbol{\nabla}}|\Phi_j\rangle \tag{7.9}$$

the so-called nonadiabatic coupling (NAC) matrix element in certain situations can have substantial values. In such a case the electronic and nuclear motions cannot be considered independent. It is instructive to evaluate the behavior of $\boldsymbol{\nabla}_{ij}$ on an explicit example of an electronic wavefunction in a multireference theory, where the wavefunction is expanded in terms of configuration state functions (CSF) Θ_λ as

$$\Psi_i(\mathbf{r};\mathbf{R}) = \sum_\lambda C^i_\lambda(\mathbf{R})\Theta_\lambda(\mathbf{r};\mathbf{R}), \tag{7.10}$$

where $C_\lambda(\mathbf{R})$ are the configuration interaction (CI[2]) coefficients. Substituting (7.10) into the electronic Schrödinger equation

$$\hat{H}^{el}(\mathbf{r};\mathbf{R})\Psi_i(\mathbf{r};\mathbf{R}) = E^e_i(\mathbf{R})\Psi_i(\mathbf{r};\mathbf{R}), \tag{7.11}$$

yields the matrix CI equation

$$\mathbf{H}\mathbf{C}^i(\mathbf{R}) = E_i(\mathbf{R})\mathbf{C}^i(\mathbf{R}), \tag{7.12}$$

Differentiation of the wavefunction (7.10) with respect to nuclear degrees of freedom gives

$$\frac{\partial}{\partial R_\alpha}\Psi_i(\mathbf{r};\mathbf{R}) = \sum_\lambda C^i_\lambda\left[\left(\frac{\partial}{\partial R_\alpha}C^i_\lambda(\mathbf{R})\right)\Theta_\lambda(\mathbf{r};\mathbf{R}) + C^i_\lambda(\mathbf{R})\left(\frac{\partial}{\partial R_\alpha}\Theta_\lambda(\mathbf{r};\mathbf{R})\right)\right] \tag{7.13}$$

[2]The acronym CI is the same for the configuration interaction and conical intersection. The meaning depends on the context. It is hoped that this will not lead to a confusion.

thus the matrix element $\boldsymbol{\nabla}_{ij}$ consists of two terms

$$\boldsymbol{\nabla}^{\alpha}_{ij}(\mathbf{R}) = {}^{CI}\boldsymbol{\nabla}^{\alpha}_{ij}(\mathbf{R}) + {}^{CSF}\boldsymbol{\nabla}^{\alpha}_{ij}(\mathbf{R}), \tag{7.14}$$

with ${}^{CI}\boldsymbol{\nabla}^{\alpha}_{ij}(\mathbf{R})$ given by

$${}^{CI}\boldsymbol{\nabla}^{\alpha}_{ji}(\mathbf{R}) = \sum_{\lambda} C^{j}_{\lambda}(\mathbf{R}) \frac{\partial}{\partial \mathbf{R}_{\alpha}} C^{i}_{\lambda}(\mathbf{R}) \tag{7.15}$$

and the CSF part expressed as

$${}^{CSF}\boldsymbol{\nabla}^{\alpha}_{ji}(\mathbf{R}) = \sum_{\lambda,\mu} C^{j}_{\lambda}(\mathbf{R}) \int \Theta^{*}_{\lambda}(\mathbf{r};\mathbf{R}) \frac{\partial}{\partial \mathbf{R}_{\alpha}} \Theta_{\lambda}(\mathbf{r};\mathbf{R}) \mathbf{dr} C^{i}_{\mu}(\mathbf{R}) \tag{7.16}$$

The expression for ${}^{CI}\boldsymbol{\nabla}_{ji}$ can be rewritten in a more appropriate form by performing differentiation of (7.12) and subsequently taking the dot product with $\mathbf{C}_j(\mathbf{R})$ which gives

$${}^{CI}\boldsymbol{\nabla}^{\alpha}_{ji}(\mathbf{R}) = \mathbf{C}^{\dagger}_{j}(\mathbf{R}) \frac{\partial}{\partial \mathbf{R}_{\alpha}} \mathbf{C_i}(\mathbf{R}) = \frac{\mathbf{C}^{\dagger}_{\mathbf{j}}(\mathbf{R}) \frac{\partial \mathbf{H}}{\partial \mathbf{R}_{\alpha}} \mathbf{C_i}(\mathbf{R})}{\mathbf{E_j}(\mathbf{R}) - \mathbf{E_i}(\mathbf{R})} \tag{7.17}$$

whence it is clearly seen that in the proximity of a conical intersection ($E_j \to E_i$) the matrix element should tend to infinity. It has been shown that the CI contribution (7.17) outweighs the CSF term (7.16) when the energy gap is small.

The numerator in (7.17) is termed the NAC vector $\mathbf{h}^{\alpha}_{ij}$. The NAC vector $\mathbf{h}^{\alpha}_{ij}$

$$\mathbf{h}^{\alpha}_{ij} = \mathbf{C}^{\dagger}_{\mathbf{j}}(\mathbf{R}) \frac{\partial \mathbf{H}}{\partial \mathbf{R}_{\alpha}} \mathbf{C_i}(\mathbf{R}) \tag{7.18}$$

together with the gradient difference vector (which is derived in analogous way) given by

$$\mathbf{g}^{\alpha}_{ij} = \mathbf{C}^{\dagger}_{i}(\mathbf{R}) \frac{\partial \mathbf{H}}{\partial \mathbf{R}_{\alpha}} \mathbf{C_i}(\mathbf{R}) - \mathbf{C}^{\dagger}_{\mathbf{j}}(\mathbf{R}) \frac{\partial \mathbf{H}}{\partial \mathbf{R}_{\alpha}} \mathbf{C_j}(\mathbf{R}), \tag{7.19}$$

comprise the branching plane, in which the degeneracy between the electronic states i and j is lifted linearly. Therefore the knowledge of the vectors may significantly facilitate the localization of conical intersections and seams.

To proceed we need to mention two main techniques of MECI geometry optimization, which will be addressed in section 7.3 and chapter 8.

The requirement of the optimized function to be smooth is more difficult to satisfy when searching a conical intersection, because the PES near at intersections is per se discontinuous. To overcome the problem additional constraints are imposed either via

the NAC and gradient difference vectors or by the penalty function. The techniques based on the penalty function (PF) [187], do not require the knowledge of the **g** and **h** vectors. In this method the geometry optimization is performed by minimizing the expression

$$F(\mathbf{R}) = \bar{E} + c_1 \frac{\Delta E^2}{\Delta E + c_2}, \tag{7.20}$$

where the first term minimizes the average of the energies

$$\bar{E} = \frac{E_i + E_j}{2} \tag{7.21}$$

whereas the second term, referred to as the penalty function, minimizes the energy difference.

$$\Delta E = E_j - E_i \tag{7.22}$$

The coefficient c_1 determines the weight of the energy difference, while the coefficient c_2 controls the slope in the proximity of the seam. In this method a true degeneracy can only be approached if $c_1 \to \infty$, while large enough c_1 may lead to optimization failures. Therefore the approach must be applied with care and used in cases when the gradients **h** and **g** are not available.

Another method called Lagrange-Newton method (L-N) localizes the minimum energy CI point or seam by minimizing the Lagrangian

$$\mathbf{L_{ij}}(\mathbf{R}, \xi, \lambda_i) = \frac{E_i + E_j}{2} + \xi_1(E_i - E_j) + \xi_2 H_{ij} + \sum_{i=1}^{M} \lambda_i \mathbf{K_i}, \tag{7.23}$$

where the first and second terms minimize the average and the difference of energies, respectively, the third term imposes the constraint $\mathbf{H_{ij}} \equiv \mathbf{C}^\dagger \mathbf{H} \mathbf{C_j} = 0$, and the last term imposes constraints on particular internal coordinates λ_i. [181] The gradient of the Lagrangian (7.23) is given by

$$\nabla \mathbf{L_{ij}} = \frac{\mathbf{g_i} + \mathbf{g_j}}{2} + \xi_1 \mathbf{g_{ij}} + \xi_2 \mathbf{h_{ij}} + \sum_{i=1}^{M} \lambda_i \mathbf{K_i}. \tag{7.24}$$

7.3 MECI geometries of model systems

In this section we present the results of the $S_0 - S_1$ MECI geometry optimizations using SA-REKS method to determine the corresponding PESs. The analytic NAC vectors $\mathbf{h_{ij}}$ and gradient difference vectors $\mathbf{g_{ij}}$ are not yet implemented in the SA-REKS method, therefore we resort to the PF method, discussed above, to optimize MECI geometries for the selected model systems. The results are compared with the geometries obtained by SA-CASSCF (CAS for brevity), MS-CASPT2 (CASPT2), MRCI and MNDO/MRCI methods found in references[26, 187, 231].

The lowest valence excited singlet state (S_1) of olefines such as ethylene and stilbene, etc. is stabilized upon twist about the C=C bond. At ca. 90° of twist the systems possess a minimum on the S_1 state curve. However, the S_0/S_1 energy gap may amount to several eV and a CI may only be reached by additional deformations, such as pyramidalization.

Ethylene is a well known example of a strongly pyramidalized conical intersection geometry. [18, 137] It has been shown [49, 231] that due to the peaked topology of the conical intersection, the pyramidalized ethylene is expected to be the most efficient channel of nonradiative decay, hence it represents dynamically the most favorable MECI structure.

The pyramidalization angle is defined as $\alpha = 180° - \zeta$, where ζ is the angle between the tilted CH_2 plane and the C-C bond attached to it. Freund and Klessinger [232] pointed out that the minimum energy S_0/S_1 intersection corresponds to a twisted/pyramidalized structure of C_1 rather than C_s symmetry, i.e. the CH bonds of the kinked methylene are not equal and constitute different angles with the C-C bond.

We carried out optimization of the MECI geometries of ethylene, stilbene, methaniminium $CH_2NH_2^+$ and protonated Schiff base (PSB $C_6H_6NH_2^+$ using SA-REKS method with BH&HLYP density functional and 6-31G** basis set. The optimization was performed with the help of the CIOpt program. [233]

Ethylene and stilbene have analogous electronic structures and represent simplest variants of photoswitches. The molecules feature similar twisted-pyramidalized structures. [37] The results of calculations are summarized in the tables 7.1 and 7.2. For comparison we show the results of Levine et al. [187] and Barbatti et al. [231]. The MECI structures are depicted in Fig. 7.1.

The ethylene MECI structure obtained with the SA-REKS method features the correct C-C bondlength and twist angle, however the pyramidalization angle α slightly deviates from the results of Levine et al. [187] It should be noted, though that in our calculations we performed only one optimization cycle with c_1 coefficient (7.20) not updated. This certainly must have resulted in a lower accuracy of the MECI op-

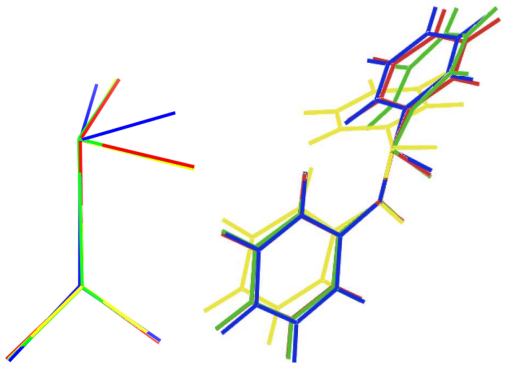

Figure 7.1: *Ethylene (left) and stilbene (right) S_0/S_1 MECI structures. The MECIs from different calculations are superimposed. The following color code was used, ethylene: SA-REKS - blue; CAS[a] - yellow, CASPT2[a] - red, MRCI[a] - green; stilbene: SA-REKS - blue, CAS(2,2)[a] - yellow, CAS(14,12)[a] - green, CASPT2[a] - red.*
[a)] *From Ref. [187]*

Table 7.1: *Twisted-pyramidalized ethylene S_0/S_1 MECI geometries calculated at SA-REKS/BH&HLYP/6-31G** level compared with the results from Ref [187].*

	CH_1	CH_2	C-C	Twist	α
CAS[a]	1.17	1.08	1.386	73.3	57.6
CASPT2[a]	1.17	1.09	1.410	72.5	58.4
MRCI[a]	1.17	1.09	1.399	73.3	58.8
MRCI[b]	1.16	1.10	1.399	-	75.6
SAREKS	1.11	1.09	1.388	73.7	52.3

[a)] From Ref. [187]
[b)] From Ref. [231]

timization. Also, the CI seam along α mode seems to be shallow. This can be seen in the MRCI results by Barbatti and co-workers [231] who found $\alpha = 75.6°$, whereas the other parameters agree well with the MRCI and CASPT2 results of Levine and co-authors [187]. The shallowness of the seam along α in stilbene was pointed out by Levine et al. who found α in CAS(2,2) calculations deviating by ca. 25° from the CAS(14,12) and CASPT2 results (see Tab. 7.2). However, the MECI structures of stilbene obtained with the SA-REKS method agree well with the CASPT2 data.

It can be seen that the twisting and pyramidalization angles are similar to those of ethylene, which is to be anticipated as the structures possess similar π systems.

Table 7.2: *Stilbene S_0/S_1 MECI structures calculated at SA-REKS/BH&HLYP/6-31G** level compared with the results from Ref [187].*

	C-C	CH1	CH2	C-H	Twist	α	β_1	β_2	β_3
CAS(2,2)	1.49	1.08	1.11	2.06	102	75	114	103	98
CAS(14,12)	1.41	1.09	1.20	1.56	-	51	113	73	105
CASPT2	1.38	1.10	1.16	1.57	78	53	111	76	108
SAREKS	1.39	1.09	1.13	1.67	79	52	114	82	109

[a] From Ref. [187]

In neutral olefins to reach the CI additional deformations other than twist are needed to induce the dipole moment. [137, 234] This is achieved by charge destabilization by, e.g. substantial kink of CH_2 group. In contrast, a pure twist in polar olefins, such as, e.g. methaniminium, is sufficient to reach a CI.

We carried out the MECI optimizations of methaniminium and the PSB molecules using SA-REKS and compare the structures with the MECI geometries found by Keal and co-workers [26] who employed the OM2/MRCI semiempirical configuration interaction method with closed shell RHF reference and fixed (6,6) active space (denoted here as RHF-AS6), open shell ROHF reference with an automatic active space (denoted as ROHF-AS+), and MS-MR-CASPT2(6,6)/6-31G* method (here CASPT2).

Table 7.3: *Methaniminium S_0/S_1 MECI geometries calculated at SA-REKS/BH&HLYP/6-31G** level compared with the results from Ref [187].*

	C-N	Twist	α_C	α_N
CAS[a]	1.389	135.0	0.0	0.0
CASPT2[a]	1.371	142.1	0.1	6.7
MRCI[a]	1.386	134.9	0.1	0.0
SAREKS	1.368	124.6	36.3	0.4

[a] From Ref. [187]

The MECI structures of methaniminium and PSB are presented in Tabs 7.3 and 7.4 and the corresponding structures are shown in Fig 7.2. From Tab. 7.3 it is seen

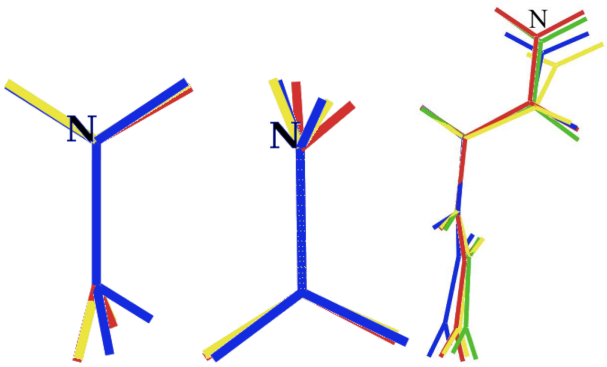

Figure 7.2: *Methaniminium $CH_2NH_2^+$ in two projections (left) and PSB $C_6H_6NH_2^+$ (right) S_0/S_1 MECI structures. The MECIs from different calculations are superimposed. The following coloring was used,*
methaniminium: SA-REKS - blue, CAS[a] - yellow, CASPT2[a] - red;
PSB: SA-REKS - blue, RHF-AS6[b] - yellow, ROHF-AS+[b] - green, CASPT2[b] - red. [a)] *From Ref. [187]*
[b)] *From Ref. [26]*

that the pyramidalization on both ends is small compared with ethylene. Although, the SA-REKS MECI structure possesses correct C-N bondlength and twisting angle, the CH_2 group is discernibly kinked. We attribute this discrepancy to the aforementioned flatness of the seam in the direction of tilt. The flatness of the seam is also apparent along the pyramidalization of the NH_2^+ group in the CASPT2 structure.

The comparison of different PSB MECI structures listed in Tab. 7.4 shows a qualitative agreement between the SA-REKS and CASPT2 MECI structures. The bond alternation pattern in SA-REKS MECI is similar to that of the CASPT2 and ROHF-AS+ methods. The torsional angle C=C-C-N is somewhat underestimated w.r.t. the corresponding CASPT2 value. This may reflect the aforementioned difficulties with the optimization using the penalty function method without analytic gradients. A similar pronounced deviation of the torsional angle is observed in the RHF-AS6 MECI structure. [26]

To summarize, in this preliminary study the MECI structures obtained with the help of the SA-REKS method are in a reasonable agreement with the respective structures found in the literature and obtained with highly-correlated methods. The discrepancy observed in ethylene and methaniminium is explained by the limitations of the numerical optimization method employed. The analytic gradients for the excited states and nonadiabatic coupling are not yet implemented in the SA-REKS

Table 7.4: *Protonated Schiff base S_0/S_1 MECI geometries calculated at SA-REKS/BH&HLYP/6-31G** level compared with the results of Keal and co-workers [26].*

	SA-REKS	CASPT2[a]	ROHF-AS+[a]	RHF-AS6[a]
C=C	1.352	1.387	1.389	1.379
C-C	1.408	1.398	1.404	1.413
C=C	1.444	1.464	1.441	1.412
C-C	1.448	1.402	1.437	1.486
C-N	1.284	1.329	1.304	1.287
C=C-C	127.3	122.8	118.9	121.3
C-C=C	118.8	123.0	120.3	120.4
C=C-C	119.8	122.0	118.6	116.3
C-C-N	122.2	122.3	119.7	120.8
C=C-C=C	-170.4	-178.6	-175.5	-177.0
C-C=C-C	-94.2	-92.0	-86.2	-90.6
C=C-C-N	155.8	179.8	178.7	141.7

[a] From Ref. [26]

method. Therefore we had recourse to the penalty function method. To facilitate the calculations we performed only one optimization cycle without updating the weighting coefficient c_1. As a consequence, the procedure was expected to be less accurate in the case of sufficiently shallow CI seam along the pyramidalization mode.

7.4 Nonadiabatic Coupling Matrix Elements

As we are concerned with the lowest excited states, here we attempt to assess the magnitudes of NACs between the ground and singly, and doubly excited states within SA-REKS formalism. In the minimal model of two-electrons in two-orbitals, the following configurations arise: $|a\bar{a}|, |a\bar{b}|, |b\bar{a}|$ and $|b\bar{b}|$ The singlet wavefunctions which cover both normal and diradicaloid situations can be expressed with the help of these

configurations as follows [18]

$$
\begin{aligned}
|S_0\rangle \equiv |1\rangle &= \sqrt{\frac{n_a}{2}}|a\bar{a}\rangle - \sqrt{\frac{n_b}{2}}|b\bar{b}\rangle \\
|S_1\rangle \equiv |2\rangle &= \frac{1}{\sqrt{2}}|a\bar{b}\rangle + \frac{1}{\sqrt{2}}|b\bar{a}\rangle \\
|S_2\rangle \equiv |3\rangle &= \sqrt{\frac{n_b}{2}}|a\bar{a}\rangle + \sqrt{\frac{n_a}{2}}|b\bar{b}\rangle,
\end{aligned}
\tag{7.25}
$$

where $|a\bar{a}\rangle$ are normalized Slater determinants, and n_a and n_b the fractional occupation numbers of the orbitals.

Consider now the matrix elements of $\frac{d}{dX_A}$ operator between the states (7.25), where X_A is the X-coordinate of the atom A

$$
\begin{aligned}
\langle 1|\frac{d}{dX_A}|2\rangle \quad &= \tfrac{\sqrt{n_a}}{2}\left(\langle a\bar{a}|\tfrac{d}{dX_A}|a\bar{b}\rangle + \langle a\bar{a}|\tfrac{d}{dX_A}|b\bar{a}\rangle\right) \\
&\quad -\tfrac{\sqrt{n_b}}{2}\left(\langle b\bar{b}|\tfrac{d}{dX_A}|a\bar{b}\rangle + \langle b\bar{b}|\tfrac{d}{dX_A}|b\bar{a}\rangle\right)
\end{aligned}
\tag{7.26}
$$

The operator $\frac{d}{dX_A}$ is a one-electron operator, hence one can rewrite the matrix elements entering (7.26)

$$
\langle a\bar{a}|\frac{d}{dX_A}|a\bar{b}\rangle = \langle a|\frac{d}{dX_A}|b\rangle \tag{7.27}
$$

due to orthonormality of spin-orbitals the matrix elements $\langle a|\hat{\nabla}|b\rangle$ are antisymmetric, thus we obtain

$$
\langle 1|\frac{d}{dX_A}|2\rangle = (\sqrt{n_a} + \sqrt{n_b})\,\langle a|\frac{d}{dX_A}|b\rangle \tag{7.28}
$$

The spin-orbitals can be expanded in terms of basis functions[3]

$$
a = \sum_{\mu} C_{\mu a}\phi_{\mu}; \quad b = \sum_{\nu} C_{\nu b}\phi_{\nu} \tag{7.29}
$$

so that

$$
\begin{aligned}
&\langle 1|\frac{d}{dX_A}|2\rangle \\
&\qquad = (\sqrt{n_a} + \sqrt{n_b}) \sum_{\mu\nu} \int C_{\mu a}\phi_{\mu}\left[\phi_{\nu}\frac{dC_{\nu b}}{dX_A} + C_{\nu b}\frac{d\phi_{\nu}}{dX_A}\right] dr,
\end{aligned}
\tag{7.30}
$$

[3]Throughout the present chapter we consider only real atomic and molecular orbitals.

here the integration is over the coordinates of electrons r. Defining $S_{\mu\nu} = \int \phi_\mu^* \phi_\nu dr$, we obtain

$$\langle 1|\frac{d}{dX_A}|2\rangle = (\sqrt{n_a} + \sqrt{n_b}) \sum_{\mu\nu} \left[C_{\mu a} S_{\mu\nu} \frac{dC_{\nu b}}{dX_A} + C_{\mu a} C_{\nu b} \langle \phi_\mu | \frac{d\phi_\nu}{dX_A} \rangle \right], \tag{7.31}$$

or in matrix form

$$\langle 1|\frac{d}{dX_A}|2\rangle = (\sqrt{n_a} + \sqrt{n_b}) \left[\mathbf{C_a^T S C'_b} + \mathbf{C_a^T \boldsymbol{\nabla} C_b} \right], \tag{7.32}$$

where $\boldsymbol{\nabla} \equiv \left| \langle \phi_\mu | \frac{d\phi_\nu}{dX_A} \rangle \right|$, and $\mathbf{C'_b} \equiv \left| \frac{dC_{\nu b}}{dX_A} \right|$.

If atom-centered basis functions are used, the following property holds $\frac{d\phi_\nu}{dX_A} = -\frac{d\phi_\nu}{dx}\big|_{\nu \in A}$, where x are electronic coordinates. Therefore, denoting

$$\nabla_{\mu\nu} \equiv \langle \phi_\mu | \frac{d}{dx} | \phi_\nu \rangle \tag{7.33}$$

and in matrix form $\boldsymbol{\nabla_e}$ we have

$$\langle 1|\frac{d}{dX_A}|2\rangle = (\sqrt{n_a} + \sqrt{n_b}) \left[\mathbf{C_a^T S C'_b} - \mathbf{C_a^T} \boldsymbol{\nabla}_e\big|_{\nu \in A} \mathbf{C_b} \right], \tag{7.34}$$

Differentiating the orthonormality condition of orbitals $\mathbf{C^T S C} = \mathbf{I}$ one finds

$$\mathbf{C'^T S C} + \mathbf{C^T S C'} = -\mathbf{C^T S' C}, \tag{7.35}$$

where primes denote a differentiation w.r.t. nuclear coordinates. An equation of the type

$$\mathbf{A}^\dagger \mathbf{B} + \mathbf{B}^\dagger \mathbf{A} = \mathbf{C}, \tag{7.36}$$

where $\mathbf{C}$ is a Hermitian matrix, has general solution

$$\mathbf{A} = \frac{1}{2} \left((\mathbf{B^{-1}})^\dagger \mathbf{C} + \mathbf{Z} \right), \tag{7.37}$$

where $\mathbf{Z}$ is an arbitrary antihermitian matrix. Therefore in our case a particular solution will be

$$\mathbf{C'} = -\frac{1}{2} \mathbf{S^{-1} S' C}, \tag{7.38}$$

specifically for a column we have

$$\mathbf{C'_b} = -\frac{1}{2} \mathbf{S^{-1} S' C_b}. \tag{7.39}$$

Substituting (7.39) in (7.34) we obtain

$$\langle 1|\frac{d}{dX_A}|2\rangle = (\sqrt{n_a}+\sqrt{n_b})\left[-\frac{\mathbf{1}}{\mathbf{2}}\mathbf{C_a^T S' C_b} - \mathbf{C_a^T}\nabla_{\mathbf{e}}\big|_{\nu\in\mathbf{A}}\mathbf{C_b}\right], \tag{7.40}$$

putting it back in explicit form

$$\langle 1|\frac{d}{dX_A}|2\rangle = (\sqrt{n_a}+\sqrt{n_b})\sum_{\mu\nu}\left[-\frac{1}{2}C_{\mu a}S'_{\mu\nu}C_{\nu b} - C_{\mu a}\nabla_{\mu\nu}\big|_{\nu\in A}C_{\nu b}\right], \tag{7.41}$$

Where $S'_{\mu\nu} \equiv \frac{dS_{\mu\nu}}{dX_A} = \langle\frac{d\phi_\mu}{dX_A}|\phi_\nu\rangle + \langle\phi_\mu|\frac{d\phi_\nu}{dX_A}\rangle$, here care must be taken with the operator $\frac{d}{dX_A}$ which will act only on the basis functions centered on atom A, that is $S'_{\mu\nu} = \langle\phi_\nu|\phi'_\mu\rangle\big|_{\mu\in A} + \langle\phi_\mu|\phi'_\nu\rangle\big|_{\nu\in A} = -\nabla_{\nu\mu}\big|_{\mu\in A} - \nabla_{\mu\nu}\big|_{\nu\in A}$. Substituting the latter expression into equation (7.41) we find

$$\begin{aligned}\langle 1|\frac{d}{dX_A}|2\rangle & \\ =&\frac{\sqrt{n_a}+\sqrt{n_b}}{2}\left[\sum_{\mu\in A}\sum_{\nu\notin A}C_{\mu a}C_{\nu b}\nabla_{\nu\mu} + \sum_{\mu\notin A}\sum_{\nu\in A}C_{\mu a}C_{\nu b}\nabla_{\nu\mu}\right],\end{aligned} \tag{7.42}$$

In the first and second terms within the brackets the indices are symmetrical, i.e. one may interchange them and combine the two sums leading to the final expression for the NAC elements in which we put a superscript "Symm" as a reminder that a particular symmetrical solution (7.39) was used.

$$\begin{aligned}\nabla_{12}^{Symm} \equiv&\langle 1|\frac{d}{dX_A}|2\rangle^{Symm} \\ =&\frac{\sqrt{n_a}+\sqrt{n_b}}{2}\sum_{\mu\in A}\sum_{\nu\notin A}\nabla_{\nu\mu}\left[C_{\mu a}C_{\nu b} - C_{\nu a}C_{\mu b}\right],\end{aligned} \tag{7.43}$$

The formula (7.43) is derived by neglecting the antihermitian matrix **Z** in (7.37). The matrix **Z** describes the antisymmetric part of the molecular orbital derivatives w.r.t. the nuclear displacements. In the most accurate way it can be obtained with the use of the coupled-perturbed formalism.

The NAC element that explicitly involves the orbital gradients w.r.t. nuclear displacements is expressed as follows

$$\begin{aligned}\nabla_{12} \equiv&\langle 1|\frac{d}{dX_A}|2\rangle \\ =&(\sqrt{n_a}+\sqrt{n_b})\left[\sum_{\mu\nu}C_{\mu a}S_{\mu\nu}C'_{b\nu} - \sum_{\mu\in A}\sum_{\nu\notin A}C_{\nu a}\nabla_{\nu\mu}C_{\mu b}\right]\end{aligned} \tag{7.44}$$

The $\langle 1|\nabla|3\rangle$ NAC elements (where 3 stands for the S_2 state) can be cast in the form

$$\begin{aligned}\nabla_{13} \equiv & \langle 1|\frac{d}{dX_A}|3\rangle \\ = & \frac{\sqrt{n_a}}{2}\langle a\bar{a}|\frac{d}{dX_A}\big|\sqrt{n_b}|a\bar{a}\rangle + \sqrt{n_a}|b\bar{b}\rangle\big) - \frac{\sqrt{n_b}}{2}\langle b\bar{b}|\frac{d}{dX_A}\big|\sqrt{n_b}|a\bar{a}\rangle + \sqrt{n_a}|b\bar{b}\rangle\big)\end{aligned} \tag{7.45}$$

from which one obtains

$$\nabla_{13} = \frac{\sqrt{n_a}}{2}\frac{d}{dX_A}\sqrt{n_b} - \frac{\sqrt{n_b}}{2}\frac{d}{dX_A}\sqrt{n_a} \tag{7.46}$$

The last nonadiabatic coupling matrix element $\langle 2|\frac{d}{dX_A}|3\rangle$ can be expressed as

$$\nabla_{23} \equiv \langle 2|\frac{d}{dX_A}|3\rangle = (\sqrt{n_a} - \sqrt{n_b})\,\langle a|\frac{d}{dX_A}|b\rangle, \tag{7.47}$$

where $\langle a|\frac{d}{dX_A}|b\rangle$ is the same as in (7.28) which allows us to write immediately the analogous formulas

$$\nabla_{23}^{Symm} = \frac{\sqrt{n_a} - \sqrt{n_b}}{2}\sum_{\mu\in A}\sum_{\nu\notin A}\nabla_{\nu\mu}\left[C_{\mu a}C_{\nu b} - C_{\nu a}C_{\mu b}\right], \tag{7.48}$$

$$\nabla_{23} = (\sqrt{n_a} - \sqrt{n_b})\left[\sum_{\mu\nu} C_{\mu a}S_{\mu\nu}C'_{b\nu} - \sum_{\mu\in A}\sum_{\nu\notin A} C_{\nu a}\nabla_{\nu\mu}C_{\mu b}\right] \tag{7.49}$$

The equations for the NAC elements (7.43, 7.44) are used in connection with the SA-REKS formalism where the (not yet available in the analytic form) derivatives of the KS orbital coefficients are calculated numerically.

7.5 Results

We carried out a series of calculations of NAC elements along the twisting mode of ethylene using SA-REKS/BH&HLYP/6-31G** method. The NAC elements were calculated using the analytic formula (7.43) and formula (7.44). The analytic formula (7.43) yields all cartesian components of the NAC matrix which were projected afterwards onto a selected internal coordinate (SA-REKS(A)). In the formula (7.44) the orbital gradients are evaluated numerically along a given internal coordinate. The numerical results were obtained in two ways: 1) by the direct differentiation along the sought internal coordinate (SA-REKS(B)) or 2) by the differentiation along each

cartesian component of each atom and a subsequent projection of the cartesian NAC matrix onto a given z-matrix, thus yielding the components of the NAC in internal coordinates (SA-REKS(C)).

The components of NAC elements along the bond stretching $\nabla^R_{12} \equiv \langle 1|\frac{d}{dR}|2\rangle$ and twisting $\nabla^\varphi_{12} \equiv \langle 1|\frac{d}{d\varphi}|2\rangle$ modes are plotted against the bond twisting angle φ in Figs 7.3 and 7.4, correspondingly. For comparison, the results of the coupled-perturbed SA-2-CASSCF(2,2)/6-31G** (denoted here as CAS) and MS-2-CASPT2(2,2)/6-31G** (here CASPT2) calculations are shown.

The numerical differentiation was performed using the central two point finite-difference scheme with 1 degree increment for the twist and 0.01 Å for displacements.

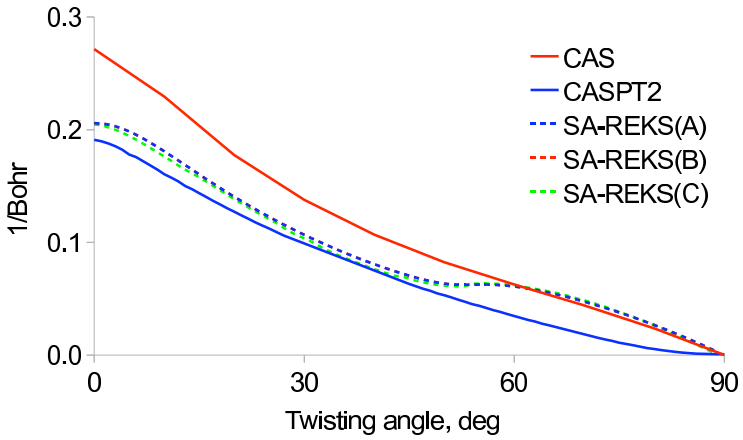

Figure 7.3: *The bond stretching component of NAC ∇^R_{12} against the twisting mode of ethylene molecule. The SA-REKS calculations were performed in three ways: (A) the cartesian NAC matrix elements $\nabla^j_{12}\Big|_{j=X,Y,Z}$ were obtained by the analytical formula (7.43) and subsequently projected to yield the NAC component ∇^R_{12} along bond stretching component; (B) ∇^R_{12} was obtained by the formula (7.44); (C) the $\nabla^j_{12}\Big|_{j=X,Y,Z}$ matrix was obtained by the formula (7.44) and subsequently projected to give the ∇^R_{12} component.*

It is worth noting that the NAC elements along the stretching mode are nearly identical in SA-REKS(A) and SA-REKS(B) calculations This indicates that the antisymmetric contribution $\mathbf{Z}$ to the orbital gradient in (7.37) is in this particular case negligible.

The CAS and CASPT2 curves in 7.3 have similar shapes to that of the SA-REKS curve demonstrating a qualitative agreement of all three methods.

The torsional component of the NAC is shown in Fig 7.3. Here the difference

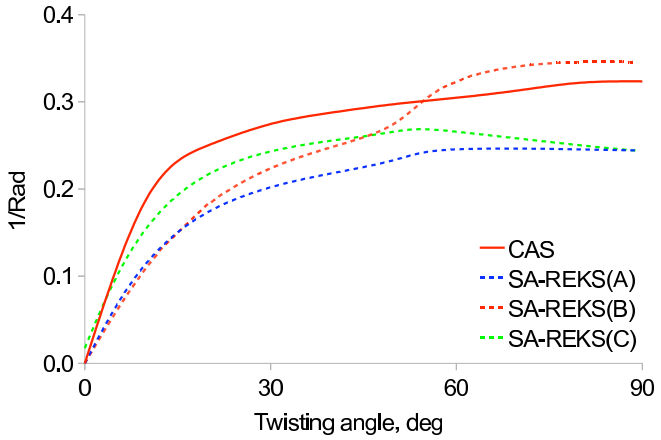

Figure 7.4: *The C=C bond twisting component of NAC ∇^{φ}_{12} against the twisting mode of ethylene molecule. The SA-REKS calculations were performed in three ways: (A) the cartesian NAC matrix elements $\nabla^{j}_{12}\Big|_{j=X,Y,Z}$ were obtained by the analytical formula (7.43) and subsequently projected to yield the NAC component ∇^{φ}_{12} along C=C twisting component; (B) ∇^{φ}_{12} was obtained by the formula (7.44); (C) the $\nabla^{j}_{12}\Big|_{j=X,Y,Z}$ matrix was obtained by the formula (7.44) and subsequently projected to give the ∇^{φ}_{12} component.*

between the SA-REKS(A) and SA-REKS(B) results becomes apparent. The discrepancy may signify that the symmetrized solution (7.38) misses certain contributions from the antisymmetric components in (7.37). Nevertheless, the shape of the SA-REKS(A) curve resembles that of the CAS. The two curves from SA-REKS (B) and (C) calculations are expected to yield similar results, since both take into account the full orbital gradient in (7.44). The behavior of the directly differentiated bond stretch NAC component (SA-REKS(B)) is, however considerably different from SA-REKS(C) at angles greater than 60°. This may be rationalized by the existence of certain additional projections on the torsional direction coming from other displacements. The amount of such additional contributions is difficult to estimate because of the nonunitarity of the transformation which may lead to uncontrollable deteriorations of existing errors from the numerical differentiation.

To conclude, the NAC elements along the torsional and bond stretching modes obtained with SA-REKS using the three types of calculations agree well with the CAS and CASPT2 results. Both the absolute values and the shapes of the NAC curves are in a qualitative agrement in all calculations. The results obtained with the analytical formula (7.43) are identical to the ones obtained by the full numerical

formula (7.44) in case where the antisymmetric contribution is negligible (e.g. C=C bond stretching).

It has been demonstrated that the inclusion of the full orbital gradients leads to somewhat different results, manifesting the occurrence of the nonzero antisymmetrical component in (7.37). To accurately estimate the amount of the components overlooked in the symmetrized formula the analytic NAC gradients must be obtained with the help of coupled-perturbed formalism.

We have demonstrated the utility of the SA-REKS formalism for the optimization of the conical intersections and for the calculation of the NAC. The preliminary tests show that the method is capable of yielding accurate results for these properties. However, a considerable improvement can be obtained with the use of analytic formalism for the calculation of the NAC and gradient difference vectors.

Chapter 8

OM2/GUGA-CI study of fluorene motor

8.1 Introduction

In the Chapter 6 we carried out the study of photoisomerization dynamics of the fluorene-based molecular motor (**1** within this chapter). For that purpose we set up a hybrid scheme were a classical (OPLS) force field was parametrized to reproduce the quantum chemical (SA-REKS) ground S_0 and excited S_1 states energy surfaces. We then ran a series of MD simulations using the parametrized force fields. The hopping from the excited to the ground state was initiated as soon as the geometry approached sufficiently close one of the two conical intersection structures. To determine the CI structures we performed (ground state relaxed) scans of the the S_0 and S_1 PESs along the torsional and pyramidalization coordinates in analogy with ethylene where these coordinates are known to lead to a conical intersection. The use of MECI search algorithms was not possible because of the absence of analytic gradients for the excited state, and employing the penalty function method would be highly inefficient in the case of the molecular motor.

The full cycle or rotation in **1** consists of a photoisomerization step P→M followed by a thermal helix inversion step M→P' as shown in 8.1A. The molecular motor is designed in such a way that the photoisomerization occurs preferably in the direction P→M and not M→P which is schematically represented in 8.1B.

To better understand the mechanism of photoisomerization of the molecular motor **1** it is necessary to identify the MECI structures CI_1 and CI_2 and also the CI seams in the vicinity of CI_1 and CI_2. The hybrid scheme used in Chapter 6 can then be extended to incorporate the CI structures from the seams encompassing the MECIs CI_1 and CI_2.

The objective of this Chapter is to study the MECI structures applying the semiempirical configuration interaction program recently developed in the group of Walter Thiel [235] which is based on the orthogonalization corrected (OM2) Hamiltonian. [236, 237] and the GUGA-CI approach. [73] The OM2/GUGA-CI method has been shown to reproduce the results from high-level *ab initio* methods such as CASPT2 and MRCI. [238, 239] One of the main advantages of the method is its

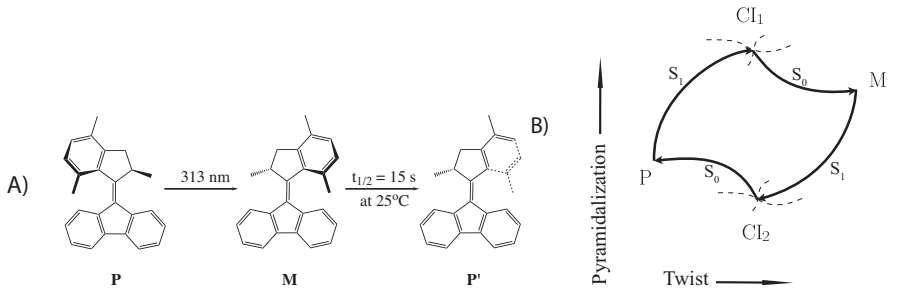

Figure 8.1: *A) Isomerization cycle of molecular motor* **1**. *B) Schematic representation of two possible minimum energy reaction paths connecting P and M conformers via CI_1 and CI_2 conical intersections. Presumed CI seams in directions of twist and pyramidalization are depicted by dashed lines.*

applicability to realistic compounds, such, e.g. biologically relevant molecules. [26]

The full MD study with a range of CI structures is in progress and will be discussed elsewhere. In this chapter we study the MECI structures and CI seams of the molecular motor **1**. The minimum energy path (MEP) connecting the FC point, MECI and the product is obtained. In this study we aim at i) determining the MECI structures reached from P and M conformers and comparing them with the previously obtained SA-REKS CI structures. ii) identifying the characteristic photoisomerization pathway in the photo-step P→M of the molecular motor **1**, iii) studying the CI seams near the MECI points.

8.2 Theory

In the present study we used the orthogonalization-corrected OM2 semiempirical Hamiltonian [236, 237] and the GUGA-CI approach [73] was employed to calculate the ground and excited energies, optimize geometries in the ground and excited states, and at the conical intersection seams. The details of the GUGA-CI method can be found in the Ref. [73], while here we only mention briefly the main points of the OM2 method.

In the Roothaan-Hall equation (see section 2.6)

$$\mathbf{FC} = \mathbf{SC}\boldsymbol{\varepsilon}, \tag{8.1}$$

the Fock matrix $F_{\mu\nu}$ is given by

$$F_{\mu\nu} = h_{\mu\nu} + \sum_{i}^{N/2} \sum_{\tau\zeta} C_{\tau i} C_{\zeta i}^{*} [2(\mu\nu|\tau\zeta) - (\mu\tau|\zeta\nu)], \tag{8.2}$$

where the two-electron repulsion integrals are explicitly written as

$$(\mu\nu|\tau\zeta) = \int\int \phi_{\mu}^{A}(\mathbf{1}) \phi_{\mu}^{B}(\mathbf{1}) \frac{1}{\mathbf{r_{12}}} \phi_{\tau}^{C}(\mathbf{2}) \phi_{\zeta}^{D}(\mathbf{2}) \mathbf{dr_1 dr_2}, \tag{8.3}$$

where A, B, C and D label the atoms on which the basis functions ϕ are centered. The equation (8.1) is usually brought to the form of an eigenvalue problem

$$^{\lambda}\mathbf{F}\,^{\lambda}\mathbf{C} = {}^{\lambda}\mathbf{C}\boldsymbol{\varepsilon}, \tag{8.4}$$

by the Löwdin basis orthogonalization.

$$^{\lambda}\mathbf{F} = \mathbf{S^{-1/2}}(\mathbf{h} + \mathbf{G})\mathbf{S^{1/2}} \tag{8.5}$$

The Fock operator can be partitioned as follows,

$$\mathbf{F} = \mathbf{h^{1c}} + \mathbf{h^{2c}} + \mathbf{G^{1c}} + \mathbf{G^{mc}}, \tag{8.6}$$

Where $\mathbf{G^{1c}}$ is the one-center and $\mathbf{G^{mc}}$ is the manycenter repulsion parts, which may be written as

$$\mathbf{G^{mc}} = \mathbf{G_{BB}^{AA}} + \mathbf{G_{AB}^{AA}} + \mathbf{G_{AB}^{AB}} + \mathbf{G_{AC}^{AB}} + \mathbf{G_{CD}^{AB}} \tag{8.7}$$

The orthogonalization leads to vanishingly small three- and four-center two-electron terms such as $\mathbf{G_{AC}^{AB}}$ and $\mathbf{G_{CD}^{AB}}$. [240] So that the Fock operator (8.5) can be written as

$$^{\lambda}\mathbf{F} = {}^{\lambda}\mathbf{h^{1c}} + {}^{\lambda}\mathbf{h^{2c}} + {}^{\lambda}\mathbf{G^{1c}} + {}^{\lambda}\mathbf{G_{BB}^{AA}} \tag{8.8}$$

In semiempirical methods the two-electron integrals are usually approximated by the zero differential overlap (ZDO)

$$(\mu\nu|\tau\zeta)\Big|_{\substack{\mu\neq\nu \\ \tau\neq\zeta}} = 0 \tag{8.9}$$

and the semiempirical secular equations are written as

$$\mathbf{F^{ZDO}C^{ZDO}} = \mathbf{C^{ZDO}}\boldsymbol{\varepsilon}, \tag{8.10}$$

thus, implicitly assuming the basis orthogonalized

$$\mathbf{F^{ZDO}} \approx {}^{\lambda}\mathbf{F}. \tag{8.11}$$

In this case, however, the representation (8.8) ceases to be exact. The orthogonalization correction can be estimated by expanding the overlap terms in (8.5) in binomial series. [241] Brown and Roby [241] have demonstrated that the expansion of the core one- and two-center hamiltonian terms leads to emergence of three- and four- center two-electron terms (8.7). This corrections are neglected in many semiempirical methods which often results in severe inaccuracies.

The orthogonalization of basis in *ab initio* methods leads to a raise of the orthogonal atomic orbitals (OAO) energy levels with respect to the atomic orbitals (AO) levels. The splitting of OAOs into the bonding and antibonding MOs results in asymmetric MOs with respect to the original AOs as depicted in 8.2.

The AO energy levels in ZDO approximation are unshifted and symmetrically split into the MOs as illustrated in Fig. 8.2. This results in a considerable underestimation of the Pauli repulsion between the completely occupied shells. The widely known semiempirical methods such as MNDO, AM1 and PM3 are based on the so-called neglect of diatomic differential overlap (NDDO) approximation which adopts (8.9) if $A \neq B$ and $C \neq D$ in (8.3).

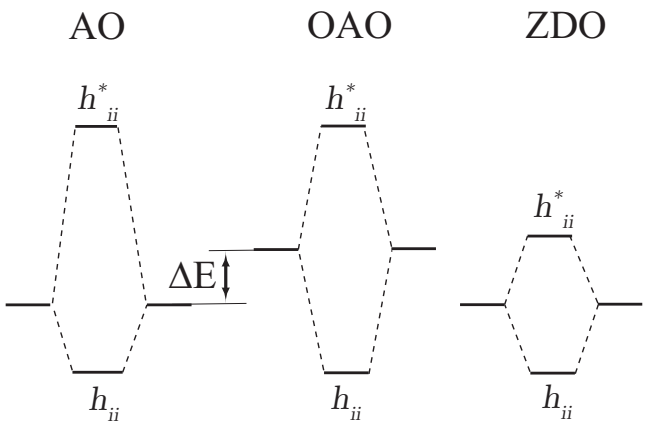

Figure 8.2: *Molecular orbital (MO) diagram for the original atomic orbitals (AO) and orthogonalized atomic orbitals (OAO). The bonding and antibonding MOs are denoted h_{ii} and h^*_{ii}, respectively. The ZDO approximation neglects the orthogonalization correction ΔE, which results in a symmetric splitting of AOs into MOs and yielding too low an antibonding MO.*

The orthogonalization of atomic basis leads to delocalization of the electron density. Since overlap integrals decrease exponentially with increasing distance, the orthogonalization effects are most important at short distances. In this respect a

number of corrections to the one-center core Hamiltonian have been proposed by introducing the dominant terms of the orthogonalization effects via effective core potential. [242–246]

In addition to the dominant terms for the one-center core Hamiltonian, it was proposed by Weber and Thiel [236, 237] to introduce the corrections to the two-center core Hamiltonian core by incorporating three-center terms via a suitably parameterized pseudopotential. The approach was called orthogonalization method 2 (OM2). For the details of the method the reader is referred to the Refs [236, 237]. The method has been successfully applied to various situations and shown to perform in all cases better than the standard MNDO, AM1 and PM3 methods. [239] The approach when employed together with the configuration interaction GUGA-CI method has been demonstrated to yield excitation energies comparable in accuracy with the high level *ab initio* methods. [238, 239]

8.3 Method of calculation

We performed the configuration interaction calculations for the orthogonalization corrected method OM2 including single and double excitations using the graphical unitary group approach (GUGA) as implemented in the MNDO code. [235] Three reference configurations were used (closed-shell, single and double HOMO-LUMO excitations) to build the MRCI expansion. The active space comprised 12 electrons in 11 orbitals, which was found suitable for a stable geometry optimization along the isomerization path including the CI points. The tracking of the π character of the orbitals in the active space was used. The optimization of CI structures was performed using the Lagrange-Newton scheme [51, 247] discussed in section 7.2. For comparison, CASSCF/6-31G** (CAS) optimization of a MECI structure was performed using the MOLPRO package. [248] The CAS calculations were carried out with active spaces (6,6) and (8,8). The details of SA-REKS calculations are explained in Chapter 6.

8.4 Results and discussion

The results of geometry optimizations are summarized in Tab. 8.1 The energies are listed in Tab. 8.2 and compared with those obtained at the SA-REBH&HLYP/6-31G** level in Chapter 6. The labeling for torsional angles is given in 8.3. The twisting angle is the dihedral angle between the 1'a-1'-2' and 8a-9-9a planes. The pyramidalization angle is defined as $180^\circ - \zeta$, where ζ is the angle between the bond 1'-9 and 8a-9-9a plane. It should be noted that the improper dihedral α is not

identical to the pyramidalization angle as are the twisting angle and the torsion θ.

We optimized the thermally stable P and unstable M conformations in the ground state (respectively P_{S_0} and M_{S_0}) and the transition state geometry TS. Starting, correspondingly, from P_{S_0} and M_{S_0}, the excited state minima P_{S_1} and M_{S_1} were localized. The two structures obtained are similar, however the fluorene residue in P_{S_1} is noticeably kinked. The MECI structures CI_1 and CI_2 were optimized starting from P_{S_1} and M_{S_1}. The two MECI structures feature strong pyramidalization of C_9 atom, however the rotor is leaning to the opposite sides of the stator. The structures obtained with OM2/GUGA-CI method are in a very good agreement with those obtained at SA-REKS level as can be seen in Fig. 8.4

The energies of the MECI structures agree well with those obtained with SA-REKS method. The MECIs from the OM2/GUGA-CI method are nearly degenerate energetically, whereas there was a slight energy difference between the S_0 and S_1 states in the CI_1 and CI_2 obtained with SA-REKS. It is interesting to note the excellent agreement of the CI_1 geometries as obtained at the CAS and OM2/GUGA-CI methods.

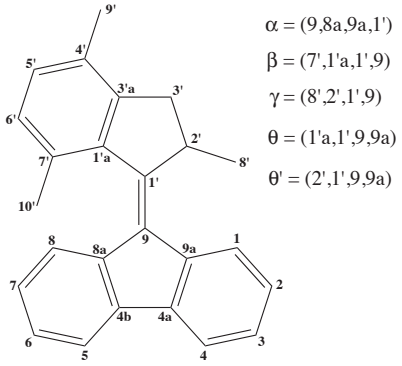

1

Figure 8.3: *The atom numbering and definition of torsion angles of the molecular motor* **1**.

After localizing the minima in the ground and excited states and optimizing the MECI structures, the reaction path was constructed connecting these points. We used the linear interpolation between P_{S_0} and P_{S_1} structures to perform constraint S_1 state geometry optimizations along the so-obtained reaction path. Similarly we found the path connecting P_{S_1} and CI_1 structures as illustrated in Fig 8.5

The energy along the linearly interpolated path between CI_1 and M structures

Table 8.1: *The OM2/GUGA-CI, SA-REKS, CAS(6,6) and CAS(8,8) geometries of stable conformations, transition states and at conical intersections.*

	CC	α	β	γ	θ	twist	pyr
P_{S_0}	1.359	0.7	-39.6	102.2	168.2	161.8	1.1
$P_{S_0}^{SAREKS}$	1.368	1.7	-43.1	105.5	169.2	161.1	2.8
M_{S_0}	1.364	1.3	27.0	41.2	27.2	28.7	2.1
$M_{S_0}^{SAREKS}$	1.376	1.7	30.0	32.4	31.7	32.2	2.8
P_{S_1}	1.400	16.4	1.5	59.4	110.2	90.2	26.7
M_{S_1}	1.392	4.3	0.7	58.6	85.3	89.9	6.9
TS	1.438	0.2	0.2	59.1	90.0	90.3	0.3
TS^{SAREKS}	1.463	0.0	5.6	66.0	90.0	91.8	0.0
CI_1	1.420	35.5	5.7	67.2	133.5	85.0	58.0
CI_1^{SAREKS}	1.490	34.0	3.8	36.8	120.0	92.2	52.7
CI_1^{CASa}	1.427	36.7	6.4	68.6	135.0	95.6	59.7
CI_1^{CASb}	1.423	35.5	4.9	64.9	131.0	93.0	58.1
CI_2	1.405	-32.6	3.2	59.6	56.1	92.2	-53.6
CI_2^{SAREKS}	1.472	-30.0	4.9	45.5	70.0	81.5	-47.9

[a)] CAS(6,6)
[b)] CAS(8,8)

Table 8.2: *The OM2/GUGA-CI and SA-REKS (in parentheses) energies of stable conformations, transition states and at conical intersections. All energies are relative to the respective ground state energy of the P conformer.*

	P	M	TS	P_{S_1}	M_{S_1}	CI_1	CI_2
S_0	0	0.09 (0.15)	1.55 (1.39)	1.77	1.64	2.72 (2.93)	2.87 (3.05)
S_1	3.93 (3.8)	3.75 (3.55)	2.69 (2.95)	2.56	2.56	2.72 (3.09)	2.87 (3.21)

changes abruptly. To find a smooth path we optimized the geometry for the ground state en route the M-conformer. Due to an almost immediate flattening of the initially pyramidalized residue in the ground state, the energy drops when departing from the CI_1 structure. To decrease this effect, the pyramidalization was kept frozen to the interpolated values, while the rest of the coordinates, except the torsion, were optimized. Following the outlined procedure we obtained a reaction path connecting the P_{S_0}, P_{S_1}, CI_1 and M_{S_0} structures. As can be seen in the figure 8.5, the S_1 path features a rather shallow minimum suggesting that the system can approach the CI_1 unhindered. This is a qualitative observation since the dynamic trajectories may take different paths. Furthermore, the conical intersection represents a multidimensional

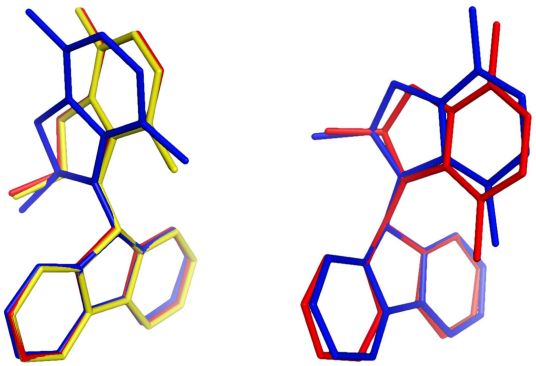

Figure 8.4: *MECI structures obtained by OM2/GUGA-CI method (red) superimposed with the CI structures obtained by the SA-REKS/BH&HLYP/6-31G** method (blue) and CAS(8,8)/6-31G** method (yellow).*

hypersurface rather than a single point. However, the most important role in the photoisomerization dynamics play conical intersections that can be reached from FC region unhampered [17, 187] To augment the manifold of the CI points near MECIs we carried out optimization of the CI seams along the twisting and pyramidalization modes. Schematically the reaction paths connecting the FC points, S_1 minima and MECI points are depicted in 8.1. The targeted CI seams are depicted by dashed curves crossing the CI_1 and CI_2 points. The optimization was performed using the same technique as during the search for MECI points except that a certain internal coordinate (twist or pyramidalization) was kept fixed. The results are shown in Figs 8.6 and 8.7

It was found that the CI seams along the twisting mode are rather shallow. The CI seams along the pyramidalization coordinate were more difficult to optimize in the vicinity of the MECIs. The latter appeared steeper than the twisting seams - even small changes in the pyramidalization angle would result in the optimization failure or end up at a substantially deformed structure differing in energy by more than 1 eV. Therefore we only retained the two nearest structures to the MECIs. This finding may seem to confront the assumptions in the previous chapter that the pyramidalization seams in ethylene, methaniminium and stilbene are shallow. However, in this case the steric effects from the methyl groups are non-negligible and the strong tension at the pyramidalized structures must definitely lead to steeper wells near MECIs.

To summarize, in this chapter we discussed a pilot study of the CI structures and seams which aims to corroborate the previous results obtained with the CI structures

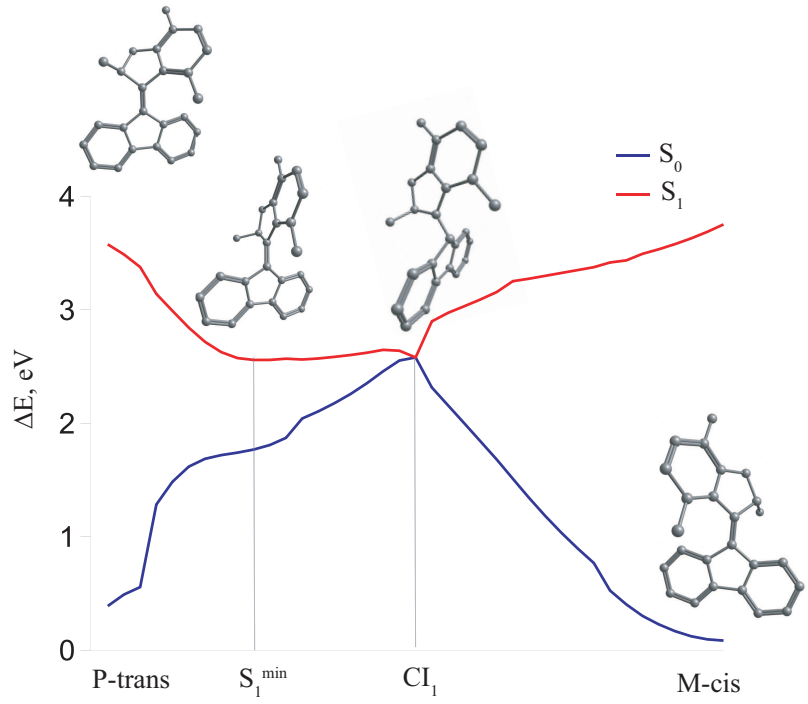

Figure 8.5: *The minimum energy path of the P→M photoisomerization step of the molecular motor* **1** *calculated at the OM2/GUGA-CI level. The MEP starts at the FC point (P-trans) passess the excited state minimum (S_1^{min}), reaches the MECI CI_1, and falls down to the M-conformer in the ground state.*

from SA-REKS calculations and to extend the study of dynamics of the fluorene based molecular motor **1** discussed in Chapter 6 by introducing a manifold of CI structures near MECIs. The geometries and energies of the main ground state conformations agree well in OM2/GUGA-CI and SA-REKS methods. The CI structures found at the SA-REKS level are in a reasonable agreement with the OM2/GUGA-CI structures. The OM2/GUGA-CI CI_1 geometry is in an excellent agreement with the corresponding CAS(8,8) result. The barrierless reaction path connecting the FC point (P) with the excited state minimum, CI_1 and the product (M) was found, which supports the previous suggestions that the CI_1 point is easily reachable from the Franck-Condon region.

The further study of the dynamics of the fluorene based molecular motor will be

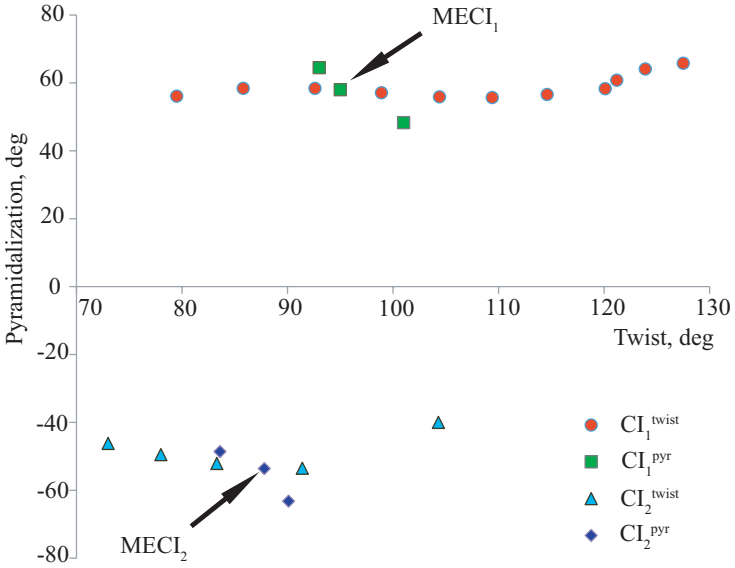

Figure 8.6: *The CI seams crossing the CI_1 and CI_2 points. The seams were optimized along the pyramidalization and twisting coordinates using the OM2/GUGA-CI method.*

performed in the hybrid quantum-chemical scheme discussed in the section 6 by employing the CI structures optimized by the OM2/GUGA-CI method. In this scheme the PESs in the ground and excited state is described by a force field parameterized to quantum chemical PESs, and the forces are calculated classically on-the-fly. The transition from the excited to ground state is induced as soon as the geometry becomes sufficiently close to one of the manifold of conical intersection structures obtained in section 8.4.

Even though such a procedure is simple and quite efficient in certain cases, it may miss specific quantum dynamic aspects such as i) transitions at avoided crossings where the PESs are strongly coupled, ii) reverse transitions, iii) correct statistical population of electronic states. A more elaborate scheme employing Tully's surface hopping SH algorithm [249] is implemented in the MNDO program,[235] developed in the group of Walter Thiel, where the PESs, nonadiabatic coupling and gradient difference vectors are evaluated on-the-fly using the OM2/GUGA-CI method. [73, 236, 237] The method allows to take into account the quantum decoherence effect, which when neglected can lead to certain artefacts. Currently a nonadiabatic semiempirical SH study of the fluorene-based molecular motor **1** using the MNDO

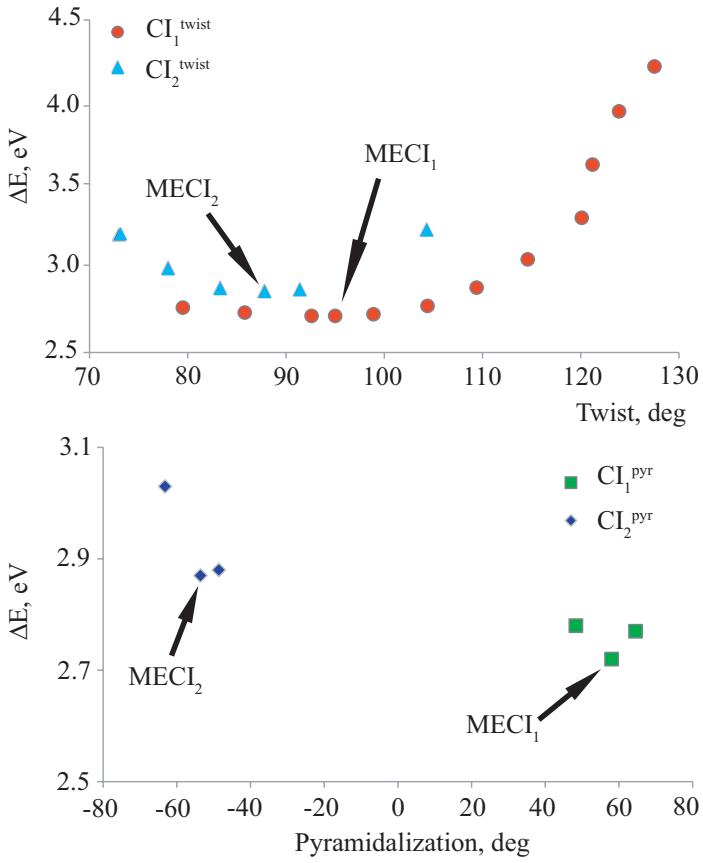

Figure 8.7: *The CI seams optimized along the pyramidalization and twisting coordinates using the OM2/GUGA-CI method.*

package [235] is in progress.

Chapter 9

Conclusions and Outlook

In this thesis we discussed the photoisomerization mechanism and dynamics of organic light driven rotary molecular motors which are capable of performing a unidirectional rotation upon absorption of light. The unidirectional rotation is achieved in a sequence of steps where an isomerization about the double bond is followed by a thermal helix inversion reaction driven by the steric repulsion between the stator and the rotor parts of the motor.

We discussed the quantum chemical methods that can adequately describe the process of bond breaking. For molecules of a size of a typical synthetic molecular motor ($\gtrsim$50 atoms) it becomes increasingly difficult to apply high-level *ab initio* methods, such as CASPT2 or MRCI, therefore one resorts the to DFT based methods. Conventional DFT cannot, however describe strong static electron correlation arising in the double bond breaking process. Alternatively, one may consider ensemble-DFT based methods. We have considered the practical implementations of ensemble-DFT in the restricted open-shell Kohn-Sham (ROKS) and Restricted Ensemble-referenced Kohn-Sham (REKS) methods in the context of extension of DFT to situations where the static correlation is dominating the electronic structure. For our purposes we need an accurate description of both the ground S_0 and the excited S_1 states. We therefore developed a method based on ensemble representation of the ground and excited state energies which is termed the State-Averaged (SA) REKS method. We tested the SA-REKS method against model compounds and compared the results with the corresponding CASPT2 results and available experimental data. A very good agreement was found in the dissociation energies and double-bond torsion potentials.

The proposed method has been used for the study of S_0 and S_1 energy profiles of the first generation light-driven molecular motor. Based on a qualitative analysis of the landscapes of the energy profiles a preliminary conclusion has been drawn concerning the preferability of unidirectional photoisomerization. The explanation of the specific asymmetry in the landscapes of the ground and excited states energy profiles was suggested.

The radiationless relaxation at the subpicosecond timescales is nowadays almost exclusively attributed to the decay via conical intersections where the ground and excited states energies become degenerate. A pure twist in alkenes will not normally

bring the molecule to the point of degeneracy, additional deformations are needed, such as, e.g. pyramidalization. Therefore, to explain the experimentally observed ultrafast radiatoinless photoisomerization we extended the study of potential energy profiles to potential energy surfaces (PES) including the pyramidalization coordinate. We performed the study of the ground and excited state PESs in one of the latest versions of molecular motors synthesized in the group of B. Feringa - the fluorene-based molecular motor 9-(2,4,7-trimethyl-2,3-dihydro-1H-inden-1-ylidene)-9H-fluorene. By scanning the PESs in the two dimensions we have found two strongly pyramidalized conical intersection (CI) structures. Subsequently, a classical force field was parameterized to reproduce the profiles of the quantum-chemical PESs obtained with the SA-REKS method. Using the parameterized force-field we ran molecular dynamics (MD) simulations in which the transitions from the excited to the ground state PES were initiated by the proximity to one of the CI structures. A statistical analysis has revealed a preferable isomerization in one direction with the photostationary state ratio 3.5:1 in a good agreement with the experiment (3:1). The results of this study bear important implications for the design of molecular rotors. For example, it seems less favorable to use compounds that feature strong pyramidalization at conical intersections, since the latter immersed in a viscous solution must be hindered on the way to the conical intersection by the environment which must be reflected in the overall quantum yield.

A thorough investigation of nonadiabatic processes leading to ultrafast decay requires knowledge of the nonadiabatic coupling between the PESs and CI geometries. We addressed the calculation of nonadiabatic coupling (NAC) matrix elements and optimization of CI geometries by use of the SA-REKS method. The NAC matrix elements were calculated along the torsion mode of ethylene molecule using SA-REKS, CASSCF and CASPT2 methods. The results from all three methods are in excellent agreement. To optimize the CI geometries we resorted to the numerical scheme because the analytic gradient difference and NAC vectors are not available in the SA-REKS method yet. We optimized the minimum energy CI (MECI) geometries of ethylene, methaniminium, a protonated Schiff base and stilbene. It has been demonstrated that all the MECI geometries obtained with SA-REKS method compare well with the structures obtained at the CASPT2 and MRCI levels. It was found, however, that in certain cases the pyramidalization can be substantially different in the MECI geometries obtained with different methods. It is argued that such deviations stem from a shallow CI seam, in which case a numerical optimization algorithm may be insufficiently accurate.

To confirm the results obtained for the fluorene molecular motor with the use of the SA-REKS method we have undertaken a study of the photoisomerization mechanism using a semi-empirical computational scheme specifically designed to describe

the excited state PESs, the semiempirical orthogonalization corrected OM2 configuration interaction (GUGA-CI) method. The analytic NAC and gradient difference vectors are available in the OM2/GUGA-CI method which makes it possible to optimize for the MECI geometries and CI seams. It has been found that the MECI geometries optimized by the OM2/GUGA-CI method are in a good agreement with the CI structures obtained with the SA-REKS method. The minimum energy reaction path connecting the Franck-Condon (FC) point with the excited state minimum, MECI point and the product has been constructed. It was pointed out that the pathway from the FC point to the MECI structure is barrierless which supports our previous conclusion that the isomerization via the CI structures found by SA-REKS method should be favored during the photoreaction.

Using OM2/GUGA-CI method we determined a manifold of CI structures near the MECI geometries along the twist and pyramidalization angles. This set of CI structures will be used to extend the criterion of hopping in the previous hybrid quantum-classical scheme. The study is currently in progress.

To address the importance of nonadiabatic effects and quantum corrections for the nuclear motion in the photoisomerization dynamics of the fluorene-based molecular motor we will apply the nonadiabatic surface hopping (SH) method as implemented in the MNDO program package. The nonadiabatic SH method allows one to obtain a realistic dynamics including nonadiabatic effects which are evaluated on-the-fly and introducing quantum decoherence to avoid the artefacts related to the classical population of the electronic states.

The photoisomerization of synthetic molecular motors can be accurately described in the context of DFT by use of the recently developed SA-REKS method. To facilitate the computations the analytic gradient difference and nonadiabatic coupling vectors will be implemented. With the analytic gradients the SA-REKS method can be efficiently employed in hybrid QM/MM schemes for simulations of nonadiabatic dynamics with surface hoppings.

Chapter 10

Samenvatting

In dit proefschrift hebben we het fotoisomerisatiemechanisme en de dynamica van organische, licht-aangedreven, roterende moleculaire motoren die in staat zijn om een gerichte rotatie uit te voeren na de absorptie van licht besproken. De gerichte rotatie wordt bereikt in een sequentie van stappen waarin een isomerisatie over de dubbele binding gevolgd wordt door een thermische helix inversiereaktie die aangedreven wordt door sterische repulsie tussen de stator en de rotor gedeeltes van de motor.

We hebben de quantummechanische methoden besproken die het process van het verbreken van een binding adequaat kunnen beschrijven. Voor molekulen met een grootte van een typische synthetische moleculaire motor ($\gtrsim$50 atomen) wordt het steeds moeilijker om een *ab initio* methode van hoog niveau toe te passen, zoals CASPT2 of MRCI. Daarom neemt men de toevlucht tot DFT gebaseerde methoden. Conventionele DFT kan evenwel niet de sterke statische electroncorrelatie beschrijven dat zich voordoet in het proces van het breken van een dubbele binding. Als alternatief kan men ensemble-DFT methoden overwegen. Wij hebben de practische implementaties van ensemble-DFT in de restricted Open-Schell Kohn-Sham (ROKS) en in de Restricted Ensemble-Referenced Kohn-Sham (REKS) methoden beschouwd in de context van de uitbreiding van de toepasbaarheid van DFT naar situaties waar de statische correlatie domineert in de electronische struktuur. Voor ons doel hebben we een nauwkeurige beschrijving van zowel de S_0 grond als de aangeslagen S_1 toestanden nodig. We hebben daarom een method ontwikkeld die gebaseerd is op een ensemble representatie van de grond- en aangeslagentoestandsenergieën, de State-Averaged (SA) REKS methode. We hebben de SA-REKS method tegen model verbindingen getest en de resultaten vergeleken met corresponderende CASPT2 resultaten en beschikbare experimentele data. Een erg goede overeenkomst is gevonden in de dissociatieenergieën en in de torsie potentialen van de dubbele binding.

De voorgestelde methode is gebruikt voor de bestudering van de S_0 en S_1 energieprofielen van de eerste generatie licht-aangedreven moleculaire motoren. Op basis van een kwalitatieve analyse van de landschappen van de energieprofielen is een eerste conclusie getrokken met betrekking tot de voorkeur van de fotoisomerisatie in één richting. De verklaring van de specifieke asymmetrie in de landschappen van de

energie van de grond- en aangeslagen toestanden is voorgesteld.

De stralingsloze relaxatie bij sub-picoseconde tijdschalen wordt tegenwoordig bijna exclusief toegeschreven aan het verval via conische intersecties waar de energieën van de grond- en aangeslagentoestand ontaard worden. Een zuivere draaiing in alkenen zal normal gesproken het molekuul niet op het punt van ontaarding brengen. Aanvullende deformaties zijn benodigd, zoals bijvoorbeeld pyramidalisatie. Daarom moeten we de bestudering van potentiele energie profielen uitbreiden naar potentiele energie oppervlakken (PES) waarin de pyramidalisatie coordinaat is opgenomen. We hebben de grond- en aangeslagentoestand PES-en bestudeerd van de laatste versies van de moleculaire motoren die in de groep van B. Feringa zijn gesynthetiseerd - de fluoreen-gebaseerde moleculaire motor 9-(2,4,7-trimethyl-2,3-dihydro-1H-inden-1-ylidene)-9H-fluorene. Door de PES-en in twee dimensies te scannen hebben we conische intersectie (CI) structuren gevonden die sterk zijn pyramidaliseerd. Vervolgens werd een klassiek force field geparametriseerd om de quantum-chemische PES-en die met de SA-REKS method zijn bepaald te reproduceren. Met dit geparameteriseerde force-field hebben we moleculaire dynamica (MD) simulaties uitgevoerd waarin de overgang van de aangeslagen- naar de grondtoestand werd geinitieerd door de nabijheid tot een van de CI strukturen. Een statistische analyse heeft uitgewezen dat de isomerisatie bij voorkeur in één richting plaatsvindt met een fotostationairetoestandsratio van 3.5:1, in goede overeenstemming met het experiment (3:1). De resultaten van deze studie hebben een belangrijke implicatie voor het ontwerp van moleculaire rotoren. Het lijkt bijvoorbeeld minder gunstig om een verbinding te gebruiken dat sterke pyramidalisatie vertoont bij conische intersecties omdat zo'n verbinding, ondergedompeld in een visceuze oplossing, door de omgeving gehinderd zal worden op weg naar de conische intersectie en dat zal tot uiting moeten komen in de gezamenlijke quantum yield.

Een grondig onderzoek naar niet-adiabatische processen die leiden tot ultra-snel verval vereist de kennis van de niet-adiabatische koppeling (NAC) matrixelementen en de met behulp van de SA-REKS methode geoptimaliseerde CI gemetrieën. De NAC matrix elementen zijn met SA-REKS, CASSCF en CASPT2 berekend langs de torsie mode van het ethylene molekuul. De resultaten van alle drie methoden zijn in excellente overeenstemming. Om de CI geometriën te optimaliseren hebben we de toevlucht genomen tot een numeriek schema omdat een analytische gradient verschillen en de NAC vectoren nog niet beschikbaar waren in de SA-REKS methode. We hebben de minimum energie CI (MECI) geometriën van ethyleen, methaniminium, een geprotoneerde Schiff base, en stilbeen bepaald. Het is aangetoond dat alle met SA-REKS verkregen MECI geometriën in goede overeenkomst zijn met de strukturen die warden bepaald op CASPT2 en MRCI niveau. Er werd echter gevonden dat in sommige gevallen de pyramidalisatie substantieel kan verschillen in de MECI

geometriën verkregen met de verschillende methoden. Er wordt betoogd dat zulke afwijkingen voortkomen uit een vlakke CI seam waarin een numeriek algoritme niet voldoende accuraat zou kunnen zijn.

Om deze met SA-REKS bepaalde resultaten voor de fluoreen moleculaire motor te bevestigen hebben we een studie gedaan naar het fotoisomerisatiemechanisme met behulp van een semi-empirisch schema dat specifiek ontworpen is om de aangeslagen toestand PES-en te beschrijven, de semi-empirische orthogonalisatie gecorrigeerde OM2 configuratie interactie (GUGA-CI) methode. De analytische NAC en gradient verschil vectoren zijn zijn beschikbaar in de OM2/GUGA-CI method zodat het mogelijk is om de MECI geometriën en CI seams te optimaliseren. Er is gevonden dat de MECI gemetriën die geoptimaliseerd zijn met de OM2/GUGA-CI methode in goede overeenstemming zijn met de CI strukturen die met de SA-REKS methode zijn verkregen. Het minimum energie reaktiepad is geconstueerd dat het Franck-Condon (FC) punt met het minimum van de aangeslagen toestand, het MECI punt en het product verbind. Er werd op gewezen dat het pad van het FC punt naar de MECI struktuur zonder barrière is. Dit ondersteund onze vorige conclusies dat de isomerisatie via de met SA-REKS gevonden CI strukturen de voorkeur zal hebben tijdens de fotoreaktie.

Gebruik makend van de OM2/GUGA-CI methode hebben we het manifold aan CI strukturen in de nabijheid van de MECI geometriën bepaald langs de twist en pyramidalisatiehoeken. Deze set CI strukturen zal gebruikt worden om het hopping criterium uit te breiden in het vorige hybide quantum-klassieke schema. De studie is momenteel in voortgang.

Om de belangrijkheid van niet-adiabatische effecten en quantum correcties voor nucleaire beweging in de fotoisomerisatie dynamica van fluoreen-gebaseerde moleculaire motoren aan te duiden, zullen we de niet-adiabatische surface hopping (SH) methode gebruiken zoals die geimplementeerd is in het MINDO pakket. De niet-adiabatische SH methode stelt ons in staat om realistische dynamica te verkrijgen inclusief de niet-adiabatische effecten die on-the-fly zijn berekend en die quantum decoherence introduceren om de artefacten verbonden met de klassieke populatie van de electronische niveaus te vermijden.

De fotoisomerisatie van synthetische moleculaire motoren kan nauwkeurig beschreven worden in de context van DFT gebruik makend van de recent ontwikkelde SA-REKS methode. Om de berekening te vergemakkelijken zal het analytische gradient verschil en de niet-adiabatische koppelingsvectoren worden geimplementeerd. Met behulp van de analytische gradienten kan de SA-REKS method efficient worden toegepast in hybride QM/MM schemas voor de simulatie van niet-adiabatische dynamica met surface hoppings.

Bibliography

[1] R. R. Birge, N. B. Gillespie, E. W. Izaguirre, A. Kusnetzow, A. F. Lawrence, D. Singh, Q. W. Song, E. Schmidt, J. A. Stuart, S. Seetharaman, and K. J. Wise, *J. Phys. Chem. B*, vol. 103, pp. 10746, 1999.

[2] J. E. Walker, *Angew. Chem. Int. Ed*, vol. 37, pp. 2308, 1998.

[3] P. D. Boyer, *Angew. Chem. Int. Ed*, vol. 37, pp. 2296, 1998.

[4] V. Sundstrom, *Annu. Rev. Phys. Chem*, vol. 59, pp. 53, 2008.

[5] G. E. Busch, M. L. Applebury, A. A. Lamola, and P. M. Rentzepis, *Proc. Natl. Acad. Sci. USA*, vol. 69, pp. 2802, 1972.

[6] R. P. Feynman, *http://www.zyvex.com/nanotech/feynman.html*, 1960.

[7] M-M. Russew and S. Hecht, *Adv. Mater*, vol. 22, pp. 3348–3360, 2010.

[8] J. Michl and E. C. H. Sykes, *ACSNANO*, vol. 3, pp. 1042, 2009.

[9] W. R. Browne and B. L. Feringa, *Annu. Rev. Phys. Chem*, vol. 60, pp. 407, 2009.

[10] M. Yamada, M. Kondo, J-I Mamiya, Y. Yu, M. Kinoshita, C. J. Barrett, and T. Ikeda, *Angew. Chem. Int. Ed*, vol. 47, pp. 4986, 2008.

[11] T. R. Kelly, *Acc. Chem. Res*, vol. 34, pp. 514, 2001.

[12] T. R. Kelly and J. P. Sestelo, *Struct. Bonding*, vol. 99, pp. 19, 2001.

[13] J. P. Sestelo and T. R. Kelly, *Appl. Phys. A*, vol. 75, pp. 337, 2002.

[14] A. P. Davis, *Angew. Chem. Int. Ed*, vol. 37, pp. 909, 1998.

[15] N. Harada, N. Koumura, and B. L Feringa, *J. Am. Chem. Soc*, vol. 119, pp. 7256, 1997.

[16] N. Koumura, R. W. J. Zijlstra, R. A. Delden, N. Harada, and B. L Feringa, *Nature*, vol. 401, pp. 152, 1999.

[17] B. G. Levine and T. J. Martinez, *Annu. Rev. Phys. Chem*, vol. 58, pp. 613, 2007.

[18] L. Salem, *Angew. Chem. Int. Ed*, vol. 11, pp. 92, 1972.

[19] E. Teller, *J. Chem. Phys*, vol. 41, pp. 109, 1937.

[20] G. Herzberg and H. C. Longuet-Higgins, *Proc. R. Soc. Lond. Ser. A*, vol. 344, pp. 147, 1975.

[21] L. Salem, *Acc. Chem. Res*, vol. 12, pp. 87, 1979.

[22] V. Bonacic-Koutecky, *J. Am. Chem. Soc*, vol. 100, pp. 396, 1978.

[23] M. E. Casida, "Recent advances in density functional methods", Singapore, 1995, p. 155, World Scientific.

[24] B. O. Roos, *Acc. Chem. Res*, vol. 32, pp. 137, 1999.

[25] L. Serrano-Andres, M. Merchdn, I. Nebot-Gil, R. Lindh, and B. O. Roos, *J. Chem. Phys*, vol. 98, pp. 3151, 1992.

[26] T. W. Keal, M. Wanko, and W. Thiel, *Theor Chem Acc*, vol. 123, pp. 145, 2009.

[27] O. Valsson and C. Filippi, *J. Chem. Theory Comput*, vol. 6, pp. 1275, 2010.

[28] C. S. Page and M. Olivucci, *J. Comp. Chem*, vol. 24, pp. 298, 2002.

[29] B. Champagne, E. A. Perpete, D. Jacquemin, S. J. A. van Gisbergen, E-J. Baerends, C. Soubra-Ghaoui, K. A. Robins, and B. Kirtman, *J. Phys. Chem. A*, vol. 104, pp. 4755, 2000.

[30] S. J. A. Gisbergen, C. F. Guerra, and E-J. Baerends, *J. Comp. Chem*, vol. 21, pp. 1511, 2000.

[31] M. Boggio-Pasqua, M. J. Bearpark, M. Klene, and M. A. Robb, *J. Chem. Phys*, vol. 120, pp. 7849, 2004.

[32] P-A Malmqvist, A. Rendell, and B. 0. Roos, *J. Phys. Chem*, vol. 94, pp. 5477, 1990.

[33] P. Celani, F. Bernardi, M. Olivucci, and M. A. Robb, *J. Chem. Phys*, vol. 102, pp. 5733, 1995.

[34] M. Garavelli, P. Celani, F. Bernardi, M. A. Robb, and M. Olivucci, *J. Am. Chem. Soc*, vol. 119, pp. 6891, 1997.

[35] R. Gonzalez-Luque, M. Garavelli, F. Bernardi, M. Merchan, A. Robb, and M. Olivucci, *Proc. Nat. Ac. Sc*, vol. 97, pp. 9379, 2000.

[36] N. Ferre and M. Olivucci, *J. Am. Chem. Soc*, vol. 125, pp. 2003, 2003.

[37] J. Quenneville and T. J. Martinez, *J. Phys. Chem. A*, vol. 107, pp. 829, 2003.

[38] S. Fantacci, A. Migani, and M. Olivucci, *J. Phys. Chem. A*, vol. 108, pp. 1208, 2004.

[39] A. Cembran, F. Bernardi, M. Olivucci, and M. Garavelli, *Proc. Natl. Acad. Sci. USA*, vol. 102, pp. 6255, 2005.

[40] M. Garavelli, P. Celani, F. Bernardi, M. A. Robb, and M. Olivucci, *J. Am. Chem. Soc*, vol. 119, pp. 6891, 1997.

[41] N. Ferre, A. Cembran, M. Garavelli, and M. Olivucci, *Theor Chem Acc*, vol. 112, pp. 335, 2004.

[42] S. Fantacci, A. Migani, and M. Olivucci, *J. Phys. Chem. A*, vol. 108, pp. 1208, 2004.

[43] L Ren, C. H. Martin, K. J. Wise, N. B. Gillespie, H. Luecke, J. K. Lanyi, J. L. Spudich, and R. R Birge, *Biochemistry*, vol. 40, pp. 13906, 2001.

[44] T. Vreven and K. Morokuma, *Theor Chem Acc*, vol. 109, pp. 125, 2003.

[45] S. Hayashi and I. Ohmine, *J Phys Chem B*, vol. 104, pp. 10678, 2000.

[46] H Houjou, K Koyama, M Wada, K Sameshima, Y Inoue, and M Sakurai, *Chem Phys Lett*, vol. 294, pp. 162, 2008.

[47] R. Rajamani and J Gao, *J Comp Chem*, vol. 23, pp. 96, 2002.

[48] A. Warshel and Z. T Chu, *J Phys. Chem. B*, vol. 105, pp. 9857, 2001.

[49] M. Ben-Nun and T. J. Martinez, *Chem. Phys*, vol. 259, pp. 237, 2000.

[50] Giustiniano Tiberio, Luca Muccioli, Roberto Berardi, and Claudio Zannoni, *Chem.Phys.Chem.*, vol. 11, pp. 1018, 2010.

[51] E. Fabiano, T.W. Keal, and W. Thiel, *Chem. Phys*, vol. 349, pp. 334, 2008.

[52] G. Granucci, M. Persico, and A. Toniolo, *J. Chem. Phys*, vol. 114, pp. 10608, 2001.

[53] M. Ben-Nun and T. J. Martinez, *J. Phys. Chem. A*, vol. 103, pp. 10517, 1999.

[54] M. Ben-Nun, J. Quenneville, and T. J. Martinez, *J. Phys. Chem. A*, vol. 104, pp. 5161, 2000.

[55] M. Ben-Nun and T. J. Martinez, *Adv. Chem. Phys*, vol. 121, pp. 439, 2002.

[56] B. L. Feringa, *Acc. Chem. Res*, vol. 34, pp. 504 – 513, 2001.

[57] W. R. Browne and B. L. Feringa, *Nature Nanotech*, vol. 1, pp. 25 – 35, 2006.

[58] B. L. Feringa, *J. Org. Chem*, vol. 72, pp. 6635 – 6652, 2007.

[59] N. Koumura, R. W. J. Zijlstra, R. A. van Delden, N. Harada, and B. L. Feringa, *Nature*, vol. 401, pp. 152 – 155, 1999.

[60] N. Koumura, E.M. Geertsema, M.B. van Gelder, A. Meetsma, and B.L. Feringa, *J. Am. Chem. Soc*, vol. 124, pp. 5037 – 5051, 2002.

[61] D. Pijper, R.A. van Delden, A. Meetsma, and B.L. Feringa, *J. Am. Chem. Soc*, vol. 127, pp. 17612 – 17613, 2005.

[62] M.M. Pollard, A. Meetsma, and B.L. Feringa, *Org. Biomol. Chem*, vol. 6, pp. 507 – 512, 2008.

[63] M.M. Pollard, P.V. Wesenhagen, D. Pijper, and B.L. Feringa, *Org. Biomol. Chem*, vol. 6, pp. 1605 – 1612, 2008.

[64] M. Klok, N. Boyle, M. T. Pryce, A. Meetsma, W. R. Browne, and B.L. Feringa, *J. Am. Chem. Soc*, vol. 130, pp. 10484 – 10485, 2008.

[65] R.A. van Delden, M.K.J. ter Wiel, M.M. Pollard, J. Vicario, N. Koumura, and B.L. Feringa, *Nature*, vol. 437, pp. 1337 – 1340, 2005.

[66] G. London, G.T. Carroll, L. T. Fernandez, M.M. Pollard, P. Rudolf, and B.L. Feringa, *Chem. Commun*, vol. 0, pp. 1712 – 1714, 2009.

[67] W.R. Browne and B.L. Feringa, *Annu. Rev. Phys. Chem*, vol. 60, pp. 407 – 428, 2009.

[68] E. M. Geertsma, S. J. van der Molen, M. Martens, and B.L. Feringa, *Proc. Natl. Acad. Sci*, vol. 106, pp. 16919 – 16924, 2009.

[69] M. Klok, L. P. B. M. Janssen, W. R. Browne, and B. L. Feringa, *Faraday Discuss*, vol. 143, pp. 319 – 334, 2009.

[70] G. Groenhof, *University of Groningen and Groningen*, vol. 0, pp. 0, 2005.

[71] S. M. Grimm, *Ludwig-Maximilians-Universitat Munchen, Munchen*, vol. 0, pp. 0, 2005.

[72] S. Grimm, C. Bruchle, and I. Frank, *ChemPhysChem*, vol. 6, pp. 1943, 2005.

[73] A. Koslowski, M. E. Beck, and W. Thiel, *J. Comput. Chem*, vol. 24, pp. 714, 2003.

[74] A. Szabo and N. S. Ostlund, *Modern Quantum Chemistry*, Mineola, New York: Dover, 1996.

[75] J. A. Pople, J. S. Binkley, and R. Seeger, *Int. J. Quant. Chem. Symp.*, vol. 10, pp. 1, 1976.

[76] J. Cízek, *J. Chem. Phys*, vol. 45, pp. 4256, 1966.

[77] B. O. Roos and K. Andersson, *Chem Phys Lett*, vol. 245, pp. 125–223, 1995.

[78] G. Ghigo, B. O. Roos, and P.-Å. Malmqvist, *Chem Phys Lett*, vol. 396, pp. 142–149, 2004.

[79] L. Serrano-Ands, M. Merchdn, I. Nebot-Gil, R. Lindh, and B. O Roos, *J. Chem. Phys*, vol. 98, pp. 3151, 1993.

[80] H. Nakano, *J. Chem. Phys*, vol. 99, pp. 7983, 1993.

[81] J. Finley, P.-Å. Malmqvist, B. O. Roos, and L. Serrano-Andres, *Chem Phys Lett*, vol. 288, pp. 299, 1998.

[82] C. Angeli, R. Cimiraglia, S. Evangelisti, T. Leininger, and J. P. Malrieu, *J. Chem. Phys.*, vol. 114, pp. 10252, 2001.

[83] C. Angeli, R. Cimiraglia, and J. P. Malrieu, *Chem. Phys. Lett.*, vol. 350, pp. 297, 2001.

[84] C. Angeli, R. Cimiraglia, and J. P. Malrieu, *J. Chem. Phys.*, vol. 117, pp. 9138, 2002.

[85] H. A. Witek, Y. K. Choe, J. P. Finley, and K. Hirao, *J. Comp. Chem.*, vol. 23, pp. 957, 2002.

[86] C. Lee, W. Yang, and R. G. Parr, *Phys. Rev. B*, vol. 37, pp. 785 – 789, 1988.

[87] W. Kohn and L. J Sham, *Phys. Rev. A*, vol. 140, pp. 1133, 1965.

[88] E. Runge and E. K. U. Gross, *Phys. Rev. Lett*, vol. 52, pp. 997, 1984.

[89] S. Hirato and M. Head-Gordon, *Chem Phys Lett*, vol. 314, pp. 291, 1999.

[90] F. Aryasetiawan, O. Gunnarsson, and A Rubio, *Europhys. Lett*, vol. 57, pp. 683, 2002.

[91] O. V. Gritsenko, S. J. A. van Gisbergen, A. Gorling, and E. J Baerends, *J. Chem. Phys*, vol. 113, pp. 8478, 2000.

[92] M. E. Casida, F. Gutierrez, J. Guan, F.-X. Gadea, D. Salahub, and J.-P Daudey, *J. Chem. Phys*, vol. 113, pp. 7062, 2000.

[93] P. R. T. Schipper, O. V. Gritsenko, and E. J Baerends, *Theor. Chem. Acc*, vol. 99, pp. 329, 1998.

[94] P. R. T. Schipper, O. V. Gritsenko, and E. J Baerends, *J. Chem. Phys*, vol. 111, pp. 4056, 1999.

[95] E. H Lieb, *Int. J. Quantum Chem*, vol. 24, pp. 243, 1983.

[96] H. Englisch and R. Englisch, *Phys. Stat. Sol. (B)*, vol. 123, pp. 711, 1984.

[97] H. Englisch and R. Englisch, *Phys. Stat. Sol. (B)*, vol. 124, pp. 373, 1984.

[98] R. M. Dreizler and E. K. U. Gross, *Density Functional Theory*, vol. 0, Springer, Berlin, 1990.

[99] J. C. Slater, J. B. Mann, T. M. Wilson, and J. H. Wood, *Phys Rev*, vol. 184, pp. 672, 1969.

[100] T. Ziegler, A. Rauk, and E. J Baerends, *Theor. Chim. Acta*, vol. 43, pp. 261, 1977.

[101] O. Gunnarsson and B. I. Lundqvist, *Phys. Rev. B*, vol. 13, pp. 4274, 1976.

[102] U. von Barth, *Phys Rev A*, vol. 20, pp. 1693, 1979.

[103] A. Gorling, *Phys. Rev. A*, vol. 47, pp. 2783–2799, 1993.

[104] A. Theophilou, *Int. J. Quant. Chem*, vol. 69, pp. 461–467, 1998.

[105] C. Daul, *Int. J. Quant. Chem*, vol. 52, pp. 867–877, 1994.

[106] I. Frank, J. Hutter, D. Marx, and M Parinello, *J. Chem. Phys*, vol. 108, pp. 4060, 1998.

[107] M. Filatov and S Shaik, *Chem. Phys. Lett*, vol. 288, pp. 689, 1998.

[108] R. Gaudoin and K. Burke, *Phys. Rev. Lett.*, vol. 93 ibid, pp. 173001, 2004.

[109] R. Gaudoin and K. Burke, *Phys. Rev. Lett.*, vol. 94, pp. 029901, 2005.

[110] A. K. Theophilou, *J. Phys. C: Solid State Phys*, vol. 12, pp. 5419, 1979.

[111] J. Katriel, *J. Phys. C*, vol. 13, pp. L375, 1980.

[112] H. Englisch, H. Fieseler, and A Haufe, *Phys. Rev. A*, vol. 37, pp. 4570, 1988.

[113] E. K. U. Gross, L. N. Oliveira, and W. Kohn, *Phys. Rev. A*, vol. 37, pp. 2805, 1988.

[114] E. K. U. Gross, L. N. Oliveira, and W. Kohn, *Phys. Rev. A*, vol. 37, pp. 2809, 1988.

[115] C. C. J. Roothaan, *Rev. Mod. Phys*, vol. 32, pp. 179, 1960.

[116] K. Hirao and H. Nakatsuji, *J. Chem. Phys*, vol. 59, pp. 1457, 1973.

[117] B. Levi and G. Berthier, *Int. J. Quant. Chem*, vol. 2, pp. 307, 1968.

[118] M. Filatov and S. Shaik, *Chem. Phys. Lett*, vol. 304, pp. 429 – 437, 1999.

[119] F. Schautz, F. Buda, and C. Filippi, *J. Chem. Phys*, vol. 121, pp. 5836–5844, 2004.

[120] F. Buda and C. Filippi, *J. Chem. Phys*, vol. 122, pp. 087102, 2005.

[121] M. Filatov and S Shaik, *J. Phys. Chem. A*, vol. 104, pp. 6628, 2000.

[122] M. Filatov and S. Shaik, *J. Phys. Chem. A*, vol. 104, pp. 6628 – 6636, 2000.

[123] S. P. de Visser, M. Filatov, and S. Shaik, *Phys. Chem. Chem. Phys*, vol. 2, pp. 5046 – 5048, 2000.

[124] I. de P. R. Moreira, R. Costa, M. Filatov, and F Illas, *J. Chem. Theory Comput*, vol. 3, pp. 764–774, 2007.

[125] D. Cremer, M. Filatov, V. Polo, E. Kraka, and S Shaik, *Int. J. Mol. Sci*, vol. 3, pp. 604, 2002.

[126] F. Illas, I. de P. R. Moreira, J. M. Bofill, and M Filatov, *Phys. Rev. B*, vol. 70, pp. 132414, 2004.

[127] F. Illas, I. de P. R. Moreira, J.M. Bofill, and M Filatov, *Theor. Chem. Acc*, vol. 116, pp. 587–597, 2006.

[128] P. Hohenberg and W Kohn, *Phys. Rev. B*, vol. 136, pp. 864, 1964.

[129] M. Levy and A Nagy, *Phys. Rev. Lett.*, vol. 83, pp. 4361, 1999.

[130] A. Nagy and M. Levy, *Phys. Rev. A*, vol. 63, no. 052502, 2001.

[131] P. Samal, M. K. Harbola, and A. Holas, *Chem. Phys. Lett.*, vol. 419, pp. 217, 2006.

[132] P. Samal and M. K Harbola, *J. Phys. B: At. Mol. Opt. Phys*, vol. 39, pp. 4065–4080, 2006.

[133] M Levy, *Phys. Rev. A*, vol. 26, pp. 1200, 1982.

[134] L. N. Oliveira, E. K. U. Gross, and W. Kohn, *Phys. Rev. A*, vol. 37, pp. 282, 1988.

[135] A. K. Rajagopal and F. A Bout, *Phys. Rev. A*, vol. 51, pp. 1770–1775, 1995.

[136] L Salem, *Science*, vol. 191, pp. 822–830, 1976.

[137] V. Bonacic-Koutecky, P. Bruckmann, P. Hiberty, J. Koutecky, C. Leforestier, and L Salem, *Angew. Chem. and Int. Ed. Engl*, vol. 14, pp. 575–576, 1975.

[138] L. Salem and C. Rowland, *Angew. Chem. and Int. Ed. Engl*, vol. 11, pp. 92–111, 1972.

[139] F. Cordova, J. Doriol, A. Ipatov, M. E. Casida, C. Filippi, and A Vela, *J. Chem. Phys*, vol. 127, pp. 164111, 2007.

[140] E. J Baerends, *Phys. Rev. Lett*, vol. 87, pp. 133004, 2001.

[141] M. E. Casida, F. Gutierrez, J. Guan, F.-X. Gadea, D. Salahub, and J.-P Daudey, *J. Chem. Phys*, vol. 113, pp. 7062, 2000.

[142] M. Wanko, M. Garavelli, F. Bernardi, T. A. Niehaus, T. Frauenheim, and M Elstnera, *J. Chem. Phys*, vol. 120, pp. 1674, 2004.

[143] B. Roos and P. R Taylor, *Chem. Phys*, vol. 48, pp. 157–173, 1980.

[144] K. Andemson, P.-A. Malmqvist, B. O Roos, O. Andrzej, J. Sadlej, and K Wolinskit, *J. Phys. Chem*, vol. 94, pp. 5483–5488, 1990.

[145] R. S. Mulliken, *Phys. Rev*, vol. 41, pp. 751, 1932.

[146] M. Filatov and S Shaik, *J. Chem. Phys*, vol. 110, pp. 116, 1999.

[147] J. Grafenstein, E. Kraka, and D Cremer, *Chem. Phys. Lett*, vol. 288, pp. 593–602, 1998.

[148] E. Kraka, J. Grafenstein, M. Filatov, H. Joo, D. Izotov, J. Gauss, Y. He, A. Wu, V. Polo, L. Olsson, Z. Konkoli, Z. He, and D. Cremer, *COLOGNE08 Stocton CA: University of the Pacific*, vol. 0, pp. 0, 2008.

[149] R. Krishnan, J. S. Binkley, R. Seeger, and J. A. Pople, *J. Chem. Phys*, vol. 72, pp. 650 – 654, 1980.

[150] P. J. Stephens, F. J. Devlin, C. F. Chabalowski, and M. J Frisch, *J. Phys. Chem*, vol. 98, pp. 11623, 1994.

[151] A. D. Becke, *Rev. Mod. Phys*, vol. 98, pp. 1372, 1993.

[152] G. Karlstrom, R. Lindh, P.A. Malmqvist, B. O. Roos, U. Ryde, V. Veryazov, P.-O. Widmark, M. Cossi, B. Schimmelpfennig, P. Neogrady, and L Seijo, *Comp. Mat. Sci*, vol. 28, pp. 222, 2003.

[153] R. Zijlstra, *Excited State Charge Separation in Symmetrical Alkenes*, Phd thesis, Rijksuniversiteit Groningen (RuG), Groningen, The Netherlands, 2001.

[154] M. Gruning, O. V. Gritsenko, and E. J Baerends, *J. Chem. Phys*, vol. 118, pp. 7183–7192, 2003.

[155] C. A. Coulson and I Fischer, *Philos. Mag*, vol. 40, pp. 386, 1949.

[156] W. Kolos and L. J Wolniewicz, *Chem. Phys*, vol. 43, pp. 2429, 1965.

[157] W. Kolos and L. J Wolniewicz, *Chem. Phys*, vol. 45, pp. 509, 1966.

[158] D. Cremer, *Mol. Phys*, vol. 99, pp. 1899, 2001.

[159] V. Polo, E. Kraka, and D Cremer, *Mol. Phys*, vol. 100, pp. 1771, 2002.

[160] R. J. Sension and B. S. Hudson, *J. Chem. Phys*, vol. 90, pp. 1377, 1989.

[161] P. D. Foo and K. K. Innes, *J. Chem. Phys*, vol. 60, pp. 4582, 1974.

[162] J.E. Douglas, B.S. Rabinovitch, and F.S Looney, *J. Chem. Phys*, vol. 23, pp. 315, 1955.

[163] S. Grimm, C. Nonnenberg, and I Frank, *J. Chem. Phys*, vol. 119, pp. 11574, 2003.

[164] D. G. Leopold, R. D. Pendley, J. L. Roebber, R. J. Hemley, and V Vaida, *J. Chem. Phys*, vol. 81, pp. 4218, 1984.

[165] W. Haugen and M. Traetteberg, *Acta Chem. Scand.*, vol. 22, pp. 628, 1966.

[166] M.Traetteberg, *Acta Chem. Scand.*, vol. 22, pp. 628, 1968.

[167] C. Woywod, W. C. Livingood, and J. H Frederick, *J. Chem. Phys*, vol. 112, pp. 613, 2000.

[168] W. T. Borden and E. R Davidson, *J. Am. Chem. Soc*, vol. 99, pp. 4587, 1977.

[169] N. Harada, N. Koumura, and B. L Feringa, *J. Am. Chem. Soc*, vol. 119, pp. 7256, 1997.

[170] N. Koumura, R. W. J. Zijlstra, R. A. Delden, N. Harada, and B. L Feringa, *Nature*, vol. 401, pp. 152, 1999.

[171] M. M. Pollard, A. Meetsma, M. Klok, D. Pijper, and B. L Feringa, *Adv. Funct. Mater*, vol. 17, pp. 718, 2007.

[172] M. M. Pollard, A. Meetsma, and B. L Feringa, *Org. Biomol. Chem*, vol. 6, pp. 507, 2008.

[173] R. Augulis, M. Klok, B. L. Feringa, and P. H. M Loosdrecht, *Phys. Stat. Sol*, vol. 6, pp. 181, 2009.

[174] F. Bernardi, M. Olivucci, and M. A. Robb, *Chem. Soc. Rev*, vol. 25, pp. 321, 1996.

[175] B. G. Levine and T. J Martinez, *Ann. Rev. Phys. Chem*, vol. 58, pp. 613, 2007.

[176] D. R Yarkony, *Rev. Mod. Phys*, vol. 68, pp. 985, 1996.

[177] M. R. Silva-Junior, M. Schreiber, S. P. A. Sauer, and W. Thiel, *J. Chem. Phys*, vol. 129, pp. 104103, 2008.

[178] A. Kazaryan, J. Heuver, and M. Filatov, *J. Phys. Chem. A*, vol. 112, pp. 12980 – 12988, 2008.

[179] W. J. Hehre, R. F. Stewart, and J. A Pople, *J. Chem. Phys*, vol. 51, pp. 2657, 1969.

[180] J. Torras, F. Rodriguez-Ropero, O. Bertran, and C Aleman, *J. Phys. Chem. C*, vol. 113, pp. 3574, 2009.

[181] T. W. Keal, A. Koslowski, and Thiel. W., *Theor. Chem. Acc*, vol. 118, pp. 837, 2007.

[182] A.H. Zewail, *J. Phys. Chem. A*, vol. 104, pp. 5660 – 5694 and references cited therein, 2000.

[183] D.R. Yarkony, *Rev. Mod. Phys*, vol. 68, pp. 985 – 1013, 1996.

[184] F. Bernardi, M. Olivucci, and M.A. Robb, *Chem. Soc. Rev*, vol. 25, pp. 321 – 328, 1996.

[185] J. Quenneville and T. J. Martinez, *J. Phys. Chem. A*, vol. 107, pp. 829 – 837, 2003.

[186] T. Schultz, J. Quenneville, B. Levine, A. Toniolo, T. J. Martinez, S. Lochbrunner, M. Schmitt, J. P. Shaffer, M. Z. Zgierski, and A. Stolow, *J. Am. Chem. Soc*, vol. 125, pp. 8098 – 8099, 2003.

[187] B.G. Levine, J.D. Coe, and T.J. Martinez, *J. Phys. Chem. B*, vol. 112, pp. 405 – 413, 2008.

[188] A. Kazaryan and M. Filatov, *J. Phys. Chem. A*, vol. 113, pp. 11630 –11634, 2009.

[189] P. R. T. Schipper, O. V. Gritsenko, and E. J. Baerends, *Theor. Chem. Acc*, vol. 99, pp. 329 – 343, 1998.

[190] R. Augulis, M. Klok, B.L. Feringa, and P.H.M. van Loosdrecht, *Phys. Stat. Sol. (c)*, vol. 6, pp. 181 – 184, 2009.

[191] P. J. Stephens, F. J. Devlin, C. F. Chabalowski, and M. J. Frisch, *J. Phys. Chem*, vol. 98, pp. 11623 – 11627, 1994.

[192] M. J. Frisch and et al, *GAUSSIAN 03 and Revision B2 and Gaussian Inc.: Pittsburgh and PA*, vol. 0, pp. 0, 2003.

[193] C. Wu, S. Tretiak, and V. Y. Chernyak, *Chem. Phys. Lett.*, vol. 433, pp. 305, 2007.

[194] B. Hess, C. Kutzner, van der Spoel m D., and E. Lindahl, *J. Chem. Theory Comput*, vol. 4, pp. 435 – 447, 2008.

[195] W. L. Jorgensen and J. Tirado-Rives, *J. Am. Chem. Soc*, vol. 110, pp. 1657 – 1666, 1988.

[196] G. Bussi, D. Donadino, and M. Parrinello, *J. Chem. Phys*, vol. 126, pp. 014101, 2007.

[197] G. Groenhof, L. V. Schäfer, M. Boggio-Pasqua, M. Goette, H. Grubmuller, and M. A. Robb, *J. Am. Chem. Soc*, vol. 129, pp. 6812 – 6819, 2007.

[198] J. J. P. Stewart, *J. Comp. Chem.*, vol. 10, pp. 209, 1989.

[199] J. J. P. Stewart, *J. Comp. Chem.*, vol. 10, pp. 221, 1989.

[200] W. Fuss, C. Kosmidis, W. E. Schmid, and S. A. Trushin, *Angew. Chem. Int. Ed*, vol. 43, pp. 4178 – 4182, 2004.

[201] D. G. Truhlar and C. A. Mead, *Phys. Rev. A*, vol. 68, pp. 032501, 2003.

[202] A. Sinicropi, E. Martin, M. Ryazantsev, J. Helbing, J. Briand, D. Sharma, J. Leonard, S. Haacke, A. Cannizzo, M. Chergui, V. Zanirato, S. Fusi, F. Santoro, R. Basosi, N. Ferre, and M. Olivucci, *Proc. Nat. Acad. Sci*, vol. 105, pp. 17642 – 17647, 2008.

[203] L. Rivado-Casas, D. Sampedro, P. J. Campos, S. Fusi, V. Zanirato, and M. Olivucci, *J. Org. Chem*, vol. 74, pp. 4666 – 4674, 2009.

[204] S.-M. Park, P. H. Nguyen, and G. Stock, *J. Chem. Phys*, vol. 131, pp. 184503, 2009.

[205] G. Groenhof, L. V. Schäfer, M. Boggio-Pasqua, and M. A. Robb, ", Weinheim, 2009, vol. 0 of *Handbook in Molecular Biophysics*, Wiley-VCH.

[206] G. Groenhof, M. Bouxin-Cademartory, B. Hess, S. P. de Visser, H. J. C. Berendsen, M. Olivucci, A. E. Mark, and M. A. Robb, *J. Am. Chem. Soc*, vol. 126, pp. 4228 – 4233, 2004.

[207] G. Groenhof, L. V. Schäfer, M. Boggio-Pasqua, H. Grubmuller, and M. A. Robb, *J. Am. Chem. Soc*, vol. 130, pp. 3250 – 3251, 2008.

[208] M. Boggio-Pasqua, M. A. Robb, and G. Groenhof, *J. Am. Chem. Soc*, vol. 131, pp. 13580 – 13581, 2009.

[209] C. Ko, B. Levine, A. Toniolo, L. Manohar, S. Olsen, H. J. Werner, and T. J. Martinez, *J. Am. Chem. Soc*, vol. 125, pp. 12710 – 12711, 2003.

[210] C. Ko, A. M. Virshup, and T. J. Martinez, *Chem. Phys. Lett*, vol. 460, pp. 272 – 277, 2008.

[211] A. Warshel and Z. T. Chu, *J. Phys. Chem. B*, vol. 40, pp. 9857 – 9871, 2001.

[212] S. Hayashi, E. Tajkhorshid, and K. Schulten, *Biophys. J*, vol. 85, pp. 1440 – 1449, 2003.

[213] U. F. Rohrig, L. Guidoni, A. Laio, I. Franck, and U. Rothlisberger, *J. Am. Chem. Soc*, vol. 126, pp. 15328 – 15329, 2004.

[214] L. M. Frutos, T. Andruniow, F. Santoro, N. Ferre, and M. Olivucci, *Proc. Natl. Acad. Sci. USA*, vol. 104, pp. 7764 – 7769, 2007.

[215] S. Hayashi, E. Tajkhorshid, and K. Schulten, *Biophys. J*, vol. 96, pp. 403 – 416, 2009.

[216] A. Toniolo, S. Olsen, L. Manohar, and T. J. Martinez, *Faraday Discuss*, vol. 127, pp. 149 – 163, 2004.

[217] L. V. Schäfer, G. Groenhof, M. Boggio-Pasqua, M. A. Robb, and H. Grubmuller, *PLoS Comput. Biol*, vol. 4, pp. 1000034, 2008.

[218] A. M. Virshup, C. Punwong, T. V. Pogorelov, B. A. Lindquist, C. Ko, and T. J. Martinez, *J. Phys. Chem. B*, vol. 113, pp. 3280 – 3291, 2009.

[219] P. R. L. Markwick and N. L. Doltsinis, *J. Chem. Phys*, vol. 126, pp. 175102, 2007.

[220] H. Nieber and N. L. Doltsinis, *Chem. Phys*, vol. 347, pp. 1–3 405 – 412, 2008.

[221] E. Fabiano and W. Thiel, *J. Phys. Chem. A*, vol. 112, pp. 6859 – 6863, 2008.

[222] Z. G. Lan, E. Fabiano, and W. Thiel, *ChemPhysChem*, vol. 10, pp. 1225 – 1229, 2009.

[223] Z. G. Lan, E. Fabiano, and W. Thiel, *J. Phys. Chem. B*, vol. 11, pp. 3548 – 3555, 2009.

[224] S. Grimm, C. Brauchle, and I. Franck, *ChemPhysChem*, vol. 6, pp. 1943 – 1947, 2005.

[225] A. Kazaryan, J. C. M. Kistemaker, L. V. Schäfer, W. R. Browne, B. L. Feringa, and M. Filatov, *J. Phys. Chem. A*, vol. 114, pp. 5058–5067, 2010.

[226] C. Wittig, *J. Phys. Chem. B*, vol. 109, pp. 8428 – 8430, 2005.

[227] O.F. Lange, L. V. Schäfer, and H. Grubmuller, *J. Comp. Chem*, vol. 27, pp. 1693 – 1702, 2006.

[228] G. R. Fleming, Oxford University Press, Oxford, 1986.

[229] B. H. Lengsfield III and D. R. Yarkony, "Nonadiabatic interactions between potential energy surfaces: theory and applications", 1992, vol. 82 of *Advances in Chemical Physics: State-Selected and State to State Ion-Molecule Reaction Dynamics: Part 2 Theory*, John Wiley.

[230] G. A. Worth and L. S. Cederbaum, *Annu. Rev. Phys. Chem.*, vol. 55, pp. 127, 2004.

[231] M. Barbatti, J. Paier, and H. Lischka, *J. Chem. Phys*, vol. 121, pp. 11614, 2004.

[232] L. Freund and M. Klessinger, *Int. J. Quant. Chem*, vol. 70, pp. 1023, 1998.

[233] B. G. Levine and T. J. Martinez, "Code for optimization of minimal energy conical intersections", 2007.

[234] B. R. Brooks and H. F. Schäfer, *J. Am. Chem. Soc.*, vol. 101, pp. 307, 1979.

[235] W. Thiel, "Mndo program, version 6.1", 2007.

[236] W. Weber, Phd thesis, Universität Zürich, Switzerland, 1996.

[237] W. Weber and W. Thiel, *Theor. Chem. Acc.*, vol. 103, pp. 495, 2000.

[238] N. Otte, M. Scholten, and W. Thiel, *J. Phys. Chem. A*, vol. 111, pp. 5751, 2007.

[239] M. R. Silva-Junior and W. Thiel, *J. Chem. Theory Comput.*, vol. 6, pp. 1546, 2010.

[240] P. O. Löwdin, *J. Chem. Physics*, vol. 18, pp. 365, 1950.

[241] R. D. BROWN and K. R. ROBY, *Theoret. chim. Acta (Berl.)*, vol. 16, pp. 175–193, 1970.

[242] P. Coffey and K. Jug, *J. Am. Chem. Soc.*, vol. 14, pp. 7575, I973.

[243] D. N. Nanda and Karl Jug, *Theoret. Chim. Acta (Berl.)*, vol. 57, pp. 95, 1980.

[244] M. J. Filatov, O. V. Gritsenko, and G. M. Zhidomirov, *Theor Chim Acta*, vol. 72, pp. 211, 1987.

[245] M. J. Filatov, I. L. Zilberberg, and G. M. Zhidomirov, *Int. J. Quant. Chem.*, vol. 44, pp. 565, 1992.

[246] K Jug, R Lert, and J Schulz, *Int. J. Quant. Chem.*, vol. 32, pp. 265, 1987.

[247] W. Domcke, D. R. Yarkony, and H. Köppel, *Conical Intersections: Electronic Structure, Dynamics and Spectroscopy*, World Scientific, Singapore, 2004.

[248] H.-J. Werner, P. J. Knowles, R. Lindh, F. R. Manby, M. Schutz, P. Celani, T. Korona, G. Rauhut, R. D. Amos, A. Bernhardsson, A. Berning, D. L. Cooper, M. J. O. Deegan, A. J. Dobbyn, F. Eckert, C. Hampel, G. Hetzer, A. W. Lloyd, S. J. McNicholas, W. Meyer, M. E. Mura, A. Nicklass, P. Palmieri, U. Schumann, H. Stoll, A. J. Stone, R. Tarroni, and T. Thosteinsson., "Molpro, version 2006.1, a package of ab initio programs", 2006.

[249] J. C. Tully, *J. Chem. Phys.*, vol. 93, pp. 1061, 1990.